Thirty years of H_3^+ astronomy

Steve Miller* and Jonathan Tennyson

Department of Physics and Astronomy, University College London, London WC1E 6BT, United Kingdom

Thomas R. Geballe

Gemini Observatory, 670 North A'ohoku Place, Hilo, Hawaii 96720, USA

Tom Stallard

School of Physics and Astronomy, University of Leicester, Leicester LE2 7RH, United Kingdom

(published 3 August 2020)

This review covers the work of the three decades since the first spectroscopic identification of the H_3^+ molecular ion outside of the laboratory in 1988, in the auroral atmosphere of the giant planet Jupiter. These decades have seen the astronomy related to this simple molecular ion expand to such an extent that a summary and evaluation of some 450 refereed articles is provided in the review. This enormous body of work has revealed surprises and illuminated the extensive role played by H_3^+ in astrophysical environments in our Solar System and beyond. At the same time the physical chemistry and chemical physics of the molecule that has been revealed and studied during this time has proved to be fascinating and enabled high-resolution spectroscopy to benchmark its achievements against equally high-precision calculations. This review includes a brief look at some of the key foundational articles from before the original 1988 Jupiter detection (including the original 1911 ion discharge tube detection by J. J. Thomson and the key laboratory spectroscopy and quantum mechanics calculations on H_3^+ structure and spectrum). The review explains the original detection and its serendipitous nature and looks at the astronomy that followed, all the way up to the latest results from NASA's *Juno* mission. Also covered are the major advances in our understanding of the interstellar medium (known as ISM) that have resulted from the detection of H_3^+ absorption lines there in 1996. The review closes by examining claims for the ion's presence in other astrophysical environments and its potential role in the atmospheres of exoplanets and brown dwarfs.

DOI: 10.1103/RevModPhys.92.035003

CONTENTS

*Corresponding author.
s.miller@ucl.ac.uk

I. INTRODUCTION

H_3^+, the simplest polyatomic molecular ion, sometimes known as trihydrium, was discovered in laboratory discharges by J. J. Thomson in 1911 (Thomson, 1913). Over the next seven decades, its stability, production mechanism, and molecular structure were determined via laboratory experiments and quantum theory. It has proved to be a challenge to both theoretical physicists and chemists since Bohr (1919) first took up the task of explaining its stability.

H_3^+ was first suggested as a constituent of the molecular interstellar medium (ISM) by Martin, McDaniel, and Meeks (1961). However, its key role in the physics and chemistry there was not recognized until a dozen years later, following the use of microwave spectroscopy to discover abundant simple molecular species [e.g., ammonia (NH_3), water (H_2O), and carbon monoxide (CO)] in dense ($n \geq 10^3$ cm^{-3}) interstellar clouds. This in turn led to the recognition that chains of ion-neutral reactions were the dominant gas-phase chemistry within those clouds and that H_3^+, created by the cosmic-ray ionization of H_2 followed by the reaction $H_2^+ + H_2 \rightarrow H_3^+ + H$, was at the start of each chain (Herbst and Klemperer, 1973; Watson, 1973a).

It was only following the laboratory measurement of the spectrum of H_3^+ by Oka (1980) that a search for H_3^+ in the ISM could be initiated. This search eventually led to the detection by Geballe and Oka (1996) of its absorption spectrum in two dense clouds. But the infrared (IR) spectrum of this simple molecular ion had first been identified, outside of the laboratory, in the atmosphere of Jupiter by Drossart *et al.* (1989). Since then it has been found on Saturn (Geballe, Jagod, and Oka, 1993) and Uranus (Trafton *et al.*, 1993), but not Neptune, for reasons still not fully understood (Melin *et al.*, 2018). It is also actively being sought in the atmospheres of giant extrasolar planets and is part of the target list for ESA's upcoming Ariel exoplanet mission (Tinetti *et al.*, 2018).

For planetary systems, H_3^+ has been used to trace and monitor conditions in the magnetosphere and solar wind by their effects on the atmospheres of Jupiter and Saturn (the TV-screen approach) in tandem with missions such as *Galileo* (Jupiter) (Altieri *et al.*, 2016), *Juno* (Jupiter) (Dinelli *et al.*, 2017), and *Cassini* (Saturn) (Brown *et al.*, 2004). H_3^+ has been shown to be both an atmospheric coolant (the "H_3^+ thermostat" effect) and the carrier of electric currents and the driver of wind systems, both of which can heat atmospheres. For giant extrasolar planets, its cooling effect has been modeled as critical for determining just how much energy upper atmospheres can absorb before they undergo massive expansion and hydrodynamic mass loss (Koskinen, Aylward, and Miller, 2007). H_3^+ may have played a crucial role in stabilizing Jupiter itself in the conditions of the early Solar System, when far ultraviolet output from the Sun was much greater (Ribas *et al.*, 2005, 2010). As this review shows, there is now a large body of work making use of H_3^+ studies, both observational and modeling, for planetary science.

The measured abundances of H_3^+ in dense clouds cemented the understanding of H_3^+ as the starting point of ion-neutral chemistry. H_3^+ has now been observed not only in dozens of dense clouds within the Milky Way but also in lower density ($n < 10^3$ cm^{-3}) diffuse clouds (McCall *et al.*, 1998), and even in molecular gas in a few distant galaxies. But H_3^+ is much more than the smoking gun for interstellar chemistry. Because of its unique production mechanism, which is driven by cosmic-ray ionization of H_2 rather than molecular collisions, the density of H_3^+ is a sensitive probe of the cosmic-ray ionization rate ζ (Cravens and Dalgarno, 1978), scaling with it rather than with the cloud density in almost all cases, unlike the densities of most other molecules. Studies of H_3^+ in dense and diffuse clouds clearly demonstrated for the first time that the cosmic-ray ionization rate of H_2 in diffuse clouds is typically an order of magnitude higher than in dense clouds (McCall *et al.*, 2003). This finding has significantly tightened the constraints on the cosmic-ray spectrum, which is impossible to directly measure fully from inside the Solar System.

In normal interstellar clouds, the energy level structure of H_3^+ allows it to serve as an accurate low-temperature thermometer. Observations of H_3^+ in the interstellar gas of the central few hundred parsecs of our Galaxy have resulted in the discovery of previously unknown, warm low-density gas, rich in H_3^+ (Oka *et al.*, 2019), which pervades that region. This discovery has upended the previous understanding of the Galactic Center's interstellar environment. Studies have demonstrated that it is created in high abundance due to a flux of cosmic rays, from the vicinity of the central supermassive black hole, from hot stars, from supernovae, and from other energetic phenomena, that is up to 2 orders of magnitude greater than elsewhere in the Galaxy.

The role played by H_3^+ is critically determined by its own special physical properties: although it has equilateral triangle symmetry, and thus no permanent dipole, its vibrational modes can distort that symmetry to produce strong transition moments [typical Einstein A_{if} coefficients of 100 s^{-1} or more (Miller and Tennyson, 1988a)], and as a "floppy" molecule it has many IR active vibrational bands that "classical" spectroscopy would not expect to be strongly emitting or absorbing (Le Sueur, Henderson, and Tennyson, 1993). Diagnostic features inherent to H_3^+ stem also from its rotational energy level structure, and the radiative transitions (or lack thereof) connecting those levels. We start this review with an overview of the basic properties of the H_3^+ molecular ion. Readers interested in the astronomy alone may wish to start with Sec. III, although much of the spectroscopic notation used in the later sections is discussed in Secs. II.A and II.B.

II. PHYSICS OF H_3^+

A. Basic properties

H_3^+, with two electrons binding three protons, is the electronically simplest stable polyatomic molecule. As such it has provided both a benchmark and a challenge system for molecular physics theory (Morong, Gottfried, and Oka, 2009;

Tennyson *et al.*, 2017) since Bohr (1919) first attempted quantum calculations. (Bohr actually concluded that H_3^+ was unstable, while the neutral H_3 was stable.) Subsequently Eyring, Hirschfelder, and Taylor (1936), Hirschfelder, Eyring, and Rosen (1936a, 1936b), Hirschfelder, Eyring, and Topley (1936), Hirschfelder, Diamond, and Eyring (1937), Hirschfelder (1938), and Hirschfelder and Weygandt (1938) showed that H_3^+ was indeed stable with a triangular equilibrium geometry; they concluded that an isosceles triangle was the configuration with the lowest energy, although Coulson (1935) had proposed an equilateral triangle. World War II seemed to interrupt work on this problem. In the 1960s, when the problem of the equilibrium structure of H_3^+ was again taken up, several groups (Christoffersen, Hagstrom, and Prosser, 1964; Conroy, 1964; Hoyland, 1964) confirmed Coulson's suggestion of an equilateral triangle as the equilibrium geometry; see also Oka (1992), Kragh (2010, 2012), and Miller (2012). The absolute nonrelativistic electronic energy for H_3^+ for modern calculations is given in Table I.

H_3^+ is relatively easy to produce in a molecular-hydrogen ion source [see review by Wu *et al.* (2019)]: ionization of molecular hydrogen gives H_2^+, which reacts with H_2 on essentially every collision to form H_3^+ plus H. This process is exothermic by about 1.74 eV. Much of the excess energy is retained as internal energy of the H_3^+ molecule, which has consequences for experiments performed with the resulting ions (Anicich and Futrell, 1984), some of which are discussed later.

H_3^+ has a number of somewhat unusual properties, which are associated at least in part with the equilateral triangle structure of its equilibrium geometry. The structure of H_3^+ and D_3^+ mean that they have no permanent dipole moment, which has important consequences for their spectroscopy (discussed later). The mixed isotopologue ions H_2D^+ and D_2H^+ do have significant permanent dipole moments, about 0.61 and 0.49 D, respectively. These dipole arise from a simple geometric effect due to separation of the center of mass, which shifts with isotopic substitution, from the center of charge, which does not. H_2D^+ and D_2H^+ also differ from H_3^+ and D_3^+ in their vibrational structure, but a detailed discussion of this is beyond the scope of this review.

The rotational states of the ground vibrational state are defined by two quantum numbers: the angular momentum J and its projection onto the symmetry axis K (discussed later). The proton is a fermion and as a result of the Pauli principle all states must be antisymmetric with respect to the interchange of H nuclei. One consequence is that there is no zero rotational state ($J = 0$) of the H_3^+ vibrational ground state and the lowest states have $J = 1$. There are two $J = 1$ states: an *ortho* ($J = 1$, $K = 0$) state with total nuclear spin $I = 3/2$ and a *para* ($J = 1$, $K = 1$) state with total nuclear spin $I = 1/2$. The spin weighting g_s of a state, essential for calculating partition functions and spectral line intensities, is then given by $2I + 1$, giving *ortho* states a spin weighting of $g_s = 4$ and *para* states $g_s = 2$. Overall, there are roughly twice as many *para* states as there are *ortho* ones. At higher energies and level densities, where unambiguous assignment of levels to *ortho* or *para* is not possible, levels may be then assigned an *average* value of $g_s = 8/3$ (Sidhu, Miller, and Tennyson, 1992).

The energy level structure has important consequences for interstellar physics as discussed in Sec. IV (and shown there in Fig. 14). Spectroscopic transitions between *ortho* and *para* states do not occur, and the two nuclear-spin isomers follow different chemistries (Hily-Blant *et al.*, 2018). Mechanisms for interconversion between *ortho* and *para* H_3^+ have been the subject of considerable theoretical (Quack, 1977; Uy, Cordonnier, and Oka, 1997; Oka, 2004; Suleimanov *et al.*, 2018) and experimental study (Cordonnier *et al.*, 2000; Gerlich, Herbst, and Roueff, 2002; Grussie *et al.*, 2012), in part stimulated by the observation that in some interstellar environments *ortho* and *para* H_3^+ appear to exist at different temperatures (Crabtree *et al.*, 2011). (SeeSec. III for a more detailed discussion of the spectroscopic consequences of these properties.)

Mention should be made of the somewhat unusual topology of the H_3^+ potential energy surface (PES). Although the system is triangular at its equilibrium structure, linear geometries can be accessed at relatively low energies (Gottfried, 2006). Above the barrier to linearity classical calculations on the surface show that most of it is chaotic (Velilla *et al.*, 2008), although both classical (Gomez Llorente and Pollak, 1988) and quantum-mechanical studies (Brass, Tennyson, and Pollak, 1990) show that regular motions persist to dissociation, and possibly beyond. The high-energy motion, for which the name *horseshoe* has been coined due to the shape of regular classical trajectories, involve one proton passing

TABLE I. The absolute nonrelativistic electronic energy for H_3^+ in an equilibrium triangle configuration with $r = 1.65a_0$, as calculated using methods of increasing accuracy. Given are the quoted absolute energy (with uncertainty in parenthesis) and the difference in this energy for a calculation relative to the estimated exact answer ΔE. The name of the associated potential energy surface (PES) is given where relevant. Anderson (1992) gave a comprehensive list of calculations performed prior to 1990.

Method[a] (PES)	Reference	Energy (E_h)	ΔE (cm^{-1})
CI with GTOs (MBB)	Meyer, Botschwina, and Burton (1986)	−1.343 40	160
CI R12	Röhse *et al.* (1994)	−1.343 835(1)	0.1
Quantum Monte Carlo	Anderson (1992)	−1.343 835(1)	0.005
ECG (Cencek)	Cencek *et al.* (1998)		0.04
ECG (Bachorz)	Bachorz *et al.* (2009)		0.02
ECG	Pavanello and Adamowicz (2009)	−1.343 835 625 02	0.000 02
ECG (GLH3P)	Pavanello *et al.* (2012)	−1.343 835 599	0.006

[a]CI, configuration interaction; ECG, explicitly correlated Gaussian functions.

between the other two. Quantum mechanically this motion correlates with bending motion below the barrier to linearity (Le Sueur, Henderson, and Tennyson, 1993).

Another interesting topological feature on the H_3^+ surface is the presence of a seam (Aguado *et al.*, 2000), where surfaces connecting the two dissociation limits that can be reached from the ground state surface, namely, $H_2 + H^+$ or $H_2^+ + H$, cross. The effects of this feature are currently being probed experimentally (Urbain *et al.*, 2019). At long range the $H_2 + H^+$ interaction behaves as an ion quadrupole and falls off as R^{-4}, where R is the distance between the proton and the H_2 center of mass. The long-range nature of the potential is augmented by the fact that the zero point energy of H_2 is large, about 2000 cm^{-1} (~0.25 eV). In classical terms this leaves a large volume of phase space available for supporting long-range states of the system. Calculations suggest that there are indeed long-range or asymptotic vibrational states of the system (Munro, Ramanlal, and Tennyson, 2005), although the true extent and nature of these remains to be determined.

B. High-resolution spectroscopy

Spectroscopically H_3^+ has no observed electronic bands and, despite theoretical predictions for the low-lying, metastable $^3\Sigma_u^+$ state (Friedrich *et al.*, 2001), there are no assigned transitions within any excited electronic states. Again, despite long-standing theoretical predictions (Pan and Oka, 1986; Miller and Tennyson, 1988a), the pure rotational spectrum of H_3^+ has yet to be observed either in the laboratory or in space. As H_3^+ does not have a permanent dipole moment, the predicted transitions gain intensity due to distortions of the molecule when it rotates; these distortions lead to an instantaneous dipole. Even with this, some states do not have a decay route, leading to dramatic differences in the natural lifetimes of even nearby rotationally excited states of the system (Mizus *et al.*, 2017). Conversely the permanent dipole moments of the deuterated species H_2D^+ and D_2H^+ result in pure rotational spectra that are well characterized in the laboratory (Furtenbacher, Szidarovszky, Fábri, and Császár, 2013) and have been observed in space (Caselli *et al.*, 2003; Harju *et al.*, 2017).

This leaves the IR spectrum, which is driven by changes in the vibrational state. Even here things do not look initially promising. H_3^+ has only two vibrational modes, a degenerate bending mode ν_2 and a symmetric stretching mode ν_1, which has no dipole associated with it and thus should be IR forbidden. Rotation-vibration transitions in the ν_2 band were eventually detected by Oka (1980).

We now outline the notation used to describe spectra of H_3^+. This is derived from the effective Hamiltonian developed by Watson (1984) for symmetric top molecules such as H_3^+; Lindsay and McCall (2001) also suggested a notation for assigning H_3^+ that differs in details not considered here. We refer the interested reader to either of these works for a fuller discussion. A list of H_3^+ vibrational levels and bands, with their associated energies and Einstein A_{if} emission coefficients, useful for astrophysical purposes,was given by Dinelli, Miller, and Tennyson (1992).

The two H_3^+ vibrational modes are as follows:

(1) The symmetric stretch (breathing) mode ν_1 (which is associated with the quantum number v_1) that retains the D_{3h} symmetry; transitions that involve only a change in v_1 alone are not strictly speaking IR allowed;

(2) The asymmetric stretch-bend mode ν_2 (which is associated with the quantum number v_2) that changes the symmetry produces a transition dipole moment and is therefore IR allowed. ν_2 is also associated with a *vibrational angular momentum* quantum number l_2, which has values $-v_2, -v_2+2, \ldots, v_2-2, v_2$. For $v_2 = 1$, l_2 has values ± 1; for $v_2 = 2$, l_2 has values of 0 and ± 2. $l_2 = \pm 1$ gives rise to a doubly degenerate vibrational level: $v_2 = 1$, $l_2 = +1$ is equivalent to $v_2 = 1$, $l_2 = -1$. This is also true for $l_2 = \pm 2$. For vibrational levels with l_2 exactly divisible by 3 (e.g., $l_2 = \pm 3, \pm 6, \ldots$) the $+l_2$ level is now not degenerate with the $-l_2$ level, and two separate vibrational levels result. Nonetheless, l_2 is sometimes replaced by $L_2 = |l_2|$.

A vibrational level may be designated by the three quantum numbers v_1, v_2, and l_2, often given compactly as $(v_1, v_2^{l_2})$. The fundamental asymmetric stretch-bend band ν_2 involves a transition between $v_2 = 0$ and $v_2 = 1$; since the lower level is the ground vibrational state, it is often not specified as such, and since l_2 can only be ± 1 it too is often not specified; the whole band may then be abbreviated as ν_2. A "hot band" involves a transition between $v_2 = n+1$ and $v_2 = n$: the most observed hot band astronomically is $(v_2 = 2) \rightarrow (v_2 = 1)$ [see Stallard *et al.* (2002)]; since transitions from both $l_2 = 2$ and $l_2 = 0$ are allowed, one usually specifies the $2\nu_2(l_2 = 2)$ or the $2\nu_2(l_2 = 0)$ component of the band. But one must also consider the transitions from $(1, 1^{\pm 1})$ to $(1, 0^0)$, which is also an allowed hot band. An overtone band results when $\Delta v_2 = 2$, such as the first astronomically observed H_3^+ lines in the $(v_2 = 2) \rightarrow (v_2 = 0)$ band, often referred to as the $2\nu_2$ overtone. Selection rules also require that $\Delta l_2 = \pm 1, \pm 2$, etc.; the transitions observed by Drossart *et al.* (1989) from Jupiter were from the $(0, 2^{\pm 2}) \rightarrow (0, 0^0)$ overtone band. $\Delta l_2 = 0$ transitions are not allowed, but "forbidden" transitions do occur (discussed later). "Hot overtones" from $v_2 = 3$ to $v_2 = 1$ have also been observed on Jupiter (Raynaud *et al.*, 2004). Table II lists the term values (energies) of the vibrational states involved in observed rovibrational spectra.

Two more types of bands need to be mentioned: difference bands and forbidden bands. For example, the transition from $(1, 0^0)$ to $(0, 1^{\pm 1})$ is allowed since $\Delta l_2 = 1$: this is often referred to as the $\nu_1 - \nu_2$ difference band. But the transition from $(2, 1^{\pm 1})$ to $(1, 1^{\pm 1})$ should not be allowed since $\Delta l_2 = 0$. Nonetheless, this "forbidden band," which becomes IR active through processes variously called *intensity borrowing* or *vibrationally induced dipole*, has been both calculated (Miller, Tennyson, and Sutcliffe, 1990) and observed (Xu *et al.*, 1992).

In its vibrational ground state $(0, 0^0)$ and in other states for which $l_2 = 0$, H_3^+ has the angular momentum quantum number J and k, where J is the total angular momentum and k is the projection of J on the C_3 symmetry axis. k can

TABLE II. Lowest term values (LTVs) for the observed vibrational states of H_3^+ of symmetry Γ. For vibrational states of A_2' or E' symmetry this is the $J = 0$ state and for A_1' states it is $J = 1$ state. Empirical values, where available, are taken from Furtenbacher, Szidarovszky, Mátyus *et al.* (2013) and are given to four decimal places; otherwise, predicted values given to two decimal places are taken from Mizus *et al.* (2017).

v_1	v_2	L_2	Γ	LTV ($\times$cm^{-1})
0	0	0	A_1'	64.1210
0	1	1	E'	2521.4083
1	0	0	A_1'	3240.7380
0	2	0	A_1'	4842.6070
0	2	2	E'	4998.0479
1	1	1	E'	5554.0610
2	0	0	A_1'	6323.07
0	3	1	E'	7005.97
0	3	3	A_2'	7492.9112
1	2	0	A_1'	7571.86
1	2	2	E'	7870.23
2	1	1	E'	8488.01
0	4	4	E'	9997.18
2	2	0	A_1'	11026.29
2	2	2	E'	10645.3770
0	5	1	E'	10862.9007
3	1	1	E'	11323.0960
0	5	3	A_2'	11529.24
0	5	5	E'	11658.3970

take values $-J$, $(-J+1)$, …, $J-1$, and J, with values of $-k$ and k equivalent; hence, $K = |k|$ is used. States with $K = 0, 3, 6, \ldots$ are *ortho* states with a spin weighting $g_s = 4$; those with K not exactly divisible by 3 are *para* states, with $g_s = 2$. This is essential when considering the relative strength of transitions since *ortho* lines are roughly twice as intense as *para* lines with similar absorption or emission coefficients, once relative level populations have been accounted for. This can make a considerable difference to the detectability of lines in astronomical sources. Spectroscopic transitions between *ortho* and *para* states are strictly forbidden.

For the rotational component of a dipole-mediated transition, such as the IR spectrum of H_3^+, the selection rules are $\Delta J = 0, \pm 1$; $\Delta K = \pm 1$. Transitions for which upper and lower levels have the same value of J, i.e., $\Delta J = 0$, form the Q branch of the spectrum. The P branch has $\Delta J = -1$; the upper level has a value of $J' = J - 1$, where J is the angular momentum quantum number of the lower level and J' of the upper level. The R branch has $\Delta J = +1$. In general, Q-branch transitions cluster around the central frequency of a band (the *band origin*) with P-branch lines at increasingly lower frequencies and higher wavelengths as J increases. R-branch lines are at higher frequencies and lower wavelengths than the band origin, increasing in frequency with high J until a critical value of J is reached. After that, increasing J values have lower frequencies than those of the critical J, creating a "band head." Manifolds of rotational lines with the same value of J may be grouped as $P(J)$, $Q(J)$, and $R(J)$, depending on the value of ΔJ involved; see Tennyson (2019) for a further detailed discussion.

For vibrationally excited levels with $l_2 \neq 0$, K no longer suffices and a new quantum number $G = K - l_2$ is used to take into account the vibrational angular momentum and define the J manifold. If we take the level with $v_2 = 1$ and $J = 3$, for example, we can combine $K = 3$ with $l_2 = -1$ to get the rotational state $J = 3$, $G = 4$; if we combine $K = 3$ with $l_2 = +1$, we get the rotational state $J = 3$, $G = 2$. But we can also generate the values $J = 3$ and $G = 2$ by combining $K = 1$ with $l_2 = -1$. Another quantum number, $U = -l_2$, is then often used so that rotational sublevels in vibrationally excited states with $l_2 \neq 0$ have the designations (J, G, U). The rotational level $J = 3$, $G = 4$, $U = +1$ is clearly unique. The level $J = 3$, $G = 2$, $U = +1$ is different from $J = 3$, $G = 2$, $U = -1$ since they are generated from different underlying values of K: in the first case, $K = 1$; in the second case, $K = 3$. H_3^+ rovibrational states are thus fully designated by the notation $(v_1, v_2, l_2)\,(J, K/G, U)$, where U is not required when $l_2 = 0$.

There can be further simplifications in notation: for example, planetary scientists have made considerable use of the ν_2 $Q(1, 0^-)$ line at 3.953 μm. The superscript $-$ indicates that the upper level has a value of $U = -1$; since in the upper level $K = 1$, the resulting value of G is 0. The $2\nu_2$ $R(6, 6^+)$ detection at 2.093 μm, one of the strongest of the original H_3^+ Jupiter line detections (Drossart *et al.*, 1989), has $J' = 7$ and $K' = 7$ and, with the $+$ superscript indicating $U = +2$, $G = 9$.

The IR spectrum of H_3^+ has proven to be surprisingly rich in part because of the strength of its overtone bands (Miller and Tennyson, 1988b) and its so-called forbidden transitions (Miller, Tennyson, and Sutcliffe, 1990; Xu *et al.*, 1992). Lindsay and McCall (2001) and Furtenbacher, Szidarovszky, Mátyus *et al.* (2013) both present comprehensive compilations and evaluations of the available high-resolution spectroscopic data on H_3^+. These have been augmented by recent ultrahigh (submegahertz) accuracy studies (Perry *et al.*, 2015; Guan *et al.*, 2018; Markus and McCall, 2019). Currently, the highest assigned H_3^+ line is at 16 660.240 cm^{-1}, determined by Berg, Wolf, and Petrignani (2012), which is not even half the dissociation energy.

These ultra-high-resolution studies provide the benchmark results against which *ab initio* calculations can be calibrated. As a two-electron system it is possible to get a highly accurate solution to the H_3^+ electronic structure problem. Table I summarizes recent progress in obtaining the absolute, nonrelativistic electronic energy. It can be seen that methods that used specialist procedures based on lengthy expansions of explicitly correlated Gaussian functions (Pavanello and Adamowicz, 2009) have led to electronic energies converged to ten significant figures, albeit at the cost of many months of computer time for a single molecular geometry. While this level of accuracy still does not match that achieved for H_2 (Korobov, 2006), the real difficulties occur when other effects are also considered.

A complete solution of the H_3^+ problem requires consideration of relativistic effects, nuclear motion, and Born-Oppenheimer breakdown, both diagonal (adiabatic) and nonadiabatic. The relativistic correction to the electronic energy of H_3^+ is fairly small (∼2–4 cm^{-1}); relativistic correction

surfaces were computed by Cencek *et al.* (1998) and Bachorz *et al.* (2009). In particular, Bachorz *et al.* (2009) used the complete Breit-Pauli relativistic Hamiltonian and thus considered mass-velocity, one- and two-electron Darwin contributions, Breit retardation, and a spin-spin Fermi contact term. To this correction can be added a further correction due to QED that was estimated by Lodi *et al.* (2014) to be in the range -0.4 to $+0.6$ cm^{-1} in spectroscopically important regions of the PES.

While the H_3^+ nuclear motion problem can be solved to high accuracy in the spectroscopically important region of the PES (Pavanello *et al.*, 2012), dealing with the breakdown of the Born-Oppenheimer approximation is altogether more difficult. The adiabatic or Born-Oppenheimer diagonal correction can be computed accurately in a straightforward manner (Dinelli, Le Sueur *et al.*, 1995; Pavanello *et al.*, 2012). Attempts to perform full calculations without making the Born-Oppenheimer approximation, which work well for H_2 (Jones, Formanek, and Adamowicz, 2017), struggle to give good results for H_3^+ (Muolo, Mátyus, and Reiher, 2019). For example, a recent study by Muolo, Matyus, and Reiher (2018) gave vibrational fundamentals with errors of about 15 cm^{-1}. Conversely, Polyansky and Tennyson (1999) developed a beyond the Born-Oppenheimer approximation model based on the use of a single effective vibrational mass optimized for calculations on H_2^+ by Moss (1996). This model reproduced the observed transition frequencies for all isotopologues of H_3^+ to about 0.05 cm^{-1}, although subsequent work (Polyansky *et al.*, 2012) suggested that some of this accuracy was due to a fortuitous cancellation of errors. Work on developing a tractable and accurate method of treating nonadiabatic effects in H_3^+ continues (Diniz *et al.*, 2013; Jaquet and Khoma, 2018; Amaral *et al.*, 2019), but it remains an unsolved problem.

One of the issues that make *ab initio* calculations on triatomic H_3^+ more difficult than those on the isoelectronic H_2 molecule is, at least within the Born-Oppenheimer approximation, the issue of PES fitting. Electronic structure calculations are performed on a grid of points. These points need to be interpolated for use in nuclear motion calculations; this is usually achieved by fitting to a suitable functional form. To retain the accuracy of the underlying electronic structure calculations it is important to do this carefully, something that is not always achieved in practice (Polyansky *et al.*, 2012). Furthermore, the construction of global surfaces remains challenging (Mizus *et al.*, 2019). An accurate global PES is required to study the exquisitely detailed but still unassigned near-dissociation spectra of H_3^+ and its isotopologues (Carrington, Buttenshaw, and Kennedy, 1982; Carrington and Kennedy, 1984; Carrington, McNab, and West, 1993), which are discussed in Sec. II.C. Similar global surfaces are needed to study reactive scattering problems such as $D^+ + H_2 \rightarrow HD + H^+$, although for such problems we note that the long-range interactions can reliably be represented in terms of multipole interactions (Velilla *et al.*, 2008).

H_3^+ transition intensities are important for all of the remote sensing applications discussed elsewhere in this review. Given that H_3^+ is usually created in nonthermalized plasma conditions, measurements of absolute transition intensities are difficult. Thus far the most that measurements have yielded involves only ratios of transition intensities between different bands (Farnik *et al.*, 2002; Petrignani *et al.*, 2014) rather than direct measurement of the absolute intensities required for remote sensing applications. This means that a quantitative spectral analysis relies on computed transition intensities. To meet this demand a number of line lists have been constructed (Kao *et al.*, 1991; Neale, Miller, and Tennyson, 1996; Sochi and Tennyson, 2010; Mizus *et al.*, 2017), all of which used *ab initio* transition intensities, and it is on these that the astronomical studies discussed later rely.

There are a number of side products of these line list calculations. Partition functions (Neale and Tennyson, 1995; Mizus *et al.*, 2017) are needed for spectral synthesis and are important for models of cool hydrogen-dominated stellar atmospheres, such as those of old Population III stars [probably the oldest stars still existing in the Universe and created during the first wave of star formation when heavier elements had still to be generated (Saumon and Jacobson, 1999)], where the abundance of H_3^+ controls that of H^-, which is a key opacity source. Temperature-dependent cooling functions (Miller *et al.*, 2013) are important for models of planetary atmospheres and possibly studies of the Early Universe and, finally, state-dependent radiative lifetimes (Tennyson *et al.*, 2016) are important for astronomical and other studies, some of which are discussed later.

C. States at dissociation

In the early 1980s Carrington, Buttenshaw, and Kennedy (1982) announced the detection of a truly remarkable spectrum of H_3^+. Using the setup depicted schematically in Fig. 1 they bombarded molecular hydrogen with electrons and extracted H_3^+ from the resulting plasma using a mass spectrometer. The H_3^+ then traveled along a drift tube and light from a CO_2 laser was shone along the beam. A spectrum was recorded by detecting the flux of protons at a mass spectrometer with and without the laser beam as a function of the laser wavelength. A later example of this spectrum is shown in Fig. 2.

A series of subsequent studies by Carrington and Kennedy (1984), Carrington and McNab (1989), and Carrington, McNab, and West, 1993, as well as Alvarez *et al.* (2000), Kemp, Kirk, and McNab (2000), and Yousif *et al.* (2001), elucidated the nature of the spectrum. In the range of the CO_2 laser (874–1094 cm^{-1}) it proved possible to detect some 27 000 distinct spectral lines of H_3^+ (Carrington, McNab, and West, 1993) by monitoring proton fluxes. Experimental tests showed that these lines are reproducible and due to absorption of a single photon. They are generally narrow but, as can be seen in Fig. 2, some transitions show distinct broadening due to lifetime effects. Furthermore, Carrington, McNab, and West (1993) used a retarding field to deflect the protons emitted below a given kinetic energy; they showed that protons could be produced in the photodissociation process with as much as 3000 cm^{-1} excess kinetic energy. This observation was subsequently confirmed by Alvarez *et al.* (2000).

The production of protons by shining IR laser light on a sample of a mass-selected H_3^+ beam indicates that the laser was causing the ion to dissociate. However, the dissociation

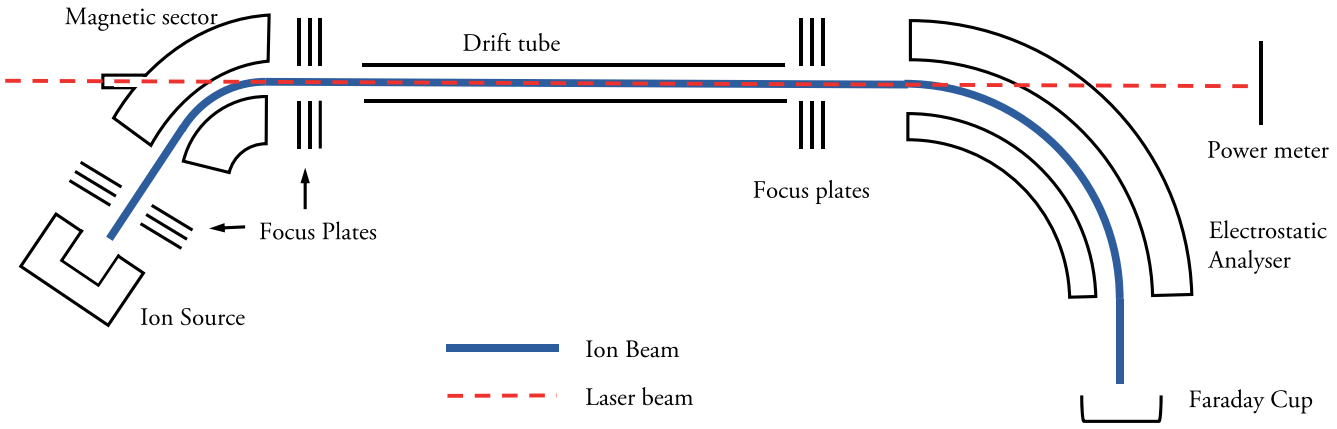

FIG. 1. Schematic diagram of depicting the key elements of the experiment of Carrington *et al.* used to probe the near-dissocation states of H_3^+ and its isotopologues.

energy (D_0) of H_3^+ is $35\,076 \pm 2$ cm^{-1} (Mizus *et al.*, 2019). Thus it is clear that if absorbing photons of a frequency of around 1000 cm^{-1} caused fragmentation, then the dissociating state must occur near the dissociation limit. Indeed, for those states whose kinetic energy release was observed to be greater than the energy carried by the absorbed photon, even the initial state has to have been above the dissociation limit. What these experiments reveal is that there is a rich and complex set of quasibound or resonance states that lie above the H_3^+ dissociation limit.

One intriguing observation made by Carrington and Kennedy (1984) followed from their convolving the strongest 1934 lines observed in the 872–1094 cm^{-1} laser window with a Gaussian of FWHM of 4 cm^{-1}. This yields a pseudo-low-resolution spectrum that is dominated by four strong peaks separated by about 30 cm^{-1}. A semiclassical analysis by Gomez Llorente and Pollak (1988) suggested that this structure could be associated with the regular horseshoe motion discussed previously.

A further semiclassical analysis of the spectra produced by the various isotopologues of H_3^+ gave some insight into the nature of the resonance states involved (Berblinger, Schlier, and Pollak, 1989). This analysis suggests that the observed initial states are shape resonances, that is, quasibound rotationally excited states that are trapped behind a centrifugal barrier. It would seem that the dense spectrum obtained due to photons emitted with low kinetic energy release arise from states with relatively low levels of rotational excitation (perhaps $J = 5$ to 10). Conversely, the high kinetic energy release spectrum has relatively few lines which appear to come from states with higher rotational excitation (perhaps $J > 20$). Thus far none of the many lines in the various near-dissociation spectra that have been recorded have any sort of spectral assignment. Theoretical studies have struggled to match the large number of lines observed in the near-dissocation region (Henderson and Tennyson, 1996), and it would seem that the sparser, high kinetic energy release spectrum would make a more promising starting point for such a study.

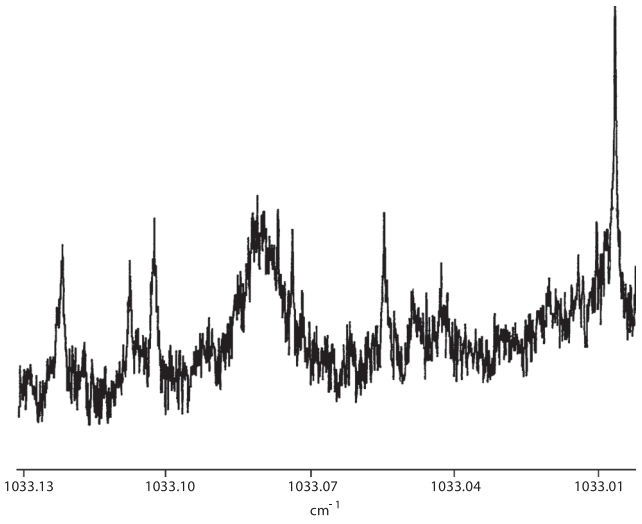

FIG. 2. A small section of the H_3^+ photodissociation spectrum.. From Kemp, Kirk, and McNab, 2000.

More recently Grechko *et al.* (2010) used multiphoton spectroscopy to study the spectrum of water in the near-dissociation region as a continuation of their studies characterizing the states of water up to dissocation (Grechko *et al.*, 2009). This work appears to identify a mixture of shape and Feshbach resonances. The use of multiphoton spectroscopy allows greatly simplified analysis of the near-dissociation spectrum, as only the observed lines must obey rotational selection rules that start from the initial (fully assigned) transition; combined with the use of laser polarization and multiple spectra that access the same final state it is possible to give definite rotation assignments to the resonance state. This greatly facilitates attempts to build theoretical models of the states above dissociation (Zobov *et al.*, 2011; Szidarovszky and Csaszar, 2013). The use of a similar multiphoton approach is perhaps the best hope for disentangling the large number of H_3^+ resonance states observed by Carrington and co-workers.

D. Creation and destruction

H_3^+ is formed rapidly in hydrogen plasmas through the process

$$H_2 + H_2^+ \rightarrow H_3^+ + H, \quad (1)$$

which occurs on timescales determined by the Langevin rate coefficient, i.e., essentially at every collision. Indeed, recent measurements suggest that the rate is even faster than Langevin at higher temperatures (Savić, Schlemmer, and Gerlich, 2020).

This makes H_3^+ the dominant hydrogenic ion in cold hydrogen plasmas, which include the interstellar clouds, and in cool stars. This reaction, first recognized by Hogness and Lunn (1925) from laboratory studies of H_3^+ in hydrogen discharges, has no energy barrier and possesses a large Langevin cross section of hundreds of $Å^2$, whose rate varies with temperature as $T^{-1/2}$. H_3^+ is an efficient protonator of many species, which leads to it driving much of the chemistry of the ISM (Herbst and Klemperer, 1973; Watson, 1973b). Furthermore, the energy differences between the lowest allowed rovibrational states of H_3^+, H_2D^+, D_2H^+, and D_3^+ (Ramanlal, Polyansky, and Tennyson, 2003) lead to significant fractionation effects, particularly at low temperatures (Millar, Bennett, and Herbst, 1989; Gerlich, Herbst, and Roueff, 2002; Walmsley, Flower, and Pineau des Forêts, 2004); this has led to the need to construct isotopologue-dependent chemistries (Majumdar *et al.*, 2017; Caselli, Sipilä, and Harju, 2019).

In most plasmas, however, a major destruction route for H_3^+ is via the process of dissociative recombination (DR):

$$H_3^+ + e^- \rightarrow H_2 + H \quad \text{or} \quad H + H + H. \tag{2}$$

As discussed later, the rate coefficient for low-energy DR of H_3^+ is important not only for interstellar and planetary atmosphere chemistry but also for the determination of the local cosmic-ray ionization rate.

In recent decades the DR rate coefficient for H_3^+ has proved somewhat controversial and has resulted in approximately 50 independent experimental attempts to determine it; see Kreckel *et al.* (2012). Conventional theory decrees that rapid DR occurs via a curve crossing between one or more neutral resonance states, often denoted as H_3^{**}, and the ion ground state (Tennyson, 1996). There are no such crossings at low energy for H_3^+ (Bates, Guest, and Kendall, 1993). Flowing afterglow measurements by Smith and Adams (1987) found the H_3^+ DR rate coefficient "to be immeasurably small" or less than 10^{-11} cm^3 s^{-1}, which led to the idea that DR of H_3^+ was an intrinsically slow.

The idea of slow H_3^+ DR, while supported by other afterglow experiments [see Glosik *et al.* (2001), Plašil *et al.* (2002) and references therein] soon began to be challenged. A spectroscopic technique used by Amano (1988) suggested a rate coefficient some 10 000 times greater than the upper limit of Smith and Adams (1987). Experiments performed in ion storage rings (Sundstrom *et al.*, 1994; McCall *et al.*, 2003, 2004) also supported this higher rate coefficient.

Originally theory struggled to find a mechanism that would lead to rapid DR for H_3^+ (Schneider, Orel, and Suzor-Weiner, 2000). However, Kokoouline, Greene, and Esry (2001) proposed a mechanism based on the inclusion of the nonadiabatic Jahn-Teller symmetry-distortion effect, which had been neglected in previous studies. Calculations using this method (dos Santos, Kokoouline, and Greene, 2007) concluded that the DR rate coefficient was indeed high and gave similar results to those obtained in storage ring experiments. This effectively settled the argument over the magnitude of the H_3^+ DR rate coefficient (Larsson, McCall, and Orel, 2008; Johnsen and Guberman, 2010).

We note, however, that the isoelectronic HeH^+ system, which also does not have any appropriate curve crossings, undergoes unexpectedly rapid DR (Yousif and Mitchell, 1989) that was recently shown to be rotational-state dependent (Novotný *et al.*, 2019). The rapid rate of DR can be successfully explained theoretically by invoking nonadiabatic coupling effects (Guberman, 1994; Sarpal, Tennyson, and Morgan, 1994). It would seem that this nonadiabatic mechanism (which involves couplings when the nuclei are close together) probably governs the rate coefficient of low-energy DR for both systems. Hence, there is no requirement to invoke the symmetry-specific Jahn-Teller effect for H_3^+. The recommended rate coefficient for H_3^+ DR is that first given by Sundstrom *et al.* (1994) of 1.15×10^{-7} cm^3 s^{-1} at 300 K, with a product branching ratio of $(H + H + H) : (H_2 + H)$ of 3 : 1.

While there is now general agreement on the DR rate coefficient for H_3^+, there are a number of remaining issues. First, careful studies by Glosik *et al.* (2015) showed that low H_3^+ dissociation yields measured in afterglow experiments are a consequence of three-body processes occurring in the plasma. These observations reconcile the afterglow measurements with the ones obtained in storage rings and by theory. Second, despite agreement on the general magnitude of the DR rate coefficient, it was still found that different measurements gave subtly different H_3^+ rate coefficients (Kreckel *et al.*, 2012). A major driver for the use of storage rings to perform DR experiments is that storing ions in the ring for seconds or even minutes prior to performing experiments should allow the ions to cool into their ground state, or perhaps some thermal distribution controlled by the blackbody radiation in the ring.

However, detailed study of the DR measurements showed the that H_3^+ did not cool in the manner anticipated; in particular, H_3^+ populations were observed to get trapped in rotationally excited states of the molecule (Kreckel *et al.*, 2002). This behavior could be modeled using calculated spectroscopic line lists (Kreckel *et al.*, 2004). The most recent calculations suggest that the high symmetry and resulting restrictive selection rules of H_3^+ lead to an unusually large number of states that cannot decay radiatively. Mizus *et al.* (2017) found such metastable states with a rotational quantum number $J \leq 19$. The highest of these states lies at 8509 cm^{-1} (more than 1 eV) above the ground state of the system. The trapping of a population in the metastable ($J = 3, K = 3$) state has been observed astronomically (Goto *et al.*, 2002) and has been the subject of a number of astronomical studies that we discuss later.

A conclusion from this is that for a full modeling of interstellar H_3^+ it is necessary to determine state-dependent DR rate coefficients. Some work in this direction has already been performed (Kreckel *et al.*, 2005, 2010), and a full solution to this problem is a major objective of the recently commissioned cryostatic storage ring in Heidelberg, Germany

(Kreckel, Novotny, and Wolf, 2019); see the recent results for the isoelectronic HeH^+ ion from Novotný *et al.* (2019).

III. PLANETARY SCIENCE

A. Introduction

Many of the key questions that H_3^+ studies of planets would go on to address had already been raised in the decades prior to its eventual direct spectroscopic identification in the auroral ionosphere of Jupiter (Drossart *et al.*, 1989). Alongside this, many of the tools and models needed to address these questions had also been developed, at least in embryo. Both modeling studies (Atreya, Donahue, and McElroy, 1974; Atreya and Donahue, 1975) and *Voyager* flybys (Hamilton *et al.*, 1980; Krimigis *et al.*, 1982) had suggested that the upper atmospheres (the ionospheres) of the giant planets would be sources of the H_3^+ molecule. In the three decades since they were first detected, planetary H_3^+ emissions have been used to map the effects of incoming energetic particles and photons, to measure upper atmosphere temperatures and ion densities, to monitor ion winds, and to calculate heating and cooling rates and the overall energy balance. As the largest planet in the Solar System and the most dynamic, Jupiter is the focus for much of what follows. But the other gas giants repay close study if only because they enable us to carry out comparative planetology that may prove useful for studying other (exo)planetary systems.

To assist understanding here, we begin with a short introduction to key planetary and space science concepts, based on standard descriptions such as those found in Dessler (1983) and Kivelson and Russell (1995). The giant planets of the Solar System (Jupiter, Saturn, Uranus, and Neptune) are all strongly magnetized and interact with the solar wind, a stream of energetic particles (electrons and protons) that flow out from the Sun at velocities of up to 700 $km\,s^{-1}$, to create a magnetosphere under the control planet's own magnetic field. This magnetosphere is compressed in the Sun-ward direction by the impact of the solar wind, forming first a bow shock and then the magnetopause, where the dynamic pressure of the solar wind is balanced by the magnetic pressure of the planet's own field. In the anti-Sun-ward direction, the solar wind drags the planet's magnetic field downstream until it becomes indistinguishable from the ambient interplanetary space field. This creates a magnetosphere whose shape is variously described as "tadpolelike" or "cometlike."

The magnetosphere interacts with the planet itself through the ionosphere, the part of the upper atmosphere that is ionized by solar ultraviolet (UV) radiation, which in turn couples to the coexisting and colocated thermosphere, where the temperature increases monotonically with altitude before reaching a nearly steady value. This region extends upward from the homopause, the point at which the planet's atmosphere is no longer convectively mixed and individual species concentrations depend on their atomic or molecular weights, to base of the exosphere, where, at its outermost reaches, the gas becomes indistinguishable from the gases of the magnetosphere and interplanetary space; see, for example, Sanchez-Lavega (2011), especially Chap. 6, for a basic introduction to planetary atmospheres.

The magnetosphere of Jupiter became a major focus of interest at the time of, and as a result of, the *Voyager* crafts; see, e.g., Smith, Davis, and Jones (1976), Armstrong *et al.* (1981), Gehrels, Stone, and Trainor (1981), and Acuna, Behannon, and Connerney (1983). Energetic H_3 entities had been found by *Voyager 2*'s Low-Energy Charged Particle instrument in Jupiter's magnetosphere (Hamilton *et al.*, 1980, 1981) and in Saturn's magnetosphere (Krimigis *et al.*, 1982; Hamilton *et al.*, 1983). Pre-*Voyager* models suggested that H_3^+ would reach peak number densities of $< 10^{10}$ m^{-3} at around 180 km altitudes for Jupiter (Atreya, Donahue, and McElroy, 1974) and about 10^9 m^{-3} at similar altitudes, around 150 km, for Saturn and Uranus, but less than half that density for Neptune (Atreya and Donahue, 1975). More sophisticated models from Waite *et al.* (1983) made similar but more detailed predictions of the vertical distributions of ions and neutral species. Of future interest was a variation by Connerney and Waite (1984) that calculated the effect of "ring rain," an influx of water and waterlike molecules derived from the rings, on Saturn's lower latitude and equatorial ionosphere. For Uranus, Chandler and Waite (1986) predicted that H_3^+ densities could reach peaks of 10^{10} m^{-3}. Thorne (1982) drew attention to the importance of wave-particle scattering for precipitating energetic ions into the Jovian upper atmosphere, potentially giving rise to auroral emission.

Spacecraft in orbit around Jupiter measured plasma flows, densities, and compositions, revealing an enormous and rapidly rotating structure held together by the planet's magnetic field. An equatorial plasma sheet, fed by the volcanos of the Galilean moon Io at a rate of ~1000 $kg\,s^{-1}$, was swept into corotation as the planet's magnetic field rotated through it at a rate of 1.76×10^{-4} $rad\,s^{-1}$ (Connerney, Acuna, and Ness, 1981). As the sheet spread out past 15 times the radius of Jupiter ($15\ R_J$; $1\ R_J = 71\,492$ km) its angular velocity reached close to 200 $km\,s^{-1}$. At this point, what Hill (1979) called an "inertial limit to corotation" was reached, the plasma sheet began to lag behind corotation with the planet and magnetic field lines were distorted, creating powerful current systems. These closed in the ionosphere and generated particle precipitation, an influx of electrically charged particles (electrons and positive ions) channeled along the magnetic field lines into the upper ionosphere. This, in turn, produced a high-latitude signature in the Jovian upper atmosphere in terms of a departure from corotation with the planet (Huang and Hill, 1989). The full significance of this for auroral activity, and, retrospectively, for the detection of the H_3^+ IR spectrum, would be appreciated only some two decades later.

Another key issue that became apparent as a result of spacecraft measurements was that of energy balance in the upper atmospheres of the giant planets. *Pioneer 10* had shown Jupiter to have an effective temperature in the lower atmosphere of ~125 K (Ingersoll *et al.*, 1975). Strobel and Smith (1973) calculated that the temperature at the top of the atmospheres of Jupiter should therefore be between 150 and 170 K based on solar energy inputs, considerably less than the > 260 K derived from stellar occultation (Hubbard *et al.*, 1972). This indicated that the planet was emitting nearly

TABLE III. Observed and calculated homopause and exospheric temperatures in kelvins for the giant planets. Adapted from Yelle and Miller, 2004.

	Jupiter	Saturn	Uranus	Neptune
$T_{\text{homopause}}$	160	143	130	130
T_{exo} (observed)	940	420	800	600
ΔT_{exo} (observed)	780	277	670	470
T_{exo} (calculated)	203	177	138	132
ΔT_{exo} (calculated)	43	34	8	2

twice as much thermal energy as it received from the Sun, creating an "energy gap" that needed to be explained. For Saturn, analysis of *Voyager* data gave upper atmospheric temperatures that ranged from 400 (Smith *et al.*, 1983) to 800 K (Waite *et al.*, 1983), both far higher than Strobel and Smith (1973) had predicted.

Resolving these differences for the giant planets would become even more problematic in later years; see Yelle and Miller (2004). The now-accepted observed and calculated temperatures for all of the giant planets are set out in Table III. The temperatures in the table refer to the bottom and top of the thermosphere, from the homopause ($T_{\text{homopause}}$) to the base of the exosphere (T_{exo}). Temperature differences are of the order of hundreds of kelvins between the value of T_{exo} calculated from the radiation balance and what is observed. These indicate just how large the energy gap is for each of the planets.

Between 1986 and 1989, Trafton *et al.* (1986, 1988) and Trafton, Lester, and Thompson (1989) reported IR spectra of Jupiter's auroral zones measured from the McDonald Observatory IR grating spectrometer (Lester, Harvey, and Carr, 1988) in Texas. The key focus of this work was to find auroral signatures from molecular-hydrogen emission that would correspond to the UV auroras already detected (Broadfoot *et al.*, 1979; Skinner *et al.*, 1984). These UV auroral features were the result of prompt emission from H_2 molecules and H atoms excited by energetic particles hitting the upper atmosphere; see Bhardwaj and Gladstone (2000) and references therein for a fuller discussion of UV emission from the giant planets at various wavelengths. In searching for H_2 auroral emission, they were successful.

Among the quadrupole-allowed H_2 emissions, however, were several strong features that Trafton's team could not identify (Trafton, Lester, and Thompson, 1989); see Fig. 3. Those features were shown, thanks to the much greater spectral resolution of the echelle spectrometer of the Canada France Hawaii Telescope (CFHT), and the greater altitude (~4200 m) and clearer skies of Maunakea, Hawaii, where it was situated, to be due to the H_3^+ molecular ion (Drossart *et al.*, 1989); see Miller (2018) for a fuller exposition of the identification of H_3^+ in the spectrum of Jupiter.

The detection of H_3^+ in the auroral ionosphere of Jupiter (Drossart *et al.*, 1989), as well as being unexpected and not searched for, came with three further surprises: first, that the lines came from an overtone band, when traditional spectroscopy predicted that overtone lines should intrinsically be much weaker than fundamental transitions (if not forbidden altogether); second, the emission lines were strong, as strong as the H_2 lines that were also present in the spectrum; and third, that the derived temperature $T(H_3^+)$, of 1000 to 1200 K was much higher than any models of the upper atmosphere were predicting.

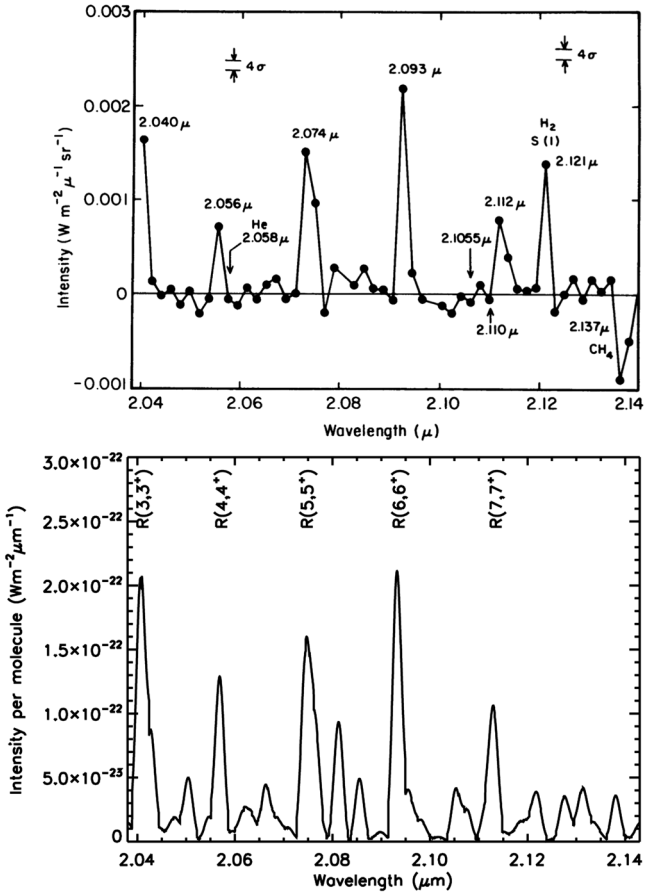

FIG. 3. Detected unidentified emission lines within Jupiter's auroral region among the quadrupole-allowed H_2 emissions. (Top panel) From Trafton *et al.*, these emission lines are well detected. (Bottom panel) A simulated spectrum using a temperature of 1200 K, the spectral resolution of the McDonald Observatory IR grating spectrometer ($\lambda/\Delta\lambda = 1200$) and the Neale, Miller, and Tennyson (1996) line list are shown for comparison, with the line assignments of the brightest five lines. From Trafton, Lester, and Thompson, 1989.

The explanation for the first of these surprises, that H_3^+ is a floppy molecule with Einstein A coefficients for many bands between 10 and > 100 s^{-1}, was dealt with in Secs. I and II.B. Nonetheless, the fact that overtone lines were detectable was a strong validation of the first-principles quantum-mechanical calculations that predicted, for example, that the $v_2 = 2 - 0$ $R(6, 6^+)$ transition at 2.093 μm should have $A_{if} = 151$ s^{-1}, making it intrinsically more than 3 times as likely to emit spontaneously than the $v_2 = 1 - 0$ equivalent $R(6, 6^+)$. This is important since it is not possible to measure ion populations in the discharge tubes used for H_3^+ spectroscopy, and thus the intrinsic strength of bands and individual lines has to be calculated from first principles. These line strengths then fed into calculations of ion density, of great importance when

trying to determine conductivity and various dynamic properties of the atmosphere.

The second of these surprises indicated that the actual column density $N(H_3^+)$ of excited H_3^+ ions should be relatively large; Drossart *et al.* (1989) calculated that there were around 10^{13} m^{-2} in the upper emitting vibrational band, which agreed with the *Voyager*-derived overall ion column density (Skinner *et al.*, 1984) of $> 5 \times 10^{16}$ m^{-2}, if a thermal population of H_3^+ ions at $T(H_3^+) = 1100$ K were assumed. Drossart *et al.* (1989) also raised the possibility that the $v_2 = 2$ level of H_3^+, transitions of which occurred at nearly the same frequencies as the $v = 1$ level of H_2, could be being resonantly populated by vibrational energy exchange with the neutral gas.

The third of the surprises meant (if the H_3^+ levels were simply populated thermally rather than by resonant vibrational energy exchange) that explaining the energy gap between solar inputs to the upper atmosphere and the now *in situ* measured temperature there had just become even more challenging.

Given the strength of the $2\nu_2$ overtone spectrum, it made perfect sense to look for the ν_2 fundamental spectrum. Lines of the H_3^+ overtone spectrum occur at wavelengths that fall in a transmission window of Earth's atmosphere that covers ~1.9–2.5 μm, known as the K window. This was reasonably transparent at the altitude of the McDonald Observatory (~2000 m). But the fundamental spectrum fell into the more challenging L window (L band, 3.0–4.2 μm), which was better accessed at the higher altitude of Maunakea. Three teams set out to study these lines using the telescopes on Maunakea: Maillard *et al.* (1990) detected the fundamental spectrum at relatively high resolution using the CFHT Cassegrain high-resolution Fourier transform spectrometer (Maillard and Michel, 1982) (resolving power $\lambda/\Delta\lambda \sim$ 10 000 or greater); Miller, Joseph, and Tennyson (1990) used the NASA Infrared Telescope Facility (IRTF) cooled grating spectrometer (Brown *et al.*, 1988) to measure the overtone and fundamental spectrum in quick succession at a resolution of ~1000; Oka and Geballe (1990) made use of the United Kingdom Infrared Telescope (UKIRT) cooled grating spectrometer (Chapman *et al.*, 1990) to probe the wavelength region around the ν_2 $J = 5$ manifold, again at high resolution.

The detection of H_3^+ in Jupiter also made it sensible to look for the ion in the atmospheres of other Solar System giant planets. In 1992, Trafton *et al.* used UKIRT's new cooled grating spectrometer (Mountain *et al.*, 1990) to observe Uranus. The result was a clean spectrum of H_3^+ that had almost none of the background seen in the spectrum of Jupiter with moderate ($\lambda/\Delta\lambda \sim 1000$ to 2000) resolution spectroscopy (Trafton *et al.*, 1993).

The Jupiter spectral background was due to thermal radiation, from either reflected sunlight or the Jovian lower atmosphere "leaking" through the absorbing stratospheric layers that contained otherwise opaque methane. The cleanness of the Uranian spectrum indicated that stratospheric methane concentrations (at lower altitudes) would be relatively higher than Jovian thus absorbing more of the planet's own thermal radiation from the lower atmosphere. It also meant that the planet's homopause was relatively low compared to that of Jupiter, giving a relatively longer column of nearly pure H_2 in which H_3^+ could form without being chemically removed by reactions with hydrocarbons. Later in 1992, Geballe, Jagod, and Oka (1993) detected H_3^+ emission from Saturn. This was about 40 times weaker than that at Jupiter, and weaker too than at Uranus. One explanation for this was that Saturn's homopause was relatively high compared to the other two planets, which meant that the column of nearly pure H_2 was shorter and the opportunities to form H_3^+, in conditions where reactions with hydrocarbons would not destroy it were less.

A comparison among the three planets showed that for Jupiter and Saturn emission was concentrated around the poles and thus mainly auroral in nature, while Uranus (much more difficult to resolve spatially as a result of its larger orbital radius and smaller size) seemed to have emission spread across the planetary disk. A stage was also set for time series studies and for the investigation of just how H_3^+ was distributed across each planetary disk as a function of geographical and magnetic longitude and latitude. We now look at the planets in turn.

B. Jupiter

1. The aurora

The H_3^+ emission seen by Drossart *et al.* (1989) was generated from molecules ionized in the upper atmosphere of Jupiter, the coexisting thermosphere and ionosphere. This is an atmospheric region where gases are not convectively mixed, so species settle out according to their respective atomic or molecular weights. Each species s of mass m_s has its own scale height given by $H_s = kT/m_s g$, where k is the Boltzmann constant, T is the local atmospheric temperature, and g is the local gravitational constant. The concentration of species s then falls off as $\exp(-h/H_s)$ with increasing altitude h. Thus, concentrations of hydrocarbons and other "heavy" molecules, abundant in the convectively mixed atmosphere *below* the homopause, fall off rapidly with increasing altitude such that the neutral thermosphere has a composition largely of H_2 and H, with some He.

For Jupiter, pressures in this region fall from ~10^{-6} bar (1 μbar) around 300 km above the cloud tops to less than 10^{-10} bar (0.1 nbar) at an altitude of 1000 km (Grodent, Waite, and Gérard, 2001). The temperature increases monotonically with altitude since energy is mainly input into the upper atmosphere from above as solar UV radiation, and in some regions energetic particle influxes, until a relatively constant exospheric temperature T_{exo} is reached. Similar conditions prevail on the other giant planets, for which hydrogen (atomic and molecular) is the main gas species. Photochemical dissociation of molecules also plays a role in creating lighter species at higher altitudes.

The spatial distribution of H_3^+ could be established by using long-slit spectrometers and either scanning the slit across the disk from north to south or allowing the planet to rotate under it if the slit itself was aligned north to south from pole to pole along the noon meridian. The former technique allowed for local-time effects to be studied at particular latitude ranges (since the slit spanned several latitudes); the latter was used to try to understand how the planet varied geographically at a

particular local time (noon). For studies of Jupiter's ionospheric-thermospheric morphology, it is most useful to use the coordinate system known as System III, as this is fixed to the planet's magnetic field, unlike Systems I and II, which are referenced to features in the lower atmosphere.

H_3^+ studies started at a time when new IR cameras were being developed that allowed for an instantaneous image of the whole (or at least a large part of the) disk. One of the first of these was ProtoCAM, which was developed for the NASA IRTF (Toomey *et al.*, 1990). Turned on Jupiter, ProtoCAM gave the first detailed images of the auroral-polar regions of the planet (Baron *et al.*, 1991; Kim *et al.*, 1991).

A useful, if not entirely rigorous, property of a planetary magnetic field is the distance from the planet where a field line crosses the magnetic equatorial plane. This distance, measured in planetary radii from the center of the planet, gives an L value associated with the field line, and its associated L shell. Jupiter has a planetary radius (R_J) of 71 492 km. The orbit of the volcanic moon Io and its associated plasma torus is 5.9 R_J, Thus, the L shell of Io and the plasma torus generated along the orbit of Io by its active volcanoes is $L = 5.9$. The general consensus before the detection of H_3^+ was that it was particles precipitating from this torus that gave rise to the main auroral emissions from Jupiter (Sandel *et al.*, 1979).

In 1991, two teams used ProtoCAM to map the locations of the auroras. Kim *et al.* (1991) found that the morphology of the images they obtained was dependent on the exact noon meridian [or central meridian longitude (CML)] at which they were taken, reflecting the longitude dependency of the Jovian magnetic field; see Connerney, Acuna, and Ness (1981) and Fig. 4. This was demonstrated in greater detail by Baron *et al.* (1991). In their sequences of images, the northern aurora could clearly be seen rotating around the planet, and most clearly seen at CMLs from 128°W to 192°W. In the south, the brightest images were obtained with CMLs between 4°W and 119°W, clearly offset from the Northern Hemisphere.

Moreover, in both hemispheres, the brightest emissions formed an oval that mapped to higher latitudes and L values than those corresponding to the footprint of Io and its torus at $L = 5.9$; it was clear that the source of the brightest oval emissions was the middle magnetosphere, where L values were between 10 and 20. The fact that low L-shell ($L = 5.9$) derived particles were not the source of the main Jovian auroras was demonstrated conclusively by Connerney *et al.* (1993). They imaged Jupiter using a specially designed H_3^+ filter, centered on 3.4 μm and found the footprint of Io to be a bright spot separate from the main oval, as well as a trail that mapped to the torus. Further oval fitting (Kim *et al.*, 1994) showed that the main auroral oval closely followed the footprint of the high-L ($L = 15$ to 30) magnetic field shells. A paradigm shift that would harken back to earlier theoretical work by Hill (1979) was under way; it would be resolved nearly a decade later.

One key use of H_3^+ as a probe of changing planetary conditions came as a result of the impact of Comet Shoemaker-Levy 9 with Jupiter during the period of July 16–22 (UT), 1994; see the *Science* special issue collated by Lindley (1995) and its associated papers or Spencer and Mitton (1995) and the references therein for a summary of this event. The impacts occurred around latitude 43–44°S and gave rise to plumes of gas and dust that rose several thousand kilometers above the 1 bar surface of Jupiter before collapsing back down to create a series of dark impact scars (Hammel *et al.*, 1995; Orton *et al.*, 1995). Spectra taken on UKIRT at wavelengths sensitive to H_3^+ at the impact sites showed a plume of hot methane rising at velocities greater than the Jovian escape velocity (60 km s^{-1}), the first time an impact erosion of a planetary atmosphere had been observed (Dinelli, Achilleos *et al.*, 1995; Dinelli *et al.*, 1997). Other spectra showed that H_3^+ was depleted in the atmosphere at the impact sites (Encrenaz *et al.*, 1994).

The observations also showed that, while prior to the impacts, the northern aurora had been ~60% brighter than its southern counterpart, some five days after the final impact (July 27, 1994) the north was more than 5 times brighter than the southern aurora: the former had brightened considerably and the latter dimmed. Loss of H_3^+ in the southern auroral-polar regions had been predicted by Cravens (1994) as a result of it protonating comet-derived water. Because water ions recombine with electrons faster than H_3^+ does, this would result in peak electron densities being reduced by some 1 to 2 orders of magnitude for about a week after the impacts. Achilleos *et al.* (1995) and Miller *et al.* (1995) calculated that as a result of the lowered conductivity in the south auroral-polar regions the drag of Jupiter's magnetosphere would cause

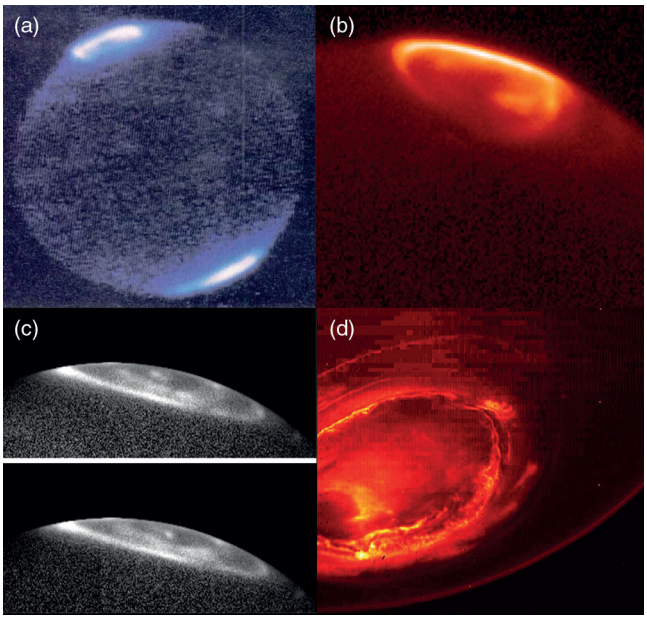

FIG. 4. Four images of Jupiter's H_3^+ aurora, showing the changes in resolution over the past 30 years. (a) One of the first detailed images of Jupiter's northern aurora, taken by ProtoCam on IRTF. From Baron *et al.*, 1991. (b) Jupiter's northern aurora taken by NSFCam on IRTF, using a specialist H_3^+ filter, as a part of the large catalog observed by Jack Connerney and Takehiko Satoh [archived at Stallard *et al.* (2018) and published in Rayner *et al.* (1993)]. (c) Two frames of Jupiter's northern aurora from the adaptive optics images taken by IRCS on Subaru, used to investigate short-term variability in Watanabe *et al.* (2018). (d) The first detailed image of Jupiter's southern aurora taken by the *Juno* JIRAM imager, as reported by Mura *et al.* (2017).

enhanced particle precipitation and Joule heating in the northern regions.

Together with Takehiko Satoh, Connerney went on to take several thousand H_3^+ images of Jupiter to fix the Io spot and other features [see Fig. 4; this dataset is archived at Stallard *et al.* (2018)], making use of ProtoCAM and its successor the National Science Foundation Camera)(Rayner *et al.*, 1993). This enabled them to develop a new magnetic field model for Jupiter (Connerney *et al.*, 1998), the VIP4 model, which made use of the *Voyager*, Io IR footprint, and *Pioneer* data (hence VIP) with a fourth (hence 4) order fit. The brightness of H_3^+ images during the 1992 *Ulysses* spacecraft encounter with Jupiter was used to infer that this correlated with the ram pressure on the Jovian magnetosphere generated by the solar wind. The images were also used to develop a model of the emissions themselves, with the researchers identifying the main auroral oval, together with a "collar" and polar-cap emission region, as the main components. But they had to be augmented by local-time variable emissions to get a good fit to the data.

Determining temperature $T(H_3^+)$ and column density $N(H_3^+)$ independently was not unproblematic. As a result Lam, Achilleos *et al.* (1997) defined a new term $E(H_3^+)$. This used $T(H_3^+)/N(H_3^+)$ pairs, together with a theoretical calculation of the emission per molecule, as a function of temperature (cooling curve) based on an *ab initio*, first-principles line lists (Kao *et al.*, 1991; Neale, Miller, and Tennyson, 1996), and the assumption that the vibrationally excited bands ($v_2 \geq 1$, etc.) were populated according to a quasithermal distribution (Miller, Joseph, and Tennyson, 1990).

Satoh and Connerney (1999a) developed the first phenomenological model to account for the detailed morphology of the auroral-polar regions. Poleward of the main auroral oval, their model had a yin-yang structure, with the midnight to midday sector darker than midday to midnight. Their analysis showed that nearly half (45%) of the overall auroral-polar emission from H_3^+ came from this polar region. Overall, the H_3^+ emission accounted for some 2.3×10^{12} W for the whole northern auroral-polar region and 1.3×10^{12} W for the south. They calculated that the particle precipitation required to produce this emission was 4.7×10^{12} W and 3.0×10^{12} W for the north and south, respectively, giving H_3^+ cooling efficiencies of ~47% of the energy deposited by particle precipitation for the planet as a whole (Satoh and Connerney, 1999a) (discussed later). This confirmed the conclusion of Miller, Lam, and Tennyson (1994) that H_3^+ was acting as an upper atmosphere thermostat: the H_3^+ thermostat effect. Further studies of images of the H_3^+ Io footprint and trail showed a series of emission spots downstream of the main footprint, probably due to Alfven waves reflecting between the Io plasma torus and the Jovian upper atmosphere.

Following these early H_3^+ images, made using ground-based telescopes, researchers began to take UV images of the atomic and molecular-hydrogen aurora using the Hubble Space Telescope. The first of these images, made using the Faint Object Camera (Macchetto, 1982) resulted in a reduced image quality when compared with what could be seen from Earth (Dols *et al.*, 1992). After the upgrade to the HST optics, however, (Clarke *et al.*, 1996) were able to detect the Io footprint in UV emission. With the introduction of the Hubble Space Telescope (HST) Wide Field and Planetary Camera 2 (WFPC2) (Griffiths, 1990), HST images began to supersede ground-based observations in terms of the degree of spatial detail that could be seen (Clarke, Ben Jaffel, and Gérard, 1998). The images showed UV emission from a structured auroral-polar region, including a narrow main oval with more diffuse emissions poleward. But Clarke *et al.* (1996) were not able to detect UV emission equatorward of the footprint of Io at the spectral resolution of WFPC2.

Soon thereafter, the HST Space Telescope Imaging Spectrograph (STIS) (Woodgate *et al.*, 1998) began to take images of Jupiter's aurora with an order-of-magnitude-higher sensitivity than earlier HST cameras and allowed the aurora to be imaged in unprecedented detail (Waite *et al.*, 2001). Using this, Grodent, Clarke, Kim *et al.* (2003) produced a statistical analysis of Jupiter's main auroral emission, detailing the "kink" in this emission between 110°W and 150°W in the northern aurora, with a new, more detailed reference model. This period also provided the first detailed measurements of the UV polar aurora, revealing three unique regions of morphology: the swirl, dark and active polar auroras (Grodent, Clarke, Waite *et al.*, 2003). The ionospheric auroral footprints of Europa and Ganymede were also observed and described for the first time (Clarke *et al.*, 2002). This use of STIS in providing unprecedented auroral details showed that the use of ground-based H_3^+ imaging in the investigation of gas giant auroras was limited, and subsequent ground-based studies have tended to focus on spectroscopic measurements of the IR auroras. For one exception to this, Barthelemy *et al.* (2011) used the UIST-IRPOL spectropolarimeter to image Jupiter's aurora in different polarizations. They were able to detect up to 7% polarization of the H_3^+ emissions of Jupiter's auroras, though no mechanism that can produce this polarization has currently been identified.

Beyond this and until the arrival of the *Juno* mission on July 4, 2016, most images of Jupiter's H_3^+ IR emission were therefore used in comparison with more detailed UV images to better understand differences between the auroras in these two wavelengths. The first direct comparison was made by Clarke *et al.* (2004), who investigated two near-simultaneous images taken of the northern UV and IR auroras. Comparison of deconvolved H_3^+ images revealed that the general auroral morphology was similar at both wavelengths. However, a later study by Radioti *et al.* (2013) reanalyzed the comparison using images from the same set of observations, taken approximately five minutes earlier. There Radioti *et al.* (2013) concluded that while the main emission morphology in the two wavelengths appeared to match well the polar aurora differed significantly. This apparent contrast in analysis was resolved by Stallard *et al.* (2016), who showed that the major differences seen between the two wavelengths were largely a result of the differing timescales of the respective auroras, as follows.

UV auroras are highly stochastic on timescales of 2–5 min since they result from prompt emission from atomic and molecular hydrogen. This coincides with the integration time for most HST observations in this period. However, when the

UV images were coadded into longer time steps, comparable to the modeled lifetime of H_3^+, $\tau(H_3^+)$, in Jupiter's polar aurora of ~10–15 min (Achilleos *et al.*, 1998), this stochastic emission resolved into clear arcs similar to those seen in the IR. The largest differences between the two wavelengths were the bright spots of emission seen on the dawn side in the UV, which could be the result of high-energy precipitation that lights up the atmosphere close to, or below, the homopause more brightly. In this boundary region, any H_3^+ generated is quickly destroyed by proton-exchange reactions with neutral hydrocarbons so that only more weakly emitting H_3^+ at higher altitudes remains. A dark region was also observed over Jupiter's northern magnetic pole, in a region that is typically bright in the UV. Observations of an auroral event in the UV and IR showed that significant eruptions from Io's Tvashtar volcano were enough to dramatically change Jupiter's auroral morphology, with the main emission expanding to engulf the Ganymede footprint, and significant localized enhancement equatorward of this, though the Io footprint itself disappeared for a day (Bonfond *et al.*, 2012).

The arrival of *Juno* at the planet refocused attention on H_3^+ studies, with observations taken by the spacecraft's Jovian Auroral Infrared Mapper (JIRAM) (Adriani *et al.*, 2017) providing the highest spatial-resolution images ever taken of the aurora. Mura *et al.* (2017) reported on the first *Juno* JIRAM images of the auroral zones of Jupiter. These provide images of the H_3^+ aurora that are not only at a spatial resolution better than any previous observations irrespective of wavelength, but at an order of magnitude higher than any past IR auroral image; see Fig. 4. They reveal the multiple arc morphology of the main ovals, with more arcs on the dusk side than have been observed in the UV in the past. Inside the polar region, there are regions of intense localized emissions that are, on average, brighter than those seen in the UV, in agreement with past ground-based observations ; see, e.g., Satoh and Connerney (1999b) and Stallard *et al.* (2001). Equatorward of the main aurora, the trail of emission behind the Io footprint was shown to last 3 h after the Io flux tube has passed, and locations of the Europa and Ganymede footprints were observed in the IR for the first time. The southern aurora is brighter than the northern aurora in these observations, with similar, probably conjugate, emission patterns observed in both polar regions.

Gérard *et al.* (2018) revealed both the complexity of Jupiter's aurora and the levels of detail that the H_3^+ emission could identify: Gérard *et al.* showed that JIRAM was measuring spatial resolutions as low as 50 km/pixel, compared with a resolution of ~750 km measured by *Juno*'s Ultraviolet Spectrograph (UVS). Gérard *et al.* (2018) also showed that large-scale auroral features were generally similar in the two wavelength regions, but they highlighted several important differences. The JIRAM images show persistent narrow arc structures in the region of the magnetic anomaly between 100°W and 180°W, not observed by UVS. The brightness across the auroral region is consistently much more variable in the UV than for H_3^+, as previously noted in ground-based observations [see, e.g., Radioti *et al.* (2013) and Stallard *et al.* (2016)], and the difference is strongest in regions where the UV emission is highly absorbed by stratospheric methane (and other hydrocarbons), where chemical reactions rapidly destroy H_3^+.

Mura *et al.* (2018) utilized this unprecedented spatial detail to reveal unexpectedly complex structure in and around the footprint of Io. The Io spot has previously been observed to consist of multiple spots (Gérard *et al.*, 2006), but JIRAM instead revealed a swirling pattern similar in appearance to a "von Kármán vortex street," a repeating pattern of swirling vortices shown in Fig. 5. The main spot was followed by a series of regularly spaced secondary spots, which alternated above and below the latitude that mapped magnetically to Io's orbit. Further downstream of the main footprint the extended tail appeared to consist of two separate parallel arcs of emission, extending for at least 70°, although this is not always present. This may be the result of a difference in the aurora in Io's own atmosphere, projected onto Jupiter. Ganymede's footprints also appeared as a pair of emission features, which may provide a remote measure of the moon's magnetosphere. These unexpected and unexplained features strongly suggest that the magnetohydrodynamic interactions between Jupiter and its moons are more complex than previously modeled.

Alongside these *Juno* JIRAM images, the use of adaptive optics (AO) has begun to allow observations from Earth to explore the aurora in detail. Watanabe *et al.* (2018) observed an hour-long sequence of images, each with an integration time of 45–110 s, revealing for the first time a periodic pulsation in the auroral arc separating the dark and swirl regions within the pole, an example of which is shown in Fig. 4. This feature could be produced by a modulated flux of precipitating electrons in the 1–10 keV range and provides an upper limit on τ (H_3^+) in this region of the aurora, 110 s. An estimate of the electron density can be obtained from the fact that $\tau(H_3^+) = (k_{DR}N_e)^{-1}$, where k_{DR} is the DR rate coefficient given in Sec. II.D and N_e is the local electron density. This leads to the result that N_e in this region is $\sim 8 \times 10^{10}$ m^{-3}.

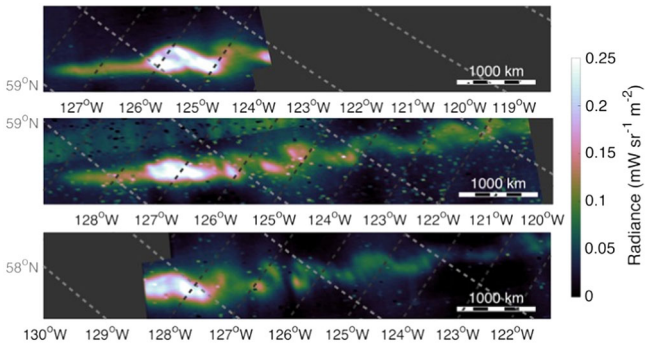

FIG. 5. High-resolution images of Io's auroral footprint in Jupiter's atmosphere. These polar orthographic projections of the radiance of the northern aurora are plotted with parallels and meridians. (Individual frames were supplied by A. Mura, deputy principal investigator of the JIRAM instrument on *Juno*.) These showed that rather than a sequence of auroral "spots," the footprint was instead formed from a swirling pattern, which Mura *et al.* (2018) compared with a von Kármán vortex street. The individual black and white pixels are the effect of penetrating radiation from Jupiter's magnetosphere affecting the detector.

2. Auroral temperatures

In their study using the fundamental ν_2 band, Maillard *et al.* (1990) determined the rotational temperature (T_{rot}) in the northern auroral region to be 1000 ($\pm$40) K in the northern auroral region and 835 ($\pm$50) K in the south, with the northern emission being roughly twice as intense as that in the south. They failed to detect the overtone spectrum on this occasion. Oka and Geballe (1990) carried out a study of a limited wavelength region around the $J = 5$ branch of the ν_2 spectrum and obtained a temperature of 670 ($\pm$100) K, and a population of 10^{14}–10^{15} m^{-2} on the $v_2 = 1$ level. Together these results clearly showed the spatial and temporal variability of the auroral atmosphere of Jupiter.

Detection of two vibrational bands in a near-simultaneous fashion enabled one of the conundrums raised concerning the way in which the H_3^+ vibrational bands were populated. Miller, Joseph, and Tennyson (1990) showed that the rovibrational temperature T_{rv} derived by taking the ratio of lines in the overtone band with those in the fundamental band was ~1100 K, which is close to the rotational temperature found by fitting lines within each of the individual bands. Since such spectroscopy could not give information about the population of the H_3^+ ground vibrational state, this result was interpreted as showing that the vibrational levels of H_3^+ were populated in accordance with a *quasithermal distribution*.

There is no vibrational correspondence between H_2 and the $v_2 = 1$ level of H_3^+ so that level cannot be populated in the upper atmosphere of Jupiter by resonant energy exchange. Thus, the Miller, Joseph, and Tennyson (1990) result meant that the population of the $v_2 = 2$ level by resonant energy exchange with H_2 was also unlikely: H_3^+ emissions were essentially thermalized, reflecting the ambient temperatures in the upper atmosphere. This was also the conclusion of Maillard *et al.* (1990) and was further borne out by analysis of the H_2 quadrupole emission of Jupiter (Kim *et al.*, 1990), which gave a temperature of 730 ($+450/-200$) K for Jupiter's southern auroral zone temperature, coinciding well with the 670 ($\pm$100) K value cited previously for the H_3^+ rotational temperature in the southern auroral zone.

Line resolved spectra by Drossart *et al.* (1993) gave $T_{rot} =$ 1250 ($\pm$70) K and the translational temperature $T_{trans} =$ 1150 ($\pm$50) K , making them in close agreement with one another, again suggesting that H_3^+ emission was from a (quasi) thermal population of the ions. The thermalized nature of the H_3^+ emissions was a useful contrast to the UV emissions that are due to prompt (pump-and-dump) processes. H_3^+ was therefore established as a useful indicator of temperature changes in Jupiter's upper atmosphere. Despite this, however, some models continued to predict that the H_3^+ $v_2 = 2$ level should be overpopulated by resonant energy exchange with H_2, $v = 1$ (Kim, Fox, and Porter, 1992).

Kim, Fox, and Porter (1992) also predicted, however, that all vibrationally excited levels would be underpopulated compared to a true local thermodynamic equilibrium (LTE) distribution since the large H_3^+ A_{if} values made depopulation of excited levels by spontaneous emission comparable to that due to collisional deexcitation at the relatively low neutral (H_2) densities ($< 10^{18}$ m^{-3}) that prevail in the lower thermosphere. This result indicated that all column densities derived directly from H_3^+ line strengths would be lower estimates, and highlighted the need for more sophisticated detailed-balance calculations and accurate model vertical profiles of the ion's distribution in Jupiter's upper atmosphere (discussed later).

Giles *et al.* (2016) provided a new comparison of kinetic, rotational, and vibrational temperature by accessing *P*-branch emission lines in the 5 μm window. Using the high-resolution Cryogenic Infrared Echelle Spectrograph (CRIRES) (Kaeufl *et al.*, 2004) with a spectral resolution of $\lambda/\Delta\lambda \sim 100\,000$ on European Southern Observatory (ESO)'s Very Large Telescope (VLT), Giles *et al.* were able to measure linewidths, producing a kinetic temperature of $T_{kin} = 1390$ K. They compared this temperature with line ratios of ν_2 fundamental emission and $2\nu_2(2) - \nu_2$ hot band emission to produce a rotational temperature of $T_{rot} = 960$ K and a rovibrational temperature of $T_{vib} = 925$ K. This suggests that while quasithermal equilibrium might hold, temperatures measured using line ratios provide results significantly lower than the true translational temperatures.

In preparation for the arrival of the *Juno* spacecraft at Jupiter, Altieri *et al.* (2016) reanalyzed observations made by the *Galileo* Near-Infrared Mapping Spectrometer (Aptaker, 1987) instrument of H_3^+ from Jupiter's north pole. They found H_3^+ temperatures between 500 and 635 K and column densities of 1.7×10^{16} m^{-2} to 32.2×10^{16} m^{-2}, suggesting temperatures significantly lower than those measured by other methods. Now in orbit around Jupiter, *Juno* has triggered a series of new observations of H_3^+ temperatures, both from the spacecraft itself and from supporting ground-based telescopes. Kedziora-Chudczer *et al.* (2017) utilized the Gemini Near-Infrared Spectrograph (Elias *et al.*, 1998) for H_3^+ observations at 2 μm to measure the $2\nu_2$ overtone band, deriving $T(H_3^+) =$ 950 K and $N(H_3^+) = 4.5 \times 10^{16}$ m^{-2}.

Moore *et al.* (2017) aligned Keck's near-IR echelle spectrograph (NIRSPEC) (McLean *et al.*, 1998) slit with Jupiter's noon (central) meridian so that the planet rotated through the slit, allowing them to map out the H_3^+ temperature as the auroral region rotated past; see Fig. 6. Although this observation technique could not follow short-term auroral changes, it resulted in high-precision maps of H_3^+ temperatures, densities, and radiances across Jupiter's northern and southern auroral regions over 4 d in April 2016. A solar-wind event that impacted Jupiter just before the first of these nights of observations (April 14) was thought to have produced a slowly cooling ionosphere, followed by a period of enhanced H_3^+ brightness and density on April 23. Since no solar-wind changes were observed during this period, it was suggested that this enhancement was the result of changes in the interior of Jupiter's magnetic field.

During the first orbit of the *Juno* mission around Jupiter, the JIRAM instrument made a large number of measurements of both of Jupiter's auroral regions. These spectral images allowed a measurement of brightness across the 2–5 μm wavelength range at unprecedented spatial resolution. Emission from both ionospheric H_3^+ and stratospheric fluorescent CH_4 can be extracted from these images, resulting in maps of the H_3^+ brightness across a range of emission lines in

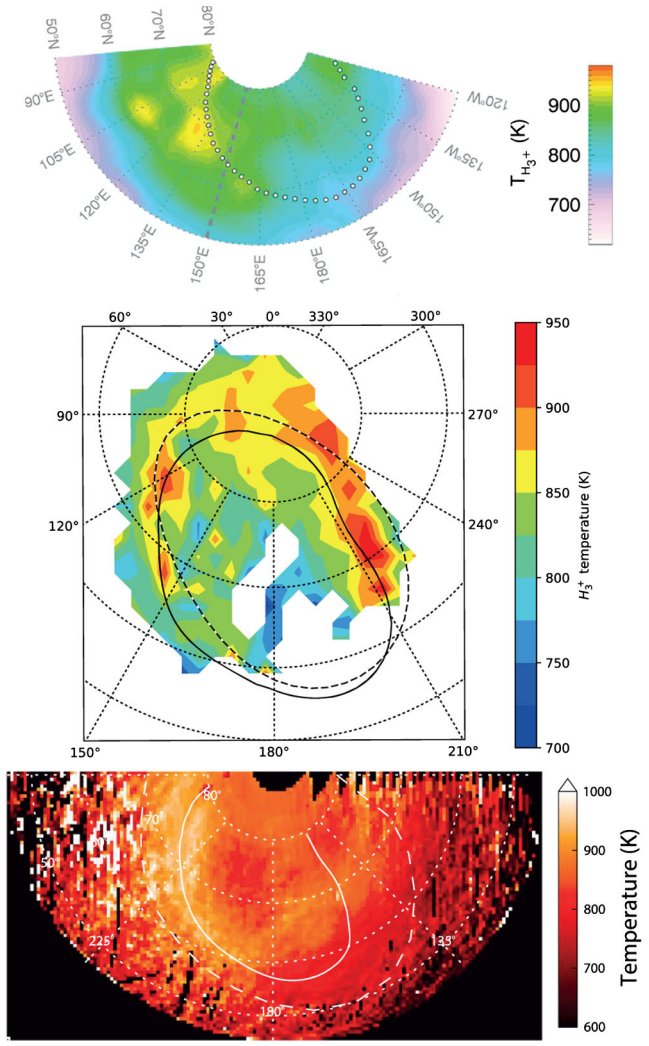

FIG. 6. Three maps of Jupiter's northern auroral H_3^+ temperature. (Top panel) The scanned spectral map of the aurora taken by the Keck NIRSPEC instrument, with the slit aligned north and south and the planet rotating through the slit, with high spectral resolution and high sensitivity ($\lambda/\Delta\lambda \sim 25\,000$ using a 10 m telescope), with the white dots marking the location of the main auroral oval from the VIP4 model (Connerney *et al.*, 1998). Adapted from Moore *et al.*, 2017. (Middle panel) Map produced by *Juno* JIRAM spectral scans of the aurora from the PJ-1 orbit, with low spectral resolution ($\lambda/\Delta\lambda \sim 200$) and high spatial resolution, in which the dashed line represents the location of the auroral oval from the VIP4 model (Connerney *et al.*, 1998) and the solid line is the statistical location of the aurora calculated by Bonfond *et al.* (2012). Adapted from Dinelli *et al.*, 2017. (Bottom panel) Scanned map of the aurora taken by the VLT CRIRES instrument, with a high spectral resolution and high sensitivity ($\lambda/\Delta\lambda \sim 100\,000$ and an 8 m telescope), with the solid line demarking the peak H_3^+ auroral intensity along the main auroral emission, as measured by Johnson *et al.* (2017), and the dashed line showing the location of the magnetic footprint of Io according to the Grodent *et al.* (2008) model. From Johnson *et al.*, 2018.

both the northern (Dinelli *et al.*, 2017) (see Fig. 6) and southern (Adriani, Mura *et al.*, 2017) auroral regions. Although their spatial resolution was lower than the near-simultaneous L-band images of the aurora, these maps provided a detailed measure of both H_3^+ temperature and column density. The column density varied between 0.2×10^{16} m^{-2} and 4.0×10^{16} m^{-2}, with the highest densities following the auroral location predicted by the VIP4 model (Connerney *et al.*, 1998). Retrieved temperatures were between 600 and 1400 K, without a strong correlation to auroral location, with a prevalence of higher values near dawn and with $T(H_3^+)$ varying on a larger spatial scale than changes in $N(H_3^+)$.

Johnson *et al.* (2018) analyzed observations of Jupiter's northern aurora using the VLT CRIRES instrument, providing a comparable measure of the H_3^+ temperature (see Fig. 6) and column density. While observing from Earth, this provided a spatial scale slightly lower than that measured from *Juno*, but lower errors in measured values, a result of the high spectral resolution ($\lambda/\Delta\lambda \sim 100\,000$) of the CRIRES echelle spectrometer. Here the column density varied in the range $(1–6) \times 10^{16}$ m^{-2} and the temperature between 800 and 1000 K. Again, the morphology of the column density closely followed past magnetic models and previous UV images, with narrow emission in the dawn and a more defuse aurora at dusk. The temperatures varied over a wider spatial scale, with the highest temperatures again observed near the dawn side main oval, with a finger of significant heating over the pole. Johnson *et al.* also identified significant changes in the local temperatures as the planet rotated, caused by either a change in the altitude of peak H_3^+ emission due to variations in the precipitating electron energy or through the propagation of a thermospheric wave across the aurora following changes in energy inputs, as predicted by Yates, Achilleos, and Guio (2014).

3. Measurements on the planetary disk

In the 1990s, the CGS4 long-slit, cooled grating spectrometer (Mountain *et al.*, 1990) made it possible to build up spectral images of the distribution of H_3^+ emission from Jupiter, making it possible to determine the emission at mid-to-low latitudes (Ballester *et al.*, 1994). Setting the slit along the CML and allowing the planet to rotate under it meant that over several nights of continuous observation latitude-longitude maps of the noon emission parameters could be obtained (Lam, Achilleos *et al.*, 1997; Miller *et al.*, 1997). These showed high temperature [$T(H_3^+) = 800$ to >950 K], high-column-density [$N(H_3^+) = \sim 1 \times 10^{16}$ m^2] emission in the auroral-polar regions, indicating that the brightness seen there in the images and in individual spectra was a combination of the two factors.

At latitudes outside of the auroral-polar regions [mid-to-low latitudes (MTLs)] there was a fairly monotonic falloff in $N(H_3^+)$ to less than 10^{15} m^{-2} in the equatorial regions, in accord with other results from the CFHT (Marten *et al.*, 1994). Temperatures fell to ~700 K at the midlatitudes, although closer to the equator there was a belt where $T(H_3^+)$ rose back up to ~800 to ~900 K; this was not quite as high as had been reported earlier by Ballester *et al.* (1994), whose high equatorial temperatures ~1200 K were shown to be due to problems subtracting the background emission of Jupiter from the weak low-latitude H_3^+ emission.

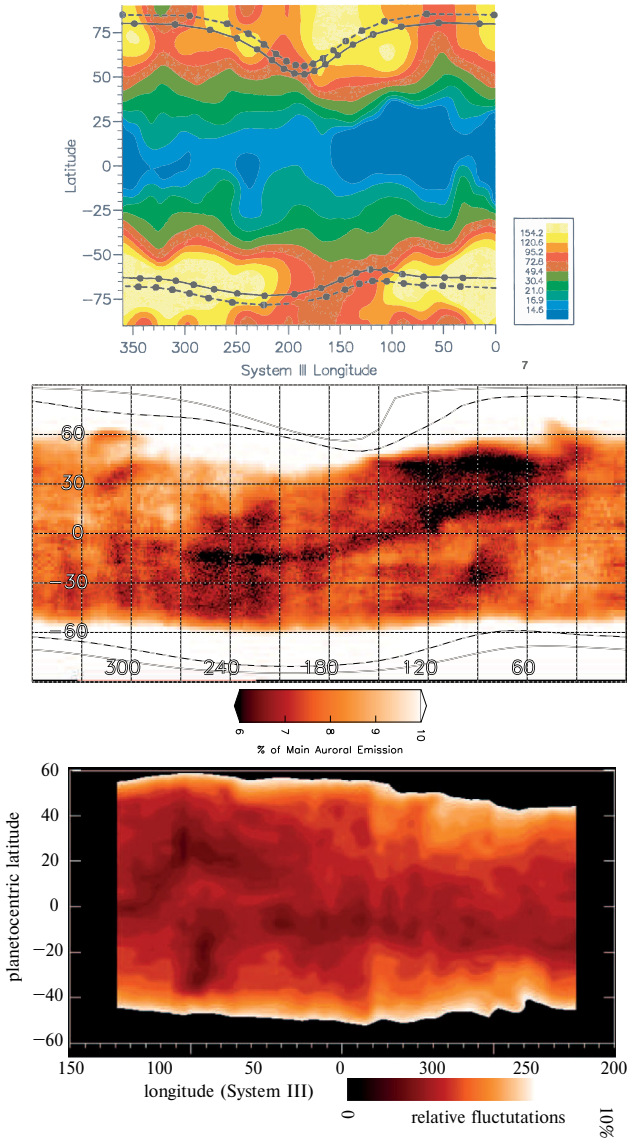

FIG. 7. Three maps of Jupiter's mid-to-low-latitude H_3^+ emission. (Top panel) Map of the H_3^+ total emission parameter derived from fitted temperature and column densities,)with units of μW m^{-2} sr^{-1}. From Lam, Achilleos *et al.*, 1997. (Middle panel) A relative brightness map, produced by combining tens of thousands of H_3^+ images taken of Jupiter between 1995 and 2000 that were then corrected to remove reflected sunlight and scaled to between 6% and 10% of the peak auroral brightness. From Stallard *et al.*, 2018. (Bottom panel) Map of H_3^+ radiance fluctuation that combines multiple H_3^+ emission lines over two nights, using moderate resolution spectra ($\lambda/\Delta\lambda \sim 30\,000$) taken by VLT ISSAC; note that this map has an offset zero in the longitude axis. From Drossart, 2019.

The emission map derived from Lam, Achilleos *et al.* (1997) (Fig. 7) showed that $E(H_3^+)$ correlated to regions on the planet where the locus of the L-shell footprint encountered a falling magnetic field strength. This was interpreted as resulting from westward drifting electrons (drifting counter to the planet's own rotation) precipitating preferentially as the magnetic field strength diminished and, in turn, ionizing the atmosphere and producing greater $T(H_3^+)$ and $N(H_3^+)$ values (Miller *et al.*, 1997). The emission map also indicated that H_3^+ was having a marked cooling effect on Jupiter's upper atmosphere, with emission of > 100 μW m^{-2} sr^{-1} in the auroral-polar regions. Even at lower latitudes, emissions were >10 μW m^{-2} sr^{-1}. Thus, the ion was behaving as an upper atmosphere thermostat (Miller, Lam, and Tennyson, 1994) across the planetary disk at lower latitudes as well as in the auroral region (Miller *et al.*, 1997). The relatively high levels of H_3^+ emission also indicated that the ion was either transported on equatorward winds from the main auroral regions or somehow produced *in situ*. The former explanation seems unlikely given the probable velocity of equatorward winds and the relatively short H_3^+ lifetimes [$100 \leq \tau(H_3^+) \leq 1000$ s] (Tao *et al.*, 2014) that would prevail in Jupiter before recombination with electrons occurred; the latter was considered to indicate that some particle precipitation might be occurring, similar to that considered necessary to produce x-ray emission (Waite *et al.*, 1997), although explaining it proved difficult (Abel and Thorne, 2003).

Low-latitude emission from Jupiter was studied by Satoh and Connerney (1999b) using their large collection of images taken on the NASA IRTF. They found that they could treat this with a model that had an optically thin layer of H_3^+ at around 750 km above the cloud tops (0.6 bar level) where the *Galileo* probe had found temperatures of 770 to 840 K, in close agreement with those measured from the ground (Lam, Achilleos *et al.*, 1997; Miller *et al.*, 1997).

The planetwide emission of Jupiter was studied in further detail by Rego *et al.* (2000). Their analysis indicated the overall pole-to-pole emission profiles could initially be broken down into three components:

(1) Emission from the main auroral oval.
(2) Diffuse emission poleward of the main oval.
(3) Solar extreme ultraviolet (EUV) produced emission across the entire disk of the planet.

There were also some profiles that showed emission from the Io footprint and its trail.

Assuming that all of the emission at the magnetic equator was the result of solar EUV ionization, the magnitude of this component could then be modeled at all latitudes. This modeling, however, demonstrated that insolation could not be responsible for all of the emission seen at subauroral–sub-Io-footprint latitudes. Instead, to fit the data, Rego *et al.* (2000) had to invoke a MTL component whose production mechanism was not clear. Further work by Morioka *et al.* (2004) showed that the area of Jupiter's disk covered by MTL-subauroral H_3^+ emission was correlated to a time-varying auroral activity index. This study also confirmed the deductions of previous studies (Lam, Achilleos *et al.*, 1997; Miller *et al.*, 1997) that H_3^+ was a major atmospheric coolant at all latitudes for Jupiter.

For an extended period, these early observations of the equatorial emission remained the only spectral observations of this region, partly due to the limited sensitivity of instrumentation at the time. There were, however, some early indications that this region might be more complex than these early observations suggested. Barrow, Matcheva, and Drossart (2012) suggested that the H_3^+ concentration in the Jovian upper atmosphere responds to the arrival of gravity waves,

driven by fluctuations as small as 0.2% and that high-resolution spectroscopy could detect these waves.

A lower limit to the amount of equatorial particle precipitation was revealed through observations by Kita *et al.* (2015), who combined observations of the Giant Metrewave Radio Telescope and NASA Infrared Telescope Facility in November 2011. This showed up to 10% enhancements in H_3^+ emission over a period of ∼10 Jovian days, directly correlated with the increased solar UV and EUV flux, but, in addition, also showed evidence of processes such as wave-particle interaction.

This supported the prediction by Brice and Mcdonough (1973) that heating of the Jovian thermosphere by solar UV and EUV radiation would drive a planetary atmospheric neutral wind, inducing a dynamo electric field in the Jovian thermosphere. This electric field, mapped onto the radiation belt, would then cause inward radial diffusion of energetic particles, causing the total flux density of Jupiter's synchrotron radiation (and thus H_3^+ ionization) to correlate with solar UV and EUV flux. This modeling work was expanded upon by Tao *et al.* (2014), who predicted that a 100% increase in EUV flux would result in a 16% increase in the thermospheric neutral wind velocity at ∼45° latitude. But the estimated variation in the effective velocity (a few $m\,s^{-1}$) was smaller by an order of magnitude than what was needed to produce the observed synchrotron radio emission enhancements from energetic particles in the magnetosphere (Tao *et al.*, 2014).

An upper limit to equatorial particle precipitation came from observations of Jupiter's nightside ionosphere from the *Cassini* flyby in 2000, where Stallard *et al.* (2015) were able to show that the subauroral enhancement in H_3^+ emission was not observed. They showed that this enhancement was due to thermal heating of a mostly EUV-ionized ionosphere on the dayside, with a maximum contribution of 10% from particle precipitation across the entire subauroral and equatorial region.

However, the neutral upper atmosphere has long been shown to vary in brightness with latitude, with a UV Lyman-α excess along the equatorial regions known as the Lyman-α bulge (Clarke *et al.*, 1980; Sandel, Broadfoot, and Strobel, 1980). This bulge had previously been described as resulting from a supersonic jet flowing from the two poles, colliding at the equator (Sommeria, Jaffel, and Prangé, 1995). Nonetheless, when Johnson *et al.* (2016) investigated the H_3^+ ion winds close to the equator, they found no evidence of any significant subrotation in this region, with the equator corotating (within errors of ∼100 $m\,s^{-1}$). Melin and Stallard (2016), who provided the most detailed map of this Lyman-α bulge using the *Cassini* Ultraviolet Imaging Spectrograph (UVIS) subsystem observations, showed clear evidence that the bulge varied in latitudinal position with the magnetic field equator and suggested that the bulge could be produced as a result of H_3^+ electron recombination driving up H densities and thus emission. These observations suggested a $\tau(H_3^+)$ lifetime of $1.6(\pm 0.4)$ h and electron density of 1.7×10^9 m^{-3}.

More recently it was shown that H_3^+ emission in this region is also strongly influenced by changes in thermospheric temperature, which in turn is effected by interactions with both the magnetosphere and the lower atmosphere. O'Donoghue, Moore *et al.* (2016) discovered a highly localized region of strong heating of H_3^+ directly above Jupiter's Great Red Spot. This heating produced a temperature of ∼1600 K, at least 500 K hotter than the surrounding equatorial regions. This provided the first direct observational evidence of energy transference from the lower atmosphere to the thermosphere.

Previous modeling studies like that of Barrow, Matcheva, and Drossart (2012) could not explain such large temperature changes. O'Donoghue, Moore *et al.* proposed that this heating is driven by acoustic waves propagating vertically upward from the turbulent regions of the Great Red Spot and breaking within the upper atmosphere. Ray *et al.* (2019) confirmed this detection and predicted that a second hot spot would appear at the magnetically conjugate position in the Northern Hemisphere; they attributed both of the hot spots to Joule heating.

Stallard *et al.* (2017) showed that localized regions of cooling can also exist within Jupiter's thermosphere: a "Great Cold Spot". This spot was characterized by H_3^+ temperatures of around 600 K, some 200 K lower than the surrounding thermospheric H_3^+ temperatures. The spot was confined over long timescales (∼320 yr) to an approximate System III position, centered on 55°N and ∼300°W. But it was observed to drift back and forth between 270° and 330° System III longitude over a period of only a few Earth months. The spot's size and morphology were both highly variable, and Stallard *et al.* speculated that it may be caused by a localized vortex within the thermosphere that ebbs and wanes but is regenerated in a similar location over time as a result of the energy flowing through the thermosphere from the auroral region.

Stallard *et al.* (2018) used an extensive reanalysis of the IRTF NSFCAM images taken by Connerney and Satoh in support of the *Galileo* mission to provide a new map of H_3^+ brightness. This map, shown in Fig. 7, was averaged over more than 40 nights taken at various times over a period of several years, providing a view of the ionosphere independent of both the underlying lower atmospheric weather (which is smoothed over several years) and local time. This revealed significant variations in the equatorial H_3^+ brightness at all longitudes and latitudes, including the detection of Jupiter's magnetic equator as a dark ribbon circling the planet. Measurements of the magnetic equator by the *Juno* magnetometer (Connerney *et al.*, 2018) have now confirmed this feature, as well as a dark spot at 25°S and 80°W, which appears to be approximately coincident with an intense spot of negative radial magnetic flux in the Southern Hemisphere, at a longitude of around 90°W (K. M. Moore *et al.*, 2018). These ionospheric darkenings were confirmed by Drossart (2019), as shown in Fig. 7.

The H_3^+ emission in Jupiter's equatorial atmosphere was observed above the limb with *Juno* JIRAM, from 60°N to 60°S, allowing the vertical distribution of H_3^+ emissions to be characterized as a function of latitude across Jupiter's dayside (Migliorini *et al.*, 2019). The H_3^+ density was distributed approximately symmetrically with latitude, decreasing from 5×10^{10} m^{-3} at 300 km to 2×10^9 m^{-3} at 650 km altitude above the 1 bar level. This equates to column densities of

3.5×10^{16} to 1.4×10^{15} m^{-2}. The H_3^+ volumetric mixing ratio was higher in the Southern Hemisphere [8×10^{-4} parts per million volumetric (ppmv) at 500 km altitude at 40°S] than in the Northern Hemisphere (4×10^{-4} ppmv at the same altitude at 40°N). Migliorini *et al.* (2019) also provided retrieved temperatures with increasing altitude, showing a close-to-monotonic increase from ~400 K at 300 km to >900 K at 700 km.

One of the remaining issues that no modeling or observational study has been able to clarify so far is just why there is so much H_3^+ to be found on the planetary disk, equatorward of the main auroral regions, as detected by Lam, Achilleos *et al.* (1997) and Miller *et al.* (1997). The rapid DR that H_3^+ undergoes with electrons, discussed in Sec. II.D, led Miller *et al.* (1997) to conclude that the lifetime of the ion was of the order of 100 to 1000 s, not long enough for it to be transported equatorward on the relatively slow winds of a few tens of $m\,s^{-1}$. Rego *et al.* (2000) demonstrated that solar EUV ionization could not produce enough H_3^+ at midlatitudes even if one made the generous assumption that it was enough to produce all of the observed ions at the equator. And Abel and Thorne (2003) found that they could reproduce the *pattern* of H_3^+ observed by considering particle precipitation from Jupiter's radiation belts, but not the *quantity*.

4. The auroral curtain and altitude profiles

In early observations the variation in H_3^+ emission focused upon changes with latitude and longitude. As instrumentation became more sensitive, observations began to focus more closely upon the changes with altitude that would enable comparisons with modeled vertical atmospheric profiles to be made. Detailed modeling of the vertical profile of the atmosphere of Jupiter both in one dimension [see, e.g., Atreya, Donahue, and McElroy (1974)], since the time of the *Pioneer* and *Voyager* missions, and, later, in three dimensions [e.g., the Jovian ionospheric model (JIM)] (Achilleos *et al.*, 1998) made it possible to investigate the chemical composition of the Jovian upper atmosphere as a function of altitude for a variety inputs, and to compute the overall consequences of this. In these models, various fluxes of keV-energy electrons were allowed to precipitate at the top of the atmosphere, from where their energy would be degraded by collisions that caused ionization, chemical reactions, and atmospheric heating. In the JIM (Achilleos *et al.*, 1998), for example, fluxes of a few milliwatts per m^{-2} of 60 keV electrons produced a pronounced H_3^+ local density peak of 10^{12} m^{-3} just above the 1 μbar homopause.

Grodent, Waite, and Gérard (2001) published a self-consistent, one-dimensional profile that made use of the measurements from the *Galileo* probe (Seiff *et al.*, 1997) and then added in auroral electron precipitation and scaled the results to match the auroral temperatures found by Lam, Achilleos *et al.* (1997). This model required a three component electron flux, with energies centered on 100 eV, to heat the top of the atmosphere, and 3 and 22 keV to create the measured H_3^+ densities. At the lower densities prevailing higher in the Jovian atmosphere, populations of vibrationally excited H_3^+ ions were thought to fall below those expected from full LTE. Melin *et al.* (2005) then used this profile, together with a non-LTE calculation of the emission from various rovibrational states of H_3^+, to calculate the emission as a function of altitude. Integrated through the entire vertical column of the atmosphere, the modeled emission in the $Q(1,0^-)$ line at 3.953 μm allowing for non-LTE effects was reduced to 72% of that calculated assuming that full LTE prevailed; for the $2\nu_2R(6,6^+)$ line at 2.903 μm, however, the value could be as low as 4% of the LTE-expected value. This result had important consequences for understanding H_3^+ emission rates and temperatures, particularly at higher altitudes where gas densities were low.

Using off-limb spectra in the Jovian auroral regions, Lystrup *et al.* (2008) were able to measure the H_3^+ emission across the southern auroral-polar region using the NIRSPEC long-slit spectrometer on the Keck II telescope. As the slit sampled regions "off" the dusk auroral oval it effectively took a vertical profile of the H_3^+ above the aurora. There $T(H_3^+)$ rose monotonically to ~1400 K, while $N(H_3^+)$, derived by using an "onion skin" approximation to the emissions, fell off until it could no longer be determined. The density vertical profile spanned values from 2×10^{11} m^{-3} at the peak emission (~700 km above the nominal reference zero of the Jovian cloud tops) to 3×10^7 m^{-3} at the highest altitude they could effectively sample: 3900 km. Given the work of Melin *et al.* (2005), Lystrup *et al.* (2008) needed to account for non-LTE effects by rescaling the Grodent, Waite, and Gérard (2001) density profile. Normalized to the respective peak density values, these profiles matched, giving one confidence that the Grodent, Waite, and Gérard (2001) profile, suitably scaled, could be used to model $T(H_3^+)$ and $N(H_3^+)$ when measured vertical profiles are not available.

The measurements of Lystrup *et al.* (2008) were also able to determine temperatures and column densities west-to-east across the planet in the auroral-polar regions themselves. Poleward (inside) of the main auroral oval, they found $T(H_3^+)$ in excess of 1300 K and $N(H_3^+)$ around 0.6×10^{16} m^{-2}, with anticorrelated oscillations that provided some evidence of wave activity. Over the oval itself, the temperature dropped to ~1050 K with $N(H_3^+) \sim 4 \times 10^{16}$ m^{-2}, evidence of the aurora being produced by high-energy (tens of keV) electrons precipitating deep into the thermosphere toward the 1 μbar homopause, as anticipated by the models.

Tao, Badman, and Fujimoto (2011) provided a direct measure of the expected changes in both IR and UV emission from Jupiter and Saturn due to precipitation-induced ionization. Emission rates for both wavelengths increased with increasing individual electron energy, but while UV emission was directly proportional to flux, the H_3^+ emission was modeled as proportional to the square root of flux and more strongly affected by changing temperature. This model predicted that for both planets the main H_3^+ emission peak would be quasithermalized so that most emission from these planets would provide a reasonable measure of the underlying thermospheric temperature. Following from the work of Tao, Badman, and Fujimoto (2011), more detailed analysis (Tao *et al.*, 2012) of the changes in individual H_3^+ line brightness with particle precipitation energy showed that careful analysis of individual H_3^+ emission lines in the 2 and 3–4 μm regions at

Jupiter could be used to estimate the energy of precipitating electrons. However, Kim (2012) remodeled the non-LTE effects; in contrast to Tao, Badman, and Fujimoto (2011), their model showed that significant non-LTE effects appeared near and above the H_3^+ peak, and that the kinetic temperatures in the Jovian thermospheric temperatures derived from the observed line ratios in the 2 and 3.5 μm H_3^+ emissions were highly model dependent.

AO made it possible for Uno *et al.* (2014) to measure H_3^+ emission above Jupiter's limb at a spatial resolution of ~165 km/pixel. These researchers looked at the 2 μm spectra using the Subaru Infrared Camera and Spectrograph (IRCS) (Kobayashi *et al.*, 2000) and produced H_3^+ vertical profiles for the overtone and hot overtone bands at Jupiter simultaneously with H_2 emission profiles. The overtone H_3^+ appeared to peak at ~750 km in the polar region and ~500 km near the edge of the auroral oval. This suggests that this emission occurs at similar, though not identical, altitudes to the H_2 IR quadrupole emission, which was observed at 720 km for polar H_2 and 600 km for H_2 emission at the edge of oval. Using the model of Tao *et al.* (2012), it was shown that the H_3^+ emission could be modeled as resulting from a blend of precipitating electrons consisting of 0.1 and 3 keV.

This study was followed up with further IRCS AO-corrected observations by Kita *et al.* (2018), who repeated the observation of 2 μm emission from Jupiter but also observed fundamental H_3^+ emission at 4 μm. In doing so, they were able to measure the peak emission altitudes for H_3^+ fundamental, H_3^+ overtone, and H_2 quadrupole lines. These were calculated at 650, 870, and 830 km, respectively, in the north and 700, 910, and 950 km, respectively, in the south. This result showed for the first time that the fundamental H_3^+ emission peak at Jupiter sits some 200 km deeper in the atmosphere than the layer in which the overtone H_3^+ emission and H_2 quadrupole emission both peak.

Further detailed modeling of particle precipitation into Jupiter's atmosphere led Egert, Waite, and Bell (2017) to propose that Jupiter H_2 emission comes from electron impacts > 10 keV, while H_3^+ is due to impacts of electrons < 10 keV, in contrast with past models that used precipitating particles of tens of keVs. Recently analysis of measurements of the auroral curtain by *Juno* JIRAM showed a peak density of H_3^+ at an altitude > 750 km (Dinelli *et al.*, 2019).

Moore *et al.* (2019) explored the effects of the changing H_3^+ temperature and density along the line of sight for a typical observation, finding that H_3^+ column densities retrieved from such observations are found to represent a lower limit, reduced by 20% or more from the true atmospheric value. A preliminary method of deriving vertical temperature structure using such observations was also demonstrated at Jupiter using model reproductions of electron density and H_3^+ measurements, suggesting that this tool might allow the temperature structure of Jupiter's ionosphere to be understood in three dimensions in the future.

5. Auroral ion winds

Earlier modeling studies [see, e.g., Atreya and Donahue (1975), Waite *et al.* (1983), Majeed and McConnell (1991), Kim, Fox, and Porter (1992), and Cravens (1994)] used one-dimensional profiles to probe the importance of H_3^+ in determining the chemistry and electrical properties of giant planet atmospheres, showing how varying key parameters, such as the rate coefficient of H_3^+ DR with electrons (Majeed and McConnell, 1991) and the resonant population of H_3^+ ($v_2 = 2$) by H_2 ($v = 1$), could affect these properties. Three-dimensional, time-dependent modeling showed the importance of H_3^+ in determining the dynamics of planetary upper atmospheres. The JIM (Achilleos *et al.*, 1998) demonstrated that neutral winds of > 100 m s^{-1} would be produced as a result of pressure gradients and could form the basis of modeling other dynamic effects. In particular, the JIM showed the importance of ion drag effects in determining the neutral wind systems.

Using the IRTF Cryogenic Echelle Spectrograph (CSHELL) (Greene *et al.*, 1993) at $\lambda/\Delta\lambda \sim 30\,000$, Rego *et al.* (1999) showed for the first time that H_3^+ was moving at high velocities in the planetary frame of reference. Following this up and scanning the spectrometer slit equatorward from the pole, a complicated wind pattern could be discerned: there was a westward flowing auroral jet of H_3^+ ions nearly coincident with the main oval, known as the electrojet (Stallard *et al.*, 2001). Stallard *et al.* identified a rising auroral oval (RAO) in the dawn sector, followed in order by a dark polar region (DPR), a bright polar region (BPR), and a setting auroral oval (SAO).

Typically, the electrojet flowed westward at ~1.2–1.5 km s^{-1}, about half the sound speed in Jupiter's upper atmosphere. In the planetary reference frame, the DPR was strongly redshifted and the BPR slightly blueshifted; an inner region of the DPR appeared to be static in the inertial frame of reference, indicating a region around the magnetic pole that was connected to field lines that went far out into the planet's magnetotail (Cowley *et al.*, 2003; Stallard *et al.*, 2003). This flow could be modeled by the lag to corotation of the middle magnetosphere bending magnetic field lines that connected to the auroral ionosphere, creating an equatorward electric field $\mathbf{V}_E$ of magnitude V_E across the auroral oval. In this region, Jupiter's magnetic field $\mathbf{B}_J$ is almost vertical, with a magnitude B_J of ~10^{-3} T. This then produced a Hall drift of the ions given by

$$v_{\text{ion}} = -\left(\frac{\mathbf{B}_J \times \mathbf{V}_E}{B_J^2}\right), \tag{3}$$

where v_{ion} is the velocity of the ions in the auroral electroject in the planetary frame of reference and the minus sign indicates the flow is westward. Equation (3) leads to the conclusion that for an equatorward field V_E of magnitude 1 V m^{-1}, $v_{\text{ion}} = 1$ km s^{-1} for $B_J = 10^{-3}$ T. [See Miller *et al.* (2006) and references therein for a fuller explanation of this.] Conversely, measured ion winds could be used to infer the value of the equatorward electric field, an important input into modeling energy inputs in the auroral-polar regions of Jupiter; see Sec. III.B.6.

The significance of the ion winds for Jupiter's upper atmospheric dynamics was made clear by using the JIM to model an event in which a voltage applied across the auroral oval was used to drive ion winds (Achilleos *et al.*, 2001).

This showed that the neutral gas picked up a considerable fraction of the ion velocity. Further JIM studies by Millward *et al.* (2005) showed that this could reach as high as 60% of the electrojet velocity at the H_3^+ concentration peak.

Two teams, Cowley and Bunce (2001) and Hill (2001), independently developed the original Hill (1979) theory of the breakdown of corotation in the middle magnetosphere around 15 to 20 R_J from the planet to explain the main Jovian auroral. This breakdown resulted in an azimuthal curvature of the magnetic field lines that in turn set up a current system from the equatorial magnetospheric plasma sheet along the magnetic field lines that closed through the auroral ionosphere. Following Huang and Hill (1989), Cowley and Bunce (2001) introduced a factor $k(h)$ that represented the height-dependent slippage of the neutral thermosphere from corotation as a result of coupling with ions that were being dragged back by the magnetosphere, with $k(h)$ given by

$$k(h) = 1 - \frac{\delta\Omega_n}{\delta\Omega_M}, \tag{4}$$

where $\delta\Omega_n = \Omega_J - \Omega_n$, $\delta\Omega_M = \Omega_J - \Omega_M$, and Ω_J is the angular velocity of Jupiter, Ω_n is the angular velocity of the neutral atmosphere in the auroral oval, and Ω_M is the angular velocity of the magnetosphere from where the magnetic field lines map onto the auroral oval. (Note that Ω_n is height dependent, while Ω_M is not.) Since measurements can only derive velocities averaged over the column of atmosphere observed, $k(h)$ was usually replaced by its height-integrated value K for comparison with measured H_3^+ ion winds. (Note that this K is not the same as the spectral quantum number K: context has to be used to distinguish the two.)

Calculations also showed that electrons coming from the equatorial plasma sheet to provide the currents that closed in the ionosphere had to be accelerated to ~100 keV to supply sufficient charge carriers. Cowley and Bunce (2001) also estimated the *effective* height-integrated Pedersen conductivity Σ_P^* of the auroral ionosphere to be between 0.2 and 1 reciprocal ohms (mho), where $\Sigma_P^* = (1 - K)\Sigma_P^*$, with Σ_P the actual Pedersen conductivity. This modification would prove essential in calculating the energy balance in the upper atmosphere of Jupiter and other giant planets.

Our understanding of the vertical profile of upper atmosphere winds has been enhanced by the work of Chaufray *et al.* (2010, 2011). In the latter study, they measured H_3^+ velocities in Jupiter's auroral regions, again showing the strongest flows in the dawn polar region of the planet. The wind speeds of ~3 km s^{-1}, however, were of somewhat higher velocity than those measured by Stallard *et al.* (2001), which were around 1–2 km s^{-1}. However, Chaufray *et al.* (2011) were measuring lines from the overtone $2\nu_2$ band in the 2 μm spectral region which probe altitude and pressure levels around 1 nbar in the middle theromosphere, unlike the 1.0–0.1 μbar level to which the fundamental ν_2 fundamental lines used by Stallard *et al.* (2001) were sensitive, which is closer to the homopause. Chaufray *et al.* (2011)'s observations were taken in the 2 μm spectral region, which could also probe simultaneous neutral wind velocities using H_2 quadrupole emission. These lines showed the neutral atmosphere to be close to corotation at the 1 nbar level, with apparent motion away from rotation frustratingly below the measured noise. (Unfortunately, there are no H_2 lines that can be measured in the ν_2, 3–4 μm window.)

Thus, the picture revealed by a combination of the winds derived from the ν_2 (1.0–0.1 μbar pressure level) spectra and the $2\nu_2$ (10^{-3} μbar pressure level) is one where the westward ion velocity in the planetary reference frame increases from 1–2 to ~3 km s^{-1} with increasing altitude and decreasing pressure. Although we have no information about the neutral winds at the 1.0–0.1 μbar pressure level, models such as that of Achilleos *et al.* (2001) and Millward *et al.* (2005) predict that $k(h)$ will be between 0.3 and 0.6 at this level. Therefore, neutral winds of anywhere between 0.3 and 1.2 km s^{-1} might be expected. But at the nanobar level, Achilleos *et al.* (2001) predicted that $k(h)$ would be close to zero, so any neutral winds should similarly be ~0, as Chaufray *et al.* (2011) found. At this level, the ions, responding to the lag to corotation of the magnetic field lines that pass through the middle magnetosphere, are almost completely decoupled from the neutrals in the thermosphere. The ion winds measured at the nanobar pressure level, in turn, then give a good measure of the true lag to corotation of the middle magnetosphere.

Chaufray *et al.* (2010) previously used the Hubble Space Telescope to look for Doppler shifting in the atomic-H Lyman-α emission, measuring 4–8 km s^{-1} probably supersonic winds in the upper thermosphere at the 10^{-11} bar level/1500 km. This altitude is much higher in the atmosphere than the H_3^+ peak emissions, where ion winds are measured, and confirms that at these rarified atmospheric levels the upper thermosphere and lower exosphere is entirely decoupled from the ionosphere, which is still tied to the rotation rate of the middle magnetosphere (i.e., a planetary westward drift of ~3 km s^{-1}).

Measurements of Jupiter's ion winds by both Stallard *et al.* (2001) and Chaufray *et al.* (2011) provided measurements of the wind structure only in strips cutting through the auroral region. Johnson *et al.* (2017) provided a significant step forward in these measurements by scanning the slit across the auroral region, resulting in a scanned two-dimensional (2D) map of emission intensity and line-of-sight velocity (shown in Fig. 8). These showed similar flow morphology to the past studies, but in much greater detail. The region fixed at a zero inertial velocity, directly associated with field lines swept into the magnetotail by the solar wind, was shown to be confined to a much narrower region around the pole, directly mapping to the region described as the dark region in UV auroral observations (Grodent, Clarke, Waite *et al.*, 2003). In addition, a region of superrotation was observed equatorward of the dawn aurora, suggesting either a region of superrotation within Jupiter's inner magnetosphere or, alternatively, a neutral wind accelerating the ions in this region as predicted by Nichols and Cowley (2004) and Yates, Achilleos, and Guio (2014).

6. Energy considerations

The problem of the energy gap, noted for all of the Solar System's giant planets [see Yelle and Miller (2004)], was

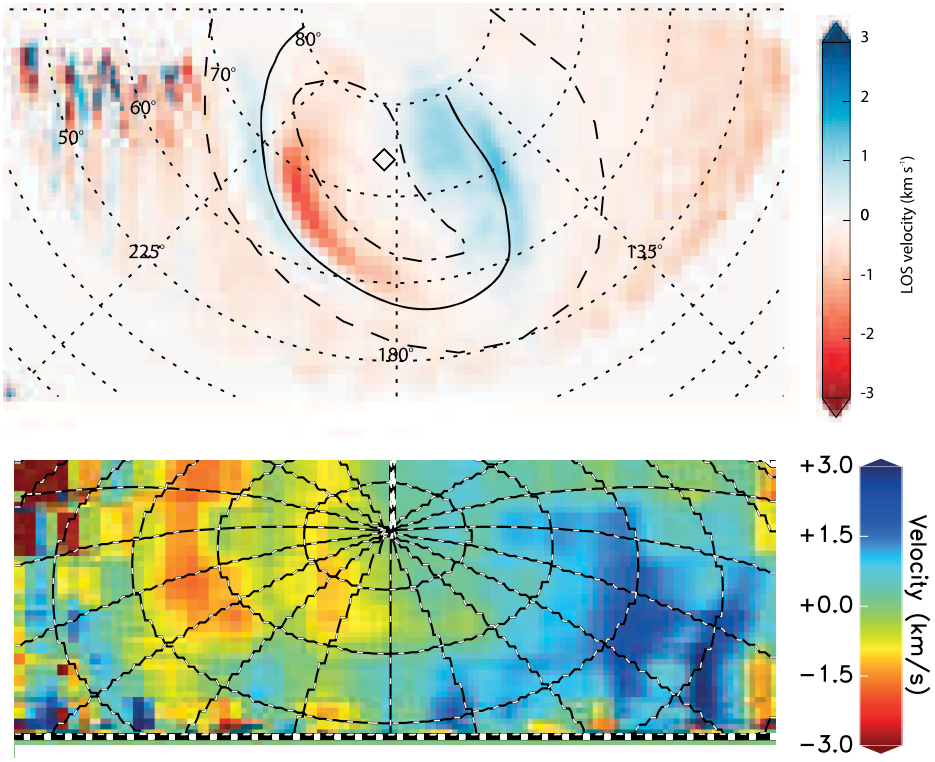

FIG. 8. Jupiter's and Saturn's auroral H_3^+ ion wind line-of-sight velocities. (Top panel) Jupiter's ion winds in the planetary frame of reference observed by VLT CRIRES showing significant structures across the entire auroral region, both equatorward and poleward of the main auroral region (marked by the solid line). The solid line marks the peak H_3^+ auroral intensity along the main auroral emission as measured by Johnson *et al.* (2017), the dashed line shows the location of the magnetic footprint of Io according to the Grodent *et al.* (2008) model, and the dot-dashed line bounds the fixed dark polar region as defined by Stallard *et al.* (2003). From Johnson *et al.*, 2017. (Bottom panel) Saturn's ion winds in the planetary frame of reference observed by Keck NIRSPEC, shown here as a scanned image, with strong subrotation across the auroral region and narrow arcs of flow across the pole, with lines of latitude and local-time longitude shown by dashed lines separated by 10° and 20°, respectively. From Stallard *et al.*, 2019.

introduced previously. Analysis of results from spacecraft and ground-based observations showed that exospheric temperatures calculated from solar inputs alone were much lower than those measured. These are set out in Table III from Yelle and Miller (2004). Solar inputs account for a small fraction of the difference in temperature between the homopause and the final temperature at the top of the atmosphere. Questions arise as to whether or not energy inputs are vertical (from below or above) or from higher to lower latitudes. One explanation involving gravity waves propagating from the lower atmosphere has been hotly contested; see Matcheva and Strobel (1999) and Yelle and Miller (2004). Also possible was the meridional transfer of energy from higher to lower latitudes. We discuss problems with this proposal further in the section on Saturn, for which similar considerations are relevant.

As previously outlined, Grodent, Waite, and Gérard (2001) used the atmospheric profile derived from the *Galileo* probe (Seiff *et al.*, 1997; Seiff *et al.*, 1998) to constrain their one-dimensional (1D) model of the Jovian auroral atmosphere. They also used H_3^+ measurements to set their temperature at the ion peak. This model and its derivatives were important for determining energy changes during events on Jupiter and Saturn.

Three-dimensional (3D) modeling studies using the JIM (Achilleos *et al.*, 1998) showed that influxes of high-energy electrons into the auroral atmosphere could produce Σ_P values of several mho, and that for electrons with an individual energy of 60 keV seemed most effective at producing conductivity (Millward *et al.*, 2002). It also demonstrated that the maximum local conductivity was due to the formation of H_3^+ rather than H^+ ions. Further modeling (Millward *et al.*, 2005) showed that values of V_E of tenths of a $V\,m^{-1}$ to a few $V\,m^{-1}$ equatorward across the auroral-oval-generated ion winds of between $0.12\ km\,s^{-1}$ for $V_E = 0.2\ V\,m^{-1}$ and $1.7\ km\,s^{-1}$ for $V_E = 2\ V\,m^{-1}$. The energy input to the upper atmosphere was enhanced by not only the energy of precipitating electrons but also the acceleration of the ions and the subsequent ion drag effects on the neutral ions entrained in the auroral oval. These two effects were given by

$$H_J = [(1-K)V_E]^2\Sigma_P \qquad \text{(Joule heating)}, \tag{5}$$

$$H_D = K(1-K)V_E^2\Sigma_P \qquad \text{(ion drag heating)}, \tag{6}$$

which gave

$$H_{tot} = (1-K)V_E^2\Sigma_P \qquad \text{(total heating)}. \tag{7}$$

Adding to this, Smith *et al.* (2005) showed that if the electric field were fluctuating, then this amount could be doubled since the Joule heating would be significantly increased. No observational evidence for such fluctuations has been forthcoming, however, on timescales of a minute (Lystrup *et al.*, 2007).

Since values of the K parameter could be as high as ~0.6 for high-energy (60 keV) electrons and $V_E = 2$ V m^{-1} (Millward *et al.*, 2005), Miller *et al.* (2006) calculated that the total input from Joule heating and ion drag terms could be more than 10^{14} W, much more than the total energy due to particle precipitation in the auroral regions and the planetwide absorption of solar EUV radiation, which combined gave between 5×10^{12} W and 10×10^{12} W for Jupiter (Satoh and Connerney, 1999a; Yelle and Miller, 2004), depending on the solar wind and magnetospheric conditions.

This picture was also confirmed independently by results from the Jupiter Thermospheric General Circulation Model (JTGCM) (Bougher *et al.*, 2005). JTGCM was able to run to full equilibrium by making use of the Grodent, Waite, and Gérard (2001) vertical profile of ion densities rather than calculating the chemistry at every time step and assuming an initial vertical temperature profile across the entire planet. Using this they found that the unmodified Grodent, Waite, and Gérard (2001) profile caused excessive heating in the auroral-polar regions that led to unphysical upper atmosphere temperatures once Joule heating and ion drag [which were not included in the Grodent, Waite, and Gérard (2001) model] came into play. To deal with this and get temperatures that matched those derived from observations they had to reduce the heating effects due to ion drag by a factor of ~3. It was also necessary to assume a planetwide flux of low-energy particles to heat the upper reaches of the thermosphere at lower latitudes to match the temperature profile observed by the *Galileo* probe (Seiff *et al.*, 1997).

This was an important result since it indicated that meridional winds alone could not transport sufficient energy from the auroral zones to heat the lower latitude thermosphere (Bougher *et al.*, 2005). It also provided some explanation for the planetwide H_3^+ emission (noted previously) and x-ray emission observed by the ROSAT satellite (Waite *et al.*, 1997). Bougher *et al.* (2005) further showed that cooling by H_3^+ in the atmosphere around pressure levels above the homopause (usually located between 1 and 0.1 μbar for Jupiter) was complemented by hydrocarbon emission at or below this level. Smith and Aylward (2009) modeled various wind, conductivity, and heating parameters for an axisymmetric 2D Jupiter model. They concluded that neither steady heating effects at high latitudes nor fluctuating fields could account for the high thermospheric temperature at the equator (900 K) while keeping temperatures in the auroral-polar regions (latitudes $> 75°$) within the 750–1250 K measured by H_3^+ observations. Instead, they proposed electric field fluctuations at latitudes $< 80°$.

In calculating the energy balance in planetary thermospheres, it had been useful to assume that excited H_3^+ vibrational energy levels were in "quasithermal" equilibrium (Miller, Joseph, and Tennyson, 1990). Studies using the BEAR imaging Fourier transform spectrometer (Maillard, 2000) instrument on the CFHT, however, showed that there were limitations to this approximation (Yelle and Miller, 2004) and that temperatures in the H_3^+ ($v_2 = 3$) level at 960 K were > 200 K lower than those on the $v_2 = 2$ level (Lellouch, 2006). Melin *et al.* (2005) therefore used detailed-balance calculations [based on Oka and Epp (2004) methodology] combined with scaled versions of the Grodent, Waite, and Gérard (2001) profile to interpret the energy balance in the Jovian auroral upper atmosphere during an "auroral event" that occurred from September 8 to September 11, 1998 (Stallard *et al.*, 2001, 2002).

They found that during the event the upper atmosphere started with heating and cooling terms nearly balanced, with just 7.4 mW m^{-2} net excess heating on average across the auroral-polar regions, once heating due to particle precipitation and Joule heating and ion drag were balanced by downward conduction and H_3^+ and hydrocarbon cooling (Melin *et al.*, 2006). But three Earth days later there was over 175 mW m^{-2} of excess heating, due mainly to a fourfold increase in the Joule heating and ion drag contributions that resulted from a doubling of the ion velocity in the auroral electrojet and its modeled impact on generating neutral winds (Melin *et al.*, 2006). This could, within the uncertainties in the model calculations, account for the ~80 K increase in average temperature observed between September 8 (981 K) and September 11 (1065 K) (Stallard *et al.*, 2002; Melin *et al.*, 2006).

Later work by Johnson *et al.* (2018) looking at the auroral-polar regions as a whole, however, found no significant correlation between temperature and total emission. Thus, H_3^+ may not be an entirely efficient thermostat across the whole auroral region, and the lack of direct correlation with either column density or ion winds also suggests that heating from particle precipitation and Joule heating, respectively, may not completely determine H_3^+ temperatures either (Johnson *et al.*, 2018).

The results of Melin *et al.* (2006) showed that modeling Jupiter's atmosphere in the steady state could miss the intrinsic variability of the planet and its interactions with its space environment. This issue was tackled by Yates, Ray, and Achilleos (2018), who used actual solar-wind data from the *Pioneer 10* spacecraft to model the coupling of the multiple shocks and rarefactions that resulted in Jupiter's magnetosphere with a self-consistent model of the upper atmosphere. Their aim was to see whether such a variable magnetosphere-ionosphere interaction could carry the large amounts of energy generated in the auroral-polar regions by Joule heating and ion drag to lower latitudes, and account for the high temperatures observed there. They found was that such driving of the upper atmosphere could indeed produce heating at lower latitudes. But the eventual temperature increase produced was only ~7.6 K after 100 Jovian days, with a maximum increase of 15 K during the whole simulation period. Yates, Ray, and Achilleos (2018) therefore concluded that "the magnetospheric interaction is unlikely to be solely responsible for the observed high temperatures in Jupiter's upper atmosphere."

C. Saturn

1. The aurora

The magnetic field of Saturn is considerably more symmetric than that of Jupiter, with the rotational and magnetic axes nearly coinciding, and the surface value of B is just 21 μT, less than that at Earth, and more than an order of magnitude less than Jupiter. This makes its magnetosphere more susceptible to influences from the solar wind than the Jovian system. The circumpolar oval traced by Saturn's brightest auroral emissions (the main Saturnian oval) is located at ~75° latitude in both hemispheres, aligning closely to the boundary between open and closed field lines in the magnetosphere. This made Saturn's auroras appear to be similar to those of Earth. In principle, therefore, the Saturnian system could be considered simpler than the jJovian. Although the H_3^+ emission from Saturn has been known to be largely auroral in nature from the time it was discovered in 1992 (Geballe, Jagod, and Oka, 1993), its rather low intensity meant that ground-based imaging studies had not proved successful.

The understanding of Saturn's H_3^+ aurora fundamentally changed following the arrival of the *Cassini* mission in 2004. The first spatially detailed maps of these auroras were made using *Cassini*'s Visual and Infrared Mapping Spectrometer (VIMS) (Brown *et al.*, 2004). These showed a main auroral oval similar to that observed in the UV but highlighted the determination that the polar emission was significantly different, with both auroral arcs and and polar-cap brightening observed (Stallard, Miller, Lystrup *et al.*, 2008); see Fig. 9.

Melin, Stallard, Miller, Gustin *et al.* (2011) provided the first detailed simultaneous comparison between the UV and IR auroras. Using high-spatial-resolution spectral images from *Cassini*'s VIMS and UVIS instruments, they were able to measure a narrow segment of the H and H_2 neutral emission and the H_3^+ ion emission at and around the main auroral oval. These showed H, H_2, and H_3^+ emission to be morphologically identical in the bright main auroral oval (~73°S) but revealed two additional arcs, an equatorward arc seen predominantly in H (~70°S), and a poleward arc (~74°S) seen mainly in H_2 and H_3^+.

Badman, Andrews *et al.* (2012) averaged a significant number of *Cassini* VIMS images taken between October 2006 and February 2009 to produce maps of global auroral emission strength and morphology. These revealed that both northern and southern auroras were brightest in the dawn-to-noon region, with the southern aurora also enhanced in the dusk-to-midnight sector. Similar enhancement to the UV average emission was subsequently found by Carbary (2013). However, unlike the UV aurora, significant emission was also found in the auroral-polar region, poleward of the main oval, with a general enhancement across the entire pole and a localized arc of emission crossing from noon to midnight on the dawn side of the pole.

Badman, Achilleos *et al.* (2012) analyzed multiple intense auroral arcs separated by dark regions poleward of the main oval observed by the *Cassini* VIMS instrument, which appeared to have similar morphology to arcs previously observed in the UV. In combining H_3^+ images with *in situ* measurements of magnetic field and particle data, these auroral arcs were interpreted as the ionospheric signatures of bursts of reconnection occurring at the dayside magnetopause, associated with upward field-aligned currents, the magnetic signatures of which were detected by *Cassini* at high planetary latitudes.

Lamy *et al.* (2013) presented a detailed comparison of emissions from multiple wavelengths in Saturn's auroral-polar regions for January 2009. This again showed that, unlike UV emissions, the polar H_3^+ emissions were approximately as bright as the main oval. Calculations of energy balance showed that H_3^+ and UV emissions radiated out $\sim 3.5 \times 10^{11}$ W.

Melin *et al.* (2016) made use of the UVIS, Imaging Science Subsystem, and VIMS instruments on *Cassini*, together with Hubble, Keck, and IRTF remote observations of Saturn's aurora, to observe and analyze Saturn's aurora at multiple scales in IR, visible, and UV wavelengths. This found that the overall UV brightness varied by significantly more than the overall H_3^+ brightness, and that the aurora varied across similar spatial scales and timescales. The main auroral emissions for all three wavelengths were found to be approximately colocated in the midnight sector. There was also an indication that the main noon H_3^+ aurora appeared to change in brightness with the planetary-period phase, suggesting enhanced currents from the planetary-period current system, as predicted by Provan *et al.* (2014).

Analysis of the field-aligned currents observed by *Cassini* as it passed repeatedly through Saturn's southern postmidnight auroral region were able to show that Saturn's main auroral oval is generated by two coincident current systems (Hunt *et al.*, 2014). The first is an axisymmetry current system associated with the breakdown in corotation within Saturn's middle magnetosphere. The second is a current system that rotates with the planet, and that has been used in the past to explain oscillations within Saturn's aurora [see, e.g., Nichols *et al.* (2008), Badman, Andrews *et al.* (2012), and Bader *et al.* (2018)], magnetospheric plasma (Gurnett *et al.*, 2007), and magnetic perturbation fields in many locations within the magnetosphere (Andrews *et al.*, 2008; Provan *et al.*, 2009; Clarke *et al.*, 2010). These *planetary-period oscillations* appear to show ongoing variations in the rotation rate of Saturn, with differing rates observed in the northern and southern poles (Gurnett *et al.*, 2009). By measuring the auroral currents at a variety of planetary phases, Hunt *et al.* (2014) were able to calculate both the phase-dependent and phase-independent currents, and they provided the first evidence that the currents moving with the planet might be driven by neutral winds within Saturn's upper atmosphere, the only example of a weather-generated aurora within the solar system, as originally predicted by Smith (2006).

The possibility that these rotating field-aligned currents could be generated within the atmosphere of Saturn has been suggested for more than a decade; see, e.g., Smith (2006), Jia, Kivelson, and Gombosi (2012), and Smith and Achilleos (2012). A possible mechanism is that these are driven by a neutral twin-cell vortex that couples with, and in turn drives, a current within the surrounding ionosphere. The resultant difference in neutral and plasma flows would produce Pedersen currents perpendicular to the flow of the neutrals, effectively identical to a current system produced by plasma

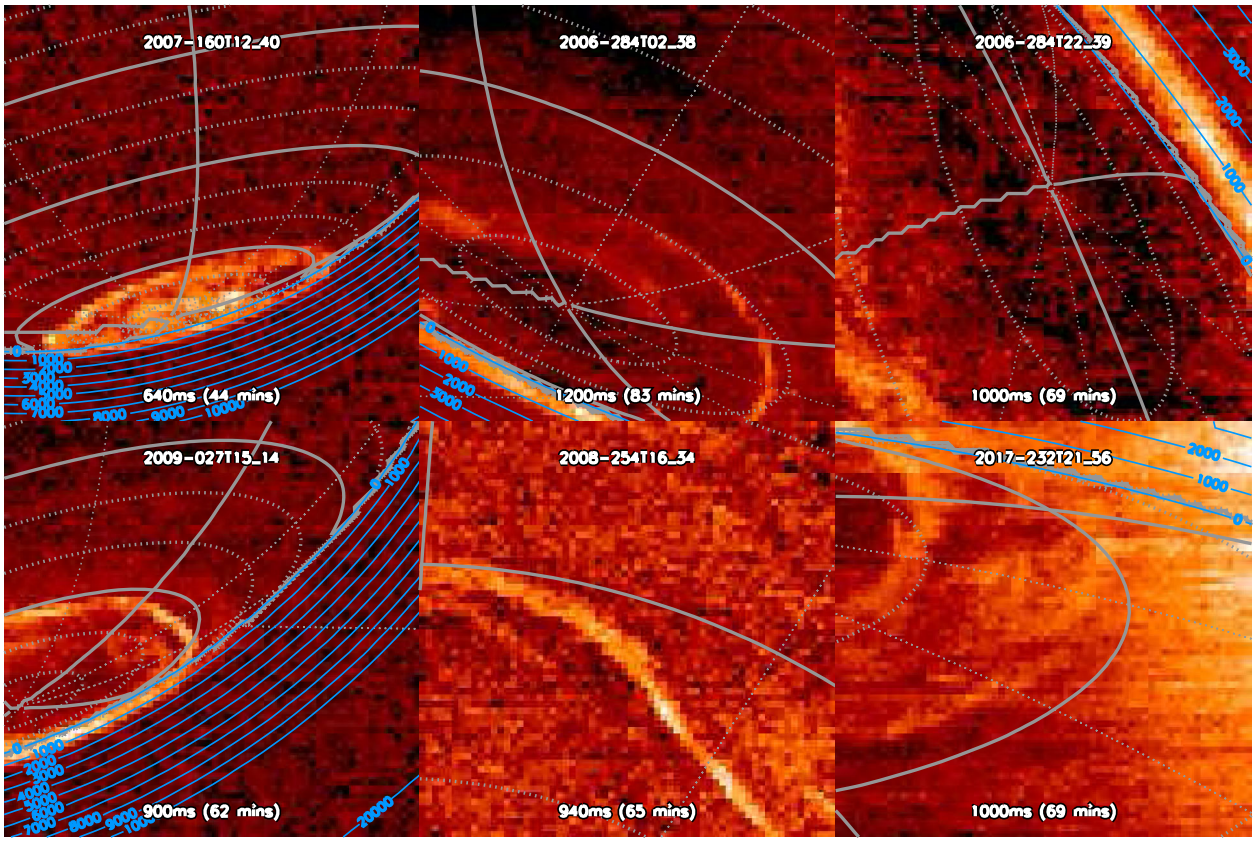

FIG. 9. Various images of Saturn's H_3^+ aurora, observed by the *Cassini* VIMS instrument. These images, taken throughout *Cassini*'s decade-long orbit of Saturn, reveal many of the instances where VIMS provided a unique insight into Saturn's aurora. Each image was constructed from light gathered from a range of VIMS wavelength bins bright in H_3^+ between 3.4 and 4.2 μm, with background light removed using a range of adjacent H_3^+ dark bins, described in more detail by Stallard, Melin, Miller, Badman *et al.* (2012). Latitudes are shown in steps of 5° (dotted lines) and 15° (three-dot-dashed lines), local-time longitudes in steps of 30° (dotted lines) and 90° (three-dot-dashed lines), and the "ray height" (the projected height above the 1 bar planetary surface on the limb) in steps of 1000 km (blue lines). The data and time are shown at the top of each image and the image exposure time (in milliseconds per pixel and minutes for the total image) is at the bottom. (Top left and center panels) Images among those used by Stallard, Miller, Lystrup *et al.* (2008) to highlight a narrow and bright main auroral emission, similar to that observed in the UV but with polar aurora unlike any previously seen at other wavelengths. (Top right panel) Image resolving Saturn's auroral curtain, used by Stallard, Melin, Miller, Badman *et al.* (2012) to reveal the H_3^+ altitudinal structure. (Bottom left panel) Image is one of those used by Lamy *et al.* (2013) to directly compare auroral emission from H_3^+ and UV auroras with simultaneous measurements of low-frequency radio emissions and images of energetic neutrals surrounding Saturn. (Bottom middle panel) Image is one of the highest-spatial-resolution images taken of any planetary aurora from space, which Melin, Stallard, Miller, Gustin *et al.* (2011) compared with UVIS images to correlate the H, H_2, and H_3^+ auroras. (Bottom right panel) Image is one of the last H_3^+ auroral images taken by *Cassini* before it crashed into Saturn; this image reveals complex morphology (partly obscured by sunlight on the right-hand side of the image, the result of the difficult observing conditions high above Saturn's pole), which will be described in more detail in future publications.

flowing in the opposite direction (Smith, 2011). H_3^+ ions with energies ranging between 30 and 200 keV have also been identified among other light ions flowing into the auroral region of Saturn by the *Cassini* Magnetosphere Imaging Instrument (Mitchell *et al.*, 2009).

2. Auroral temperatures

The upper atmospheric temperature of Saturn was a subject of some controversy for many years: Festou and Atreya (1982) obtained a value of 800 K from *Voyager* data, while Smith *et al.* (1983) obtained a value of 400 K from the same data. Measuring Saturn's H_3^+ temperatures proved difficult from Earth, where the weak emission meant instruments required both high resolution, to exclude the background reflected sunlight, and broad wavelength coverage, to observe multiple emission lines. Given that that was hard to achieve, Geballe, Jagod, and Oka (1993) obtained a value of 780 K by combining spectra from the northern and southern auroras, seemingly agreeing with Festou and Atreya (1982). But Melin *et al.* (2007) used spectral fitting techniques that had worked effectively for Jupiter to come up with temperatures from 380 K in September 1999 measurements to 420 K in February 2004, supporting Smith *et al.* (1983). Melin, Stallard, Miller, Gustin *et al.* (2011) later showed that the mean temperature along a small section of the main auroral arc was $T = 440(\pm 50)$ K, in good agreement with their previous derivations. Although no temperatures as high as the 800 K

value of Festou and Atreya (1982)have subsequently been derived, considerable temperature variations do occur in Saturn's upper atmosphere nonetheless.

The first global maps of Saturn's auroral temperature were made by the VIMS instrument on the *Cassini* spacecraft. The relatively low VIMS spectral resolution meant that local variations in the reflected sunlight and thermal emission could not be easily separated out from the H_3^+ emission itself. This made it hard to obtain reliable auroral temperatures. Stallard, Melin, Miller, O'Donoghue *et al.* (2012) took H_3^+ emission from above Saturn's limb, which is not affected by sunlight or thermal emission, and were able to measure the auroral temperature changing over time from 611 to 567($\pm$20) K over a period of about 4 h. This ~40 K drop in temperature corresponded to a cooling of between 3×10^{12} W and 8×10^{12} W across the auroral regions, similar in magnitude to the inputs due to Joule heating and ion drag (discussed later). Lamy *et al.* (2013) used multiple VIMS images to provide estimates of the thermospheric temperatures, which were found to be roughly constant over the whole auroral region and with time, averaging to ~410 K.

O'Donoghue *et al.* (2014) used the Keck telescope with the NIRSPEC instrument to provide the combination of higher spectral resolution, wide wavelength coverage, and high sensitivity needed to get a detailed measure of the H_3^+ physical parameters from Earth. They noted consistent temperatures throughout a2 h period, with temperatures of 527($\pm$18) K in the north and 583($\pm$13) K in the south. During this same period, column densities varied more significantly with time and appeared to be approximately anticorrelated with temperature, as shown by the average column densities of $156(\pm 0.32) \times 10^{15}$ m^{-2} in the north and $1.16(\pm 0.14) \times 10^{15}$ m^{-2} in the south. O'Donoghue *et al.* (2014) concluded that the hemispheric temperature difference was driven by an inverse relationship between the total thermospheric heating rate (Joule heating and ion drag) and the magnetic field strength, with a smaller southern magnetic field strength resulting in a higher Pedersen conductivity [predicted by Galand *et al.* (2011)], in turn producing an increased total heating rate and an increased temperature, irrespective of season.

O'Donoghue, Melin *et al.* (2016) measured the temperatures in three locations on the northern aurora, noon and midnight on the main oval and at the pole, and the noon southern aurora. This again showed a cooler northern noon main oval 418($\pm$18) K than the southern noon main oval 444($\pm$18) K, with significantly raised temperatures in the northern pole 433($\pm$13) K, and the northern midnight main oval (466($\pm$16) K. O'Donoghue, Melin *et al.* (2016) also showed a strong variation in auroral brightness with the phase of the planetary-period current system, which was shown to result from increasing column density. There was weak evidence for an anticorrelation with temperature with the planetary-period phase.

Chowdhury *et al.* (2019) measured localized H_3^+ temperatures across the northern auroral region, with an average temperature of 361($\pm$48) K, with a localized hot spot of 379($\pm$66) K potentially corresponding to a location where H_3^+ is failing to cool the thermosphere.

Stallard *et al.* (2019) produced the first maps of H_3^+ temperature across Saturn's auroral region, revealing sharp gradients in H_3^+ temperatures, with localized temperatures varying between 350 and 650 K across the auroral region. These localized regions of heating were somewhat stable over several Saturnian days but changed significantly over longer periods. However, the location of these hot spots did not appear to rotate with the planetary-period current system, as might be expected if this current system were generated by thermospheric neutral winds.

3. Measurements on the planetary disk

For Saturn, measurements on the disk are complicated by the planet's magnetic connection to the extensive rings system. Pole-to-pole spectral measurements along the noon (central) meridian indicated that, as well as its auroral emission, Saturn (like Jupiter) also had more emission from the body of the planet than could be explained by ionization due to insolation alone (Stallard *et al.*, 1999). Investigation of the H_3^+ emission equatorward of the main aurora by Stallard *et al.* (2010) found that this emission formed a broad ring at ~60° latitude (~30° colatitude). This latitude mapped magnetically onto the magnetosphere to a distance between 3 Saturn radii (R_S; $1R_S = 58\,232$ km) and $3.95R_S$, directly tying the broad ring emission to the torus of material orbiting with Enceladus. This relatively bright H_3^+ emission was distinct from the faint spot of UV emission that had been observed as connected magnetically to Enceladus itself (Pryor *et al.*, 2011). Stallard *et al.* (2010) proposed that the H_3^+ emission is caused by a breakdown-in-corotation current system between the Enceladus torus and the upper atmosphere, similar to Jupiter's main auroral emission.

O'Donoghue *et al.* (2013) discovered that Saturn's H_3^+ pole-to-pole emission also showed a sequence of intensity peaks and troughs. These regions of brighter and darker H_3^+ emission appeared to be mirrored in the two hemispheres, when the magnetic latitudes of the features were considered, suggesting that they were correlated magnetically, as illustrated in Fig. 10. Modeling by Moore *et al.* (2015) showed that this H_3^+ brightening could be explained as the result of water flowing into both the Northern and Southern hemispheres

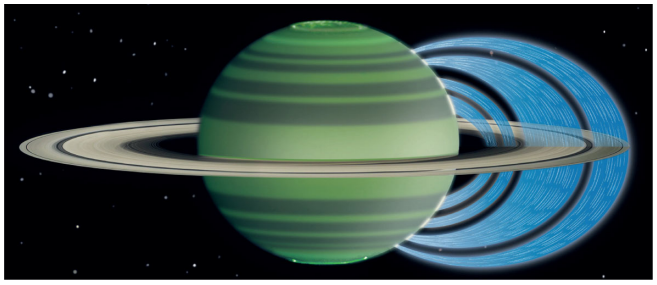

FIG. 10. Variations in Saturn's H_3^+ density with infalling water ions from the rings. This sketch shows the pathway of infalling water ions from their ionization within the rings, along magnetic field lines and into the planet, where they result in either increases or decreases in the H_3^+ column density $N(H_3^+)$ as a function of planetocentric latitude and corresponding magnetic field mapping.

from the rings. This influx removed electrons in the locations where it fell: reactions in the upper atmosphere resulted in the formation of H_3O^+, which then underwent rapid DR, with the removal of electrons as a result. The local reduction in electron densities caused by these reactions led to a corresponding reduction in the $H_3^+ + e$ DR loss process, and thus a local increase in the H_3^+ density. Only with extremely large values of water influx ($> 10^{12}$ m^{-2} s^{-1}) was the H^+/H_3^+ ionosphere destroyed completely, allowing water ion chemistry to dominate, as we discuss shortly.

The work of O'Donoghue *et al.* (2013) was thus the first direct evidence of ring rain, the infall of charged water ions from Saturn's rings precipitating along magnetic field lines onto the planet. This effect, first predicted by Connerney and Waite (1984), resulted in H_3^+ emission peaks mapping magnetically to gaps in the ring system. This ring rain was redetected using data from April 2013 (O'Donoghue *et al.*, 2017), and it is important in constraining models of Saturn's magnetic field at lower latitudes.

Recent reanalysis of the original ring-rain detection by O'Donoghue *et al.* (2019) confirmed this conclusion, showing regions of H_3^+ brightening at 45°N and 39°S matched by increasing H_3^+ density, alongside a local decrease in thermospheric temperature. At 31°S, however, a region with an expected high infall of water, a low H_3^+ density was measured: the rings in this region were depositing so much material onto the planet that H_3^+ destruction by charge exchange with incoming neutrals outweighed its lengthened lifetime due to the reduction in electron density.

O'Donoghue *et al.* (2019) estimated the water product influx using values from Moore *et al.* (2015), finding that between 432 and 2870 kg s^{-1} of water was required to explain the observed H_3^+ densities. This high rate of infall suggests that the ring-rain mechanism alone would drain Saturn's rings onto the planet in $2.92(+8.18/-1.24) \times 10^8$ yr, suggesting that they must have formed in the relatively recent past compared to the age of the Solar System.

This ring rain of water onto Saturn was, however, only a small part of the total ring input onto the planet. Observations made by *Cassini* in its final orbits provided the first *in situ* measure of the top of Saturn's ionosphere. During proximal orbit 287 (denoted P287), *Cassini* descended to an altitude of about 3000 km above the 1 bar atmospheric pressure level. Measurements by the Ion and Neutral Mass Spectrometer and Radio and Plasma Wave Science instruments showed that the equatorial ionosphere was dominated by heavy molecules, matched with a significant reduction in the ion densities of both H^+ and H_3^+, suggesting that these lighter species had chemically reacted with one or more heavy neutral molecular species (Waite *et al.*, 2018; Cravens *et al.*, 2019).

Modeling of this by L. Moore *et al.* (2018) revealed that Saturn's equatorial ionosphere was dominated by an unexpectedly large amount of of infalling neutral material originating in the rings, which appeared to be composed of organic molecules rather than water. This replaced light ions such as H^+ and H_3^+ with a range of other ion species, such as H_3O^+, HCO^+, HCO_2^+, N_2H^+, CH_5^+, and $C_2H_3^+$. It is clear, therefore, that the age of the rings suggested by O'Donoghue *et al.* (2019) is an upper limit.

Measurements from *Cassini* close to the equator also revealed an azimuthal current system at low latitudes (Khurana *et al.*, 2018). Khurana *et al.* suggested that this current may result from the wind shear in Saturn's lower atmosphere, combined with the northward offset of the magnetic field. However, this model conflicts with the model of Smith and Aylward (2008), which shows energy being transported meridionally, rather than vertically, in this region. The velocity shear that the model of Khurana *et al.* (2018) uses occurs in a similar latitude range as H_3^+ removed from the ionosphere by large fluxes of infalling neutral ring material.

4. The auroral curtain and altitude profiles

Galand *et al.* (2011) modeled Saturn's H_3^+ auroral curtain using both primary and secondary ionization from precipitating electron energies with a Maxwellian distribution in energy centered on differing mean energies. These produced modeled temperatures and column densities that were of the same order of magnitude as observations using UKIRT (Melin *et al.*, 2007). Galand *et al.* (2011) found that softer precipitation (e.g., 150 eV) resulted in higher densities (0.72×10^{16} m^{-2} at temperatures of ~500 K), but with ionospheric conductance dominated by solar ionization, while harder electrons (e.g., 2 keV) produced lower column densities (0.46×10^{16} m^{-2} and temperatures of ~480 K), with the ionospheric conductances proportional to the square root of the energy flux. These resulted in a peak electron density at altitudes of ~2600 and ~1600 km, respectively.

The auroral curtain was measured for the first time at Saturn by Stallard, Melin, Miller, Badman *et al.* (2012) (shown in Fig. 9), using *Cassini* VIMS observations that captured the aurora exactly on the limb of the planet. This observed the peak of Saturn's auroral H_3^+ emission at ~1155 km, close to the UV emission peak at 1145 km, as measured by the HST (Gérard *et al.*, 2009). The UV emission showed a kappa distribution with a significant tail of emission at higher altitudes. Measurements of hydrocarbon absorption in UV spectra indicated that in some cases the H_2 auroral emission peaked at heights above 610 km, while H_3^+ emission was distributed as a Gaussian. Stallard, Masters *et al.* (2012) suggested that the lack of higher altitude H_3^+ emission might be the result of the smaller H_2 scale height compared with H, resulting in relatively enhanced UV emission, due to Lyman-α, at higher altitudes. They hypothesized that the lack of lower altitude emission might result from the destruction of H_3^+ by hydrocarbons beneath the homopause.

5. Auroral ion winds and energy considerations

Cowley, Bunce, and Prangé (2004) produced a model based on understanding Saturn's auroral-polar regions as being a hybrid of those of Earth, with its well-known two-cell structure produced by Dungey (1961), with reconnection responsible for the main auroral oval and a lower latitude additional oval due to the Hill (1979) mechanism. Their analysis led to the conclusion that there should be an overall lag to corotation in the Saturnian polar cap given by

$$\Omega_{\rm ion} = \frac{\mu_0 \Sigma_P^* v_{SW} \Omega_S}{1 + \mu_0 \Sigma_P^* v_{SW}}, \quad (8)$$

where μ_0 is the permittivity of free space, Σ_P^* is the Pedersen conductivity in the rest frame of the neutral atmosphere coincident with the ionosphere, v_{SW} is the solar-wind velocity at Saturn, $\Omega_{\rm ion}$ is the angular velocity of the ions, and Ω_S is the angular velocity of Saturn. For $v_{SW} = 500\ {\rm m\,s^{-1}}$ and $\Sigma_P^* = 0.5$ mho, Cowley's result gave $\Omega_{\rm ion} = 0.24\Omega_S$.

Measurements of Saturn's H_3^+ ion winds in September 1998 indicated that $\Omega_{\rm ion}$ was $\sim 0.34\Omega_S$, which is in close agreement with the model results and suggests that the relevant Pedersen conductivity was 0.8 mho (Stallard *et al.*, 2004). As a result, some 5×10^{12} W of energy was being generated in Saturn's auroral-polar upper atmosphere by Joule heating and ion drag (Miller *et al.*, 2006). Again, this far exceeded the inputs from solar EUV radiation and particle precipitation at Saturn.

Further studies of Saturn's H_3^+ ion winds showed that while on some occasions it was fairly straightforward to fit the velocity profiles with a simple straight line, implying a constant proportional lag to corotation across the auroral-polar region, for others a more structured profile occurred (Stallard, Smith *et al.*, 2007). In particular, there was often a "central" auroral region located at the pole where there was almost complete corotation by the ions from colatitude 4° to the pole, with large deviations from corotation at colatitudes (4° to 23°). They termed this a "three-tiered structure." identifying the corotating region as mapping to an "old core" of field lines that were strongly twisted in the far magnetotail and no longer influenced by the flow of the solar wind past them (Stallard, Miller *et al.*, 2007).

Strong auroral brightening, coupled to changes from the three-tiered structure to one with a single slope, were associated with the magnetic reconnection of these twisted field lines. These workers also identified a "Jovian-like" aurora equatorward of the main (15° colatitude) oval that corresponded to the breakdown of corotation in the equatorial plasma sheet (Stallard, Miller, Melin *et al.*, 2008) at a colatitude ~25°. This is just poleward of the ~30° colatitude feature associated with Enceladus (Stallard *et al.*, 2010), and perhaps hard to distinguish from it in ground-based measurements.

Stallard, Masters *et al.* (2012) investigated the influence of the solar wind on both H_3^+ emission and ion wind structure, showing the changes in H_3^+ auroral morphology to match those observed in the UV, where strong dawn brightening occurs during major solar-wind compressions (Clarke *et al.*, 2005). They also showed that the typical three-tier H_3^+ velocity structure was lost following the arrival of a solar-wind compression at Saturn. This provided evidence for the theory originally suggested by Milan *et al.* (2005) and Stallard, Smith *et al.* (2007), that the central corotating region of the three-tier structure was associated with magnetic field lines open to the solar wind that spiral out into the tail of the magnetosphere. Surrounded by younger open field lines this old core reconnects only when large solar-wind compressions occur.

Past observations of H_3^+ ion wind velocities have not had the spatial resolution needed to reveal ion flows associated with the planetary-period current system. However, two recent publications evealed details of the ion winds that may indicate further complexity within the ion wind structures at Saturn. Chowdhury *et al.* (2019) described the first AO-corrected measurements of ion winds from Saturn, using the ESO VLT combined with the high spectral resolution CRIRES instrument ($\lambda/\Delta\lambda \sim 100\,000$). This produced an average line-of-sight velocity profile for the night, cutting across the auroral region from dawn to dusk through the planet's northern pole, revealing a small-scale ($\sim 1\ {\rm km\,s^{-1}}$) ion wind flow close to the pole, colocated with a localized dark region in the emission. This flow was in the noon-to-midnight direction, potentially indicating the presence of an ionospheric polar vortex.

Stallard *et al.* (2019) observed Saturn's auroral region on seven nights between July 25 and August 25, 2017, using the same slit-scanning technique previously used by Johnson *et al.* (2017) at Jupiter. Using reflected sunlight at nonauroral wavelengths, individual spectra could be positioned with unprecedented accuracy, resulting in the first ion wind maps at Saturn. These revealed a complicated pattern of ion winds consisting of multiple arcs of 0.5–1 ${\rm km\,s^{-1}}$ ion flows inside (poleward of) the main auroral emission, with different flow morphologies seen each night. In some instances there were mirrored flows on the dawn and dusk of the planet. These flows did not match with the predicted flows from models of axisymmetric currents driven by the outer magnetosphere or by the planetary periodic currents associated with Saturn's variable rotation rate. This suggested a level of complexity in the currents flowing between the ionosphere and magnetosphere that is not accounted for in current modeling. The three-tiered structure was, however, observed when all seven nights were averaged together, forming a cone of corotation starting in the noon sector and expanding out toward midnight. Stallard *et al.* (2019) concluded that since these observations were coadded in local time, wind structures associated with the planetary-period current system may be obscured, and further analysis may yetreveal details about the neutral atmosphere or ionospheric source for Saturn's variable rotation rate.

Initial 1D modeling of Saturn's upper atmosphere indicated that it would be possible to transfer the energy generated in the auroral regions to lower latitudes (Smith *et al.*, 2005). However, when ion-neutral coupling was taken into account, Coriolis forces actually took energy poleward in the steady state, causing an unexpected cooling known as the as the fridge effect (Smith *et al.*, 2007). Both UV (Grodent *et al.*, 2005; Pryor *et al.*, 2019) and H_3^+ imaging (Stallard, Miller, Lystrup *et al.*, 2008) by *Cassini*, and comparison of ground-based H_3^+ data obtained over several years (Melin *et al.*, 2007), showed, however, that the auroral-polar regions of Saturn were rarely in a steady state. Glocer *et al.* (2007) calculated that there would also be an outflow of H^+ and H_3^+ ions into the Saturnian magnetosphere that gave rise to a total particle outflow of between $0.21 \times 10^{27}\ {\rm s^{-1}}$ and $7.5 \times 10^{27}\ {\rm s^{-1}}$ integrated across the planet's entire polar cap, carrying energy away from the high-latitude regions into the magnetosphere.

D. Ice giants: Uranus and Neptune

1. Uranus

The first measurements of H_3^+ emission in Uranus by Trafton *et al.* (1993) revealed a remarkably high H_3^+

temperature of 740 K (±25 K) and a column density of 6.5×10^{14} m^{-2}, a large fraction of that of the Jovian densities, despite the fact that Uranus receives about 15 times less sunlight than Jupiter and has a much smaller and less energetic magnetosphere to deposit energy in the form of precipitating particles.

Lam, Miller *et al.* (1997) reported images taken in April 1993 and spectra taken in June 1995 that showed considerable spatial and temporal variation. These limited any auroral enhancement to ~20% of the total disk emission; see Fig. 11 for comparable images. They also found that the average temperature was around 677 K, within a range from 663 to 700 K, cooler than the original 1992 detection temperature. Satellite measurements from the Infrared Space Observatory (ISO), however, indicated a temperature of 800 K in 1997 (Encrenaz *et al.*, 2000). Overall, the brightness could vary by a factor of 2 from year to year. This work was followed up by more detailed analysis of the same data by Trafton *et al.* (1999), which included a comparison with the $v = 1 - 0$ band of H_2. This showed that molecular-hydrogen emission was uniform across the planet, with some evidence for limb brightening. This was in contrast to the H_3^+ emission that was strongly peaked toward the center of the planet. It was also clear that $T(H_3^+)$ and $T(H_2)$ were lower in 1995 than they had been at the time that H_3^+ emission was first detected. Planetwide emission $E(H_3^+)$ had roughly halved from 2.2×1011 W in April 1992 to 1.1×10^{11} W in June 1995.

Melin, Stallard, Miller, Trafton *et al.* (2011) used measurements of H_3^+ to show that the temperature of Uranus's thermosphere has been decreasing steadily since the molecule was first detected in 1992, with the exception of the 1997 ISO result, possibly the result of a seasonal variation in thermospheric temperatures. These same observations showed that the H_3^+ density showed little relation to the solar cycle. More recent analysis (Melin *et al.*, 2013, 2019) showed that rather than the expected increase following equinox the temperatures have continued to drop, with the most recent temperatures < 500 K. Since this period of cooling is 27 yr long, longer than the 21 yr seasonal cycle, Melin *et al.* (2019) suggested that it may be linked to auroral Joule heating being modulated by an offset and asymmetric magnetic field, making the northern summer solstice hot and the southern winter solstice cold.

Observations using the Hubble Space Telescope provided the first detection of a UV aurora at Uranus since the *Voyager* mission, revealing small-scale bright spots occurring irregularly across the disk of the planet (Lamy *et al.*, 2012, 2017); see Fig. 11. Using the ESO VLT, Stallard, Melin, Miller,

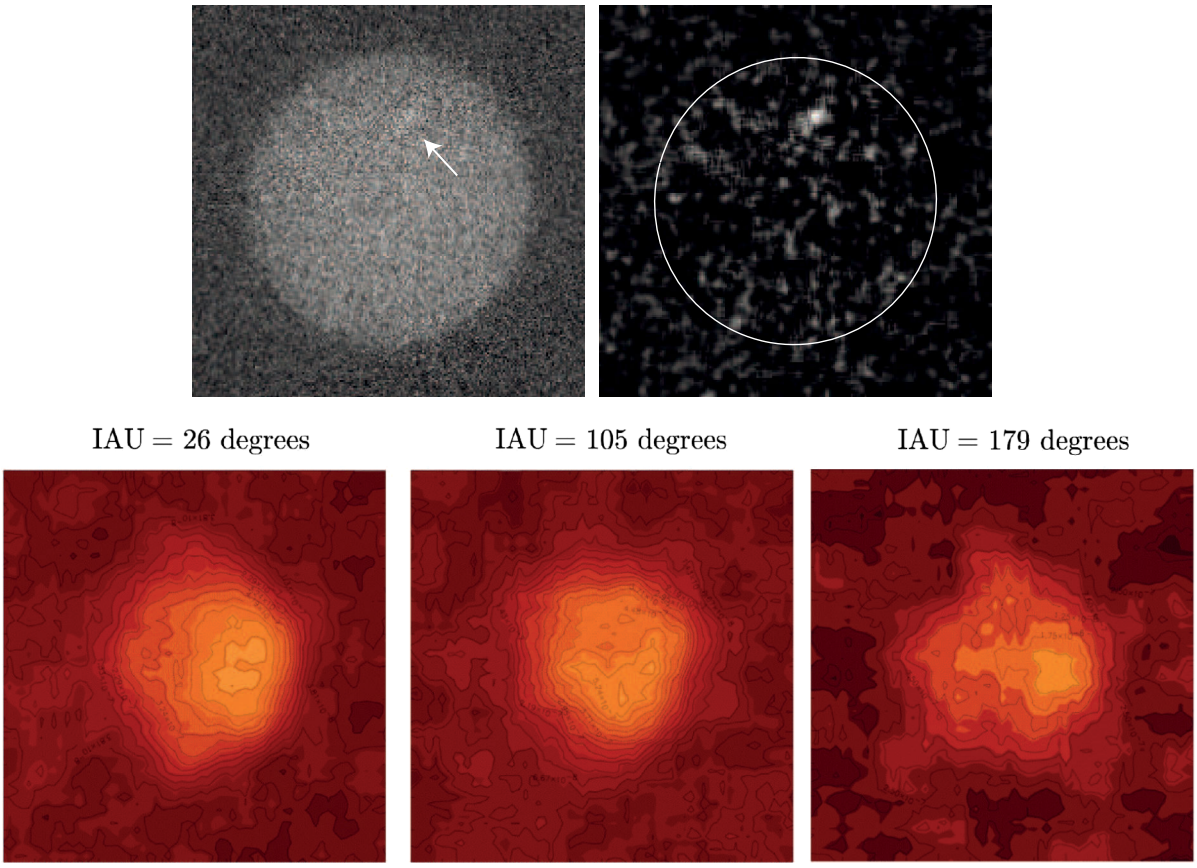

FIG. 11. Images of Uranus in the UV and IR. (Top panels, gray scale) One of the HST STIS instrument UV auroral images observed by Lamy *et al.* (2012), before (left panel) and after (right panel) background reflected sunlight was removed, showing a small auroral spot on the disk of the planet. (Bottom panels) Three images of H_3^+ emission from Uranus taken with the NFSCam on IRTF. These show the planet rotating by half of a Uranian day, with clear variability over this time. Melin (2006) concluded that the degree of spatial variability indicated possible auroral variation, but that no clear structure could be resolved. From Melin, 2006.

O'Donoghue *et al.* (2012) were able to show that the pole-to-pole H_3^+ emission from Uranus was slightly enhanced around auroral latitudes, providing a second indirect detection of the H_3^+ aurora.

Although H_3^+ aurora at Uranus still remains to be definitively detected, recent observations by Melin *et al.* (2019) showed a strong enhancement in H_3^+ brightness that was most easily explained as auroral. This observation measured the dawn limb of Uranus with spectra separated by 2.5 h, with the second of these observations showing a strong enhancement in the observed H_3^+ intensity. H_3^+ temperature and density could not be calculated for this feature, and it was unlikely to have been produced by a localized hot spot, as no contemporaneous tropospheric storms were seen in this period. As a result, it is highly likely that this enhancement was the first auroral H_3^+ emission directly detected at Uranus.

2. Neptune

Despite a series of observations over the past 25 yr, H_3^+ has never been detected at Neptune (Trafton *et al.*, 1993; Encrenaz *et al.*, 2000; Feuchtgruber and Encrenaz, 2003; Melin, Stallard, Miller, Lystrup *et al.*, 2011; Melin *et al.*, 2018). The most recent observations by Melin *et al.* (2018) derived an upper limit of the H_3^+ column density of $1.0(+1.2/-0.8) \times 10^{13}$ m^{-2} for a temperature of 550 K. This nondetection is perhaps not unexpected. Although *Voyager 2* detected diskwide UV H_2 emissions on Neptune's nightside (Sandel *et al.*, 1990), the only indication this emission was auroral was that the brightness peaked in the Southern Hemisphere, which was interpreted as auroral emission about the southern magnetic pole. This emission, along with *Voyager 2* measurements of radio emission close to the auroral zone of the northern magnetic hemisphere (Leblanc and Ladreiter, 1992), remains the only observational evidence for the aurora of Neptune at any wavelength. Neptune's auroral emission is predicted to be comparatively weak, with modeling by Masters (2015) showing that the conditions at the magnetopause are less favorable for magnetic reconnection than at the magnetopause boundary of any other Solar System magnetosphere, making the likelihood of a bright aurora small.

Using *Voyager 2* radio occultations, Lyons (1995) modeled the vertical distributions of several related species, including H_3^+, from the altitude profile of ionospheric electrons. This predicted a peak density at about 1400 km (~1.1 nbar) above the 1 bar level with a volumetric density of 1.1×10^6 m^{-3}. At this altitude, the temperature of the upper atmosphere is ~550 K (Broadfoot *et al.*, 1989), although this region coincides with the thermospheric temperature gradient, which is steep enough to provide significant uncertainties. However, the measurements of Melin *et al.* (2018) suggested that this model overestimated the H_3^+ density by at least a factor of 5. This strongly implies that H_3^+ emission cannot be detected at Neptune with current instrumentation and therefore must await observations by the James Webb Space Telescope, a future 30 m+ class telescope, or a future space mission before the presence of H_3^+ can be confirmed at Neptune.

IV. INTERSTELLAR H_3^+

A. Introduction

The existence of H_3^+ in interstellar molecular clouds was predicted six decades ago (Martin, McDaniel, and Meeks, 1961). Almost five decades ago it became clear that proton-hop reactions of H_3^+ with neutral atomic and molecular species are the initial steps in chains of ion-neutral reactions that ultimately result in the production of several abundant interstellar molecules that already had been discovered and many molecular species that were yet to be detected (Herbst and Klemperer, 1973; Watson, 1973a). Four decades ago the fundamental rovibrational band of H_3^+ was first observed in the laboratory (Oka, 1980), allowing the first searches for it in interstellar space (Oka, 1981; Geballe and Oka, 1989). The eventual detection of interstellar H_3^+ (Fig. 12) and the determinations of its abundances in dense clouds (Geballe and Oka, 1996) were the ultimate verification of the importance of ion-neutral gas-phase interstellar chemistry.

H_3^+ has now been observed in a variety of interstellar environments in the Milky Way, including in its central region (Fig. 13) and has even been detected in distant galaxies. Moreover, the scientific value of observing H_3^+ goes far beyond verifying the importance of gas-phase ion-neutral chemistry. Observations of this simplest of polyatomic molecules provides key astronomical information unobtainable by other means.

Because of the simple ways in which H_3^+ is produced and destroyed, its measured abundance in a cloud is more directly linked than any other probe to the rate of ionization of atoms and molecules by cosmic rays, high-energy particles that strongly influence the chemistry and physics in the cloud. Moreover, the unique rotational energy level structure of H_3^+, with its widely separated levels and its combination of strictly forbidden and weakly allowed transitions between them, has proved to be invaluable for deducing the physical conditions in clouds in the spiral arms of the Milky Way, especially so in the much more extreme interstellar environment near its center.

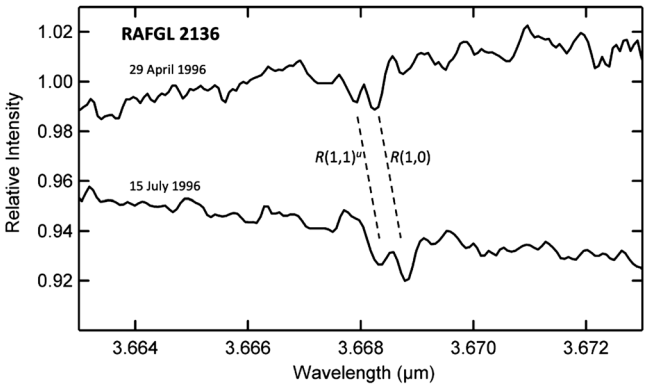

FIG. 12. Discovery spectrum of H_3^+ in a dense cloud toward the young massive protostar RAFGL 2136 by Geballe and Oka in 1996, obtained at UKIRT at a spectral resolving power ($\lambda/\Delta\lambda$) of 15 000. The shifts in the observed wavelengths of the two lines between the two observation dates are caused by the change in Earth's orbital velocity.

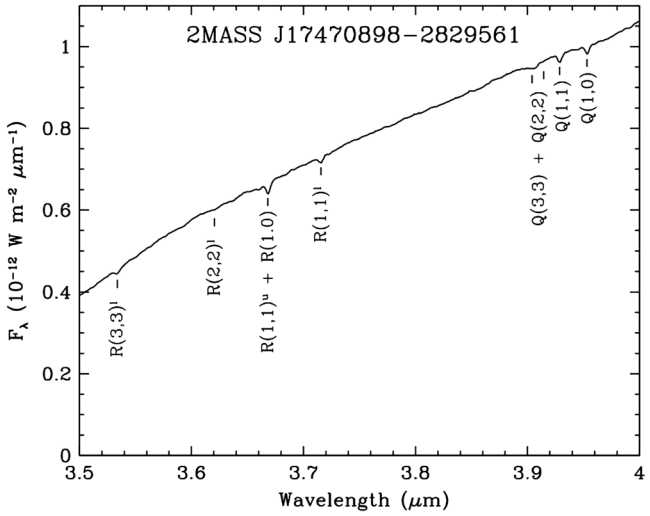

FIG. 13. Spectrum toward a bright star within the Galactic Center's Central Molecular Zone, approximately 100 pc from the central supermassive black hole, Sgr A*, obtained at the Frederick C. Gillett Gemini North Telescope at a spectral resolving power of 950. The star is embedded in an opaque shell of warm dust and gas, which emits a continuum steeply rising to longer wavelengths. All of the detected absorption lines in the spectrum are due to H_3^+, whose concentration in the absorbing foreground gas is typically a few parts in 10^8. The line labeling system is described in Sec. III.B and the detected transitions are shown schematically in Fig. 14. The detection of the $R(2,2)^l$ line is somewhat marginal; however, it is present in higher resolution spectra (Goto *et al.*, 2011). The column density of absorbing H_3^+ toward this star is the largest observed to date.

In addition, within the coldest and densest molecular clouds deuterated isotopomers of H_3^+ are abundant (Stark, van der Tak, and van Dishoeck, 1999; Vastel, Phillips, and Yoshida, 2004). Like H_3^+, they are important starting points for a rich chemistry of deuterated molecular species in these regions.

B. Creation and destruction of interstellar H_3^+

The elemental composition of interstellar gas in the Milky Way is almost entirely hydrogen (approximately 93% of the atoms) and helium (approximately 7% of the atoms). The most abundant heavier elements, carbon, nitrogen, and oxygen, each make up only a few hundredths of a percent of the atoms in interstellar space. Much of the interstellar gas condenses gravitationally into clouds, whose properties separate most of them into two basic types. In dense ($n \gtrsim 1 \times 10^3$ cm^{-3}) clouds, which typically have dimensions of ~1 pc (1 pc $= 3.08 \times 10^{18}$ cm) and temperatures of a few tens of kelvins, almost all of the hydrogen within the clouds is in molecular form, as H_2 is shielded from photoionization (requiring $E > 15.4$ eV) by the impinging external radiation field by atomic hydrogen at the cloud periphery, and is shielded from photodissociation by lower energy UV photons by UV-absorbing dust particles within the cloud.

In clouds with lower densities ($n \lesssim 3 \times 10^2$ cm^{-3} and thus also a lower density of dust particles), the so-called diffuse clouds, photoionization of H_2 within the cloud is still prevented if the cloud is sufficiently optically thick to ionizing UV radiation. However, in such clouds longer wavelength UV radiation ($E < 13.6$ eV) can still penetrate deeply. This inhibits the survival of some molecular species, most notably CO, and singly ionizes nearly all of the atomic carbon (ionization potential, 11.26 eV).

Although shielded partially or fully from UV radiation, neither type of cloud interior is shielded from cosmic rays. These high-energy particles, which are mainly protons that originate in galactic and extragalactic supernovae, the vicinities of black holes and other energetic astrophysical processes, permeate the Universe. When a cosmic ray enters a cloud it leaves behind it a trail of singly ionized H_2 molecules (H_2^+). Here we take the rate per H_2 molecule at which ionization by cosmic rays occur ζ to be 3×10^{-17} s^{-1}, which is within a factor of a few of almost all estimates made up until the turn of the century; for a summary of the history of estimates of ζ see Oka (2019).

The fate that befalls virtually every H_2^+ ion created by cosmic-ray ionization in a cloud is rapid destruction, and in the process production of H_3^+, via the well-known and rapid ion-molecule reaction $H_2^+ + H_2 \rightarrow H_3^+ + H$. Even in diffuse molecular clouds with only a modest fraction of hydrogen in molecular form, the rate at which this reaction occurs far exceeds ζ. Hence, the production rate of H_3^+ per unit volume in interstellar clouds is determined by the cosmic-ray ionization rate of H_2 times the density of H_2, which for dense clouds is approximately the cloud's particle density. This linear dependence on density is unlike the dependences of the rates per unit volume at which most molecular species are created. They are produced by reactions between species resident in the cloud, rather than interloping cosmic rays, and thus their production rates are typically proportional to density squared. As shown later, this difference gives the number density of H_3^+ a different functional behavior than the number densities of most molecules, which simply scale with the cloud density.

The inverse of the cosmic-ray ionization rate, roughly 1×10^9 yr, is the typical amount of time an isolated H_2 molecule would need to wait before it is ionized by a cosmic ray. On the other hand a molecular cloud core with a mass of ten Suns (10 $M_\odot$), perhaps the initial mass of the core out of which the Sun formed, contains 6×10^{57} hydrogen molecules. Even at this slow rate, roughly 2×10^{41} H_3^+ ions are created in that cloud core every second.

The H_3^+ thus produced is highly reactive with most neutral atoms and molecules of astrophysical interest, with the exceptions of He, N, Ne, and O_2; it is even more reactive with electrons (discussed later). In dense clouds, where electrons are scarce, the ion-neutral reactions that destroy H_3^+ are of the form $H_3^+ + X \rightarrow HX^+ + H_2$ and typically proceed on timescales determined by the Langevin rate coefficient, with coefficients of $\sim 2 \times 10^{-9}$ cm^{-3} s^{-1}. They are the initial steps in chains of reactions that lead to the formation of many observed molecular species, as was first recognized by Herbst and Klemperer (1973) and Watson (1973a). In the rarified clouds of interstellar space this ion-neutral chemistry occurs far more rapidly than the neutral-neutral chemistry (familiar to most from chemistry lab), as close encounters between atoms and molecules are rare and

for a reaction between neutral species to occur the reactants must overcome energy barriers that are virtually insurmountable at the temperatures of a few kelvins to several tens of kelvins in interstellar clouds.

In diffuse clouds, DR with electrons from singly ionized carbon ($H_3^+ + e \rightarrow H_2 + H$ or $H + H + H$) is by far the dominant destruction pathway for H_3^+ because the rate coefficient k_e for this reaction (McCall *et al.*, 2003) is 2 orders of magnitude higher than the coefficients for the proton-hop reactions of H_3^+ on neutral ions.

C. Considerations for spectroscopy of interstellar H_3^+

Because of its symmetric equilateral triangular structure, H_3^+ has no permanent electric dipole moment (the same is not true of its isotopomers H_2D^+ and D_2H^+). Normally this would mean that pure rotational transitions are forbidden. However, breakdown of symmetry due to the interaction between rotation and vibration of the molecular ion produces a small dipole moment. As a result, radiative transitions between rotational levels of H_3^+ that are not forbidden by selection rules can occur, although they are slow. Although these transitions are virtually impossible to observe in interstellar clouds they can significantly affect the population distribution in the lowest rotational levels, as discussed in Sec. IV.E.

By far the strongest transitions of H_3^+ are in its asymmetric vibrational bending (ν_2) band. Because H_3^+ is so highly reactive, its steady state concentration in dense clouds is low, as discussed later, typically a few parts in 10^8. In practice this means that even in this band its spectroscopic signature in interstellar clouds is weak. However, the quadrupole-induced IR transitions of the fundamental vibrational band of H_2, which is by far the most abundant molecule but which has no dipole moment, are $\sim 10^9$ times weaker than the dipole-induced ν_2 transitions of H_3^+, and thus the IR absorption lines of H_2 are usually considerably weaker than those of H_3^+.

Figure 14 shows the portion of the energy level diagram of H_3^+ relevant to spectroscopy of H_3^+ in interstellar clouds. In the ground vibrational state the lowest $(J, K) = (0, 0)$ level and all levels with J even and $K = 0$ do not exist due to the Pauli principle, as indicated in the figure; in addition, excited vibrational states in Fig. 14 with $J \geq 2$ and $K \geq 1$ are split into upper (u) and lower (l) levels, with transitions to them labeled accordingly. [See McCall (2001), Oka (2013), and Sec. II.B for a more thorough discussion of these features.] The energy difference between the two lowest rotational levels $(J, K) = (1, 1)$ and (1,0) is 32.86 K (where the temperature in kelvins is a substitute for $k_B T$, and k_B is Boltzmann's constant), and the next levels are 150 K or more above the lowest (1,1) level. Because typical kinetic temperatures in clouds outside of the Galactic Center are much lower than 150 K, not only are the excited vibrational levels of H_3^+ not populated, but the molecule is also confined almost entirely to the two lowest rotational levels of the ground vibrational state. Thus, absorption spectroscopy of vibrational transitions originating from the (1,1) and (1,0) levels of the $v = 0$ state is almost always the only means of detection. Figure 14 shows the six absorption lines connecting those levels to the $v_2 = 1$ levels. Five of the six, as well as several additional lines, which have only been detected toward the Galactic Center, can be seen in the spectrum shown in Fig. 13. The wavelengths of these six lie between 3.66 and 4.07 μm. Earth's atmosphere is relatively transparent in that wavelength interval and all six lines are accessible by spectrographs on ground-based telescopes.

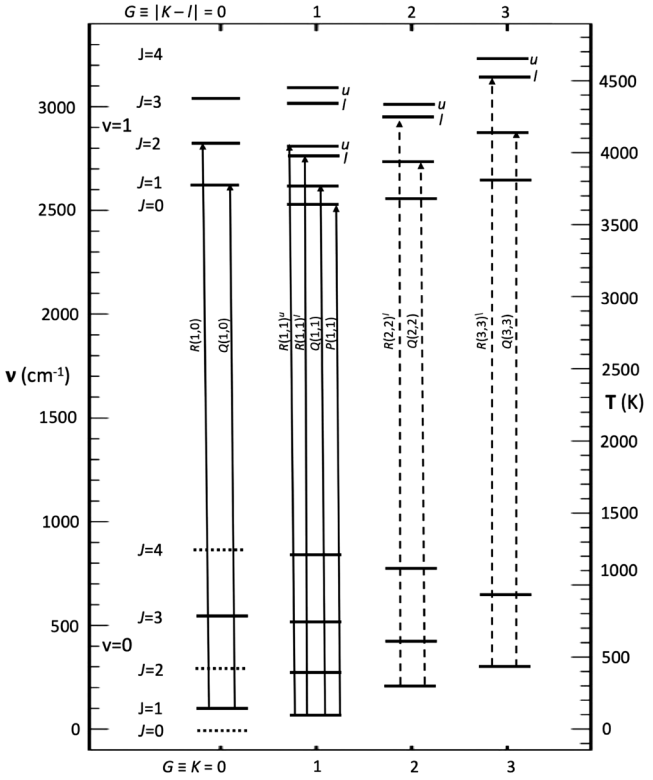

FIG. 14. Energy level diagram for the lowest rotational levels of the ground vibrational and $v_2 = 1$ states of H_3^+. Absorption lines from the $v = 0$ $(J, K) = (1, 0)$ and (1,1) levels are shown by vertical continuous lines. Four other absorption lines originating in the (2,2) and (3,3) levels, important in studies of the Galactic Center, are denoted by vertical dashed lines. The $J = 0$ and even-numbered levels of the ground vibrational state do not exist. The values of G at the bottom and top of the figure are for the ground and first excited vibrational states, respectively.

D. Predicted abundances of H_3^+

The steady state abundance of H_3^+ in a cloud can be derived by equating its production and destruction rates, which are described in Sec. IV.B. In both dense and diffuse clouds, the equation describing the steady state has the simple form

$$\zeta_{cl} n(H_2) = k_r n(r) n(H_3^+), \tag{9}$$

where ζ_{cl} is the cosmic-ray ionization rate of H_2 in the cloud, $n(r)$ is the number density of the dominant reactant with H_3^+, and k_r is the rate coefficient for that reaction. In dense clouds CO and O are the principal reactants with H_3^+. Virtually all gas-phase carbon is predicted to be in CO, with its abundance ratio relative to molecular hydrogen, $[CO]/[H_2] \sim 1.5 \times 10^{-4}$ over a wide range of conditions, and much of the gaseous

oxygen is atomic (Lee, Bettens, and Herbst, 1996). These predicted abundances, when combined with rate coefficients for the proton-hop reactions $H_3^+ + CO \rightarrow HCO^+ + H_2$ (Anicich and Huntress, 1986) and $H_3^+ + O \rightarrow OH^+ + H_2$ (Fehsenfeld, 1976), indicate that CO is responsible for approximately 75% of the destruction of H_3^+ (McCall *et al.*, 1998). In diffuse clouds the destruction of H_3^+ is virtually entirely due to DR on electrons.

Equation (9) can be rewritten as

$$n(H_3^+) = \frac{\zeta_{cl}}{k_r}\frac{n(H_2)}{n(r)}. \tag{10}$$

Thus, in both types of clouds the steady state number density of H_3^+ depends on the ratio of the number densities of H_2 and the reactant. In dense clouds $n(r) \approx 1.4n(CO)$, to include the contribution to the destruction of H_3^+ by atomic oxygen and more minor contributors, and thus $n(r)/n(H_2) \approx 2 \times 10^{-4}$. Theory and observation indicate that in diffuse clouds with total visual extinctions of at least a few magnitudes (in which H_3^+ has been frequently detected), as in dense clouds, most of the hydrogen is in molecular form (van Dishoeck and Black, 1986; Winkel *et al.*, 2017). The origin of the H_3^+-destroying electrons is the near-total single ionization of free atomic carbon in the cloud. In interstellar gas the abundance of carbon to hydrogen is $\sim 3 \times 10^{-4}$, but roughly half of the carbon is contained in dust and in carbon-bearing compounds (Sofia *et al.*, 2004; Snow and McCall, 2006). Consequently, $n(e)/n(H_2) \approx 3 \times 10^{-4}$.

From Eq. (10) it is clear that within either type of cloud $n(H_3^+)$ is a constant, i.e., independent of cloud density, as long as ζ and either $([CO] + [O])/[H_2]$ for dense clouds or $[C^+]/[H_2]$ for diffuse clouds does not vary significantly within the cloud (Geballe and Oka, 1996; Geballe *et al.*, 1999). Then the column density of H_3^+, $N(H_3^+)$, observed in the cloud is simply related to the number density by $N(H_3^+) = n(H_3^+)$, L, where $n(H_3^+)$ is a constant within the cloud and we now use L as the length of the column through the cloud to the light source, which is usually a star behind the cloud or a star in the cloud. Thus, the observed $N(H_3^+)$ acts as an approximate yardstick, allowing L to be estimated.

This linear relation for H_3^+ between column density and path length does not hold for many other species, whose densities depend linearly on the density of the cloud and whose column densities are integrals of their varying number densities through the cloud. As a simple example of the implications of this difference, two dense clouds of the same mass and identical in all other respects, except that the dimensions of one are twice that of the other, contain the same number of CO molecules, but there are 8 times as many H_3^+ ions in the larger cloud. Likewise, two dense clouds of the same dimensions but one with 10 times the particle density of the other will have column densities of CO that differ by a factor of 10, but identical column densities of H_3^+.

1. Dense clouds

For dense clouds, using the adopted cosmic-ray ionization rate of $\zeta_{dense} = 3 \times 10^{-17}$ s^{-1}, the previously mentioned value of $[CO]/[H_2]$ multipied by 1.4, and the Langevin rate coefficient for the proton-hop reaction with CO $n(H_3^+) \approx 7 \times 10^{-5}$ cm^{-3}, and thus $N(H_3^+) \approx 7 \times 10^{-5}L$. Since ζ_{dense} is somewhat uncertain, as discussed in Sec. IV.B, the previous equation might also be written as

$$\zeta_{dense}L \approx 4 \times 10^{-13}N(H_3^+), \tag{11}$$

which can be used to constrain ζ_{dense} and/or L.

Typically only a rough estimate is available for L, as the line-of-sight distance through the cloud to a source behind it or the depth of a source in the cloud is not measurable. Assuming the adopted cosmic-ray ionization rate and taking the observed column densities of H_3^+, determined from spectra such as those shown in Fig. 14, which are typically 3×10^{14} cm^{-2} (McCall *et al.*, 1999), absorption path lengths of the order of 1 pc are obtained, which are similar to the observed dimensions of the clouds on the plane of the sky. Thus, the adopted value, which previously has been based on several lines of less direct evidence unrelated to H_3^+, is consistent with the observed column densities of H_3^+ in dense clouds. In other words, the observed column densities of H_3^+ are as expected for ion-neutral chemistry, primed by H_3^+, as the dominant form of gas-phase chemistry in molecular clouds.

2. Diffuse clouds

For diffuse clouds Eq. (10) can be rewritten as

$$N(H_3^+) \approx \frac{\zeta_{diff}}{k_e}\frac{n(H_2)}{n(e)}L \approx 5 \times 10^{-6}\ \text{cm}^{-3}L, \tag{12}$$

under the assumption that all free electrons come from the nearly complete single ionization of gas-phase atomic carbon and that almost all hydrogen is in molecular form, as discussed previously. Once again, expressing $n(H_3^+)$ as $N(H_3^+)/L$ is appropriate if both ζ_{diff} and the ratio of C^+ to H_2 are constant within the cloud.

One of the initially surprising results of spectroscopy of H_3^+ in interstellar clouds was that column densities of H_3^+ are typically an order of magnitude larger than had been predicted (McCall *et al.*, 1998, 2002; Geballe *et al.*, 1999). There are various possible explanations: k_e is much smaller than thought, most carbon is neutral rather than singly ionized, diffuse clouds are much larger than thought, or the cosmic-ray ionization rate of H_2 in diffuse clouds is much greater than in dense clouds. New laboratory measurements of k_e and new astronomical observations have clearly demonstrated that the last of these possibilities is the correct explanation (McCall *et al.*, 2003; Indriolo *et al.*, 2007). The mean cosmic-ray ionization rate in diffuse clouds (outside the Galactic Center) is 3.5×10^{-16} s^{-1} (Indriolo and McCall, 2012), an order of magnitude greater than the canonical value for dense clouds. There also appear to be large variations in ζ_{diff} from cloud to cloud, differing from the mean in some cases by a factor of 3. These seem to be unrelated to large-scale Galactic parameters and are discussed further in Sec. IV.F.2.

Two possibilities have been suggested to explain the large difference between the values of ζ in dense and diffuse clouds.

One of them, proposed by Skilling and Strong (1976) and Padoan and Scalo (2005) is that the cosmic rays that are efficient at ionizing H_2 are confined in lower density clouds by self-generated Alfvén waves. Padoan and Scalo showed that the cosmic-ray density scales as the square root of the ion density. Such a dependency would result in a higher cosmic-ray ionization rate in diffuse clouds.

The other explanation for the different values of ζ is the existence of a large population of low-energy (1–10 MeV) cosmic rays that can penetrate diffuse clouds but whose energy is exhausted on the surfaces of dense clouds. The ionization cross section of cosmic rays with energies E less than 100 MeV is proportional to E^{-1} (Cravens and Dalgarno, 1978), and thus the penetration distance of a cosmic ray into a constant density cloud is proportional to E^2. Little is known about the spectrum of low-energy cosmic rays, which are deflected by the solar magnetic field and cannot be observed from Earth. Possible cosmic-ray spectra that could account for the difference in cosmic-ray ionization rates between dense and diffuse clouds were explored by Indriolo, Fields, and McCall (2009).

Figure 15 shows the number densities in an interstellar cloud of H_3^+, H_2, H, CO, and C^+ as a function of the number density $n(\mathrm{H})$ of a cloud, assuming the adopted value of ζ in dense clouds and its mean measured value in diffuse clouds. The figure illustrates the difference in behavior of H_3^+ and other species (including many not shown in the figure), whose densities scale with the cloud density. In contrast, $n(H_3^+)$ is independent of density within each type of cloud, but with a typical value in diffuse clouds roughly an order of magnitude less than in dense clouds. Because the dimensions of diffuse clouds in which H_3^+ has been detected are typically much greater than those of dense clouds, the column densities of H_3^+ are similar in the two cloud types. This would not be the situation if ζ were the same in both cloud types.

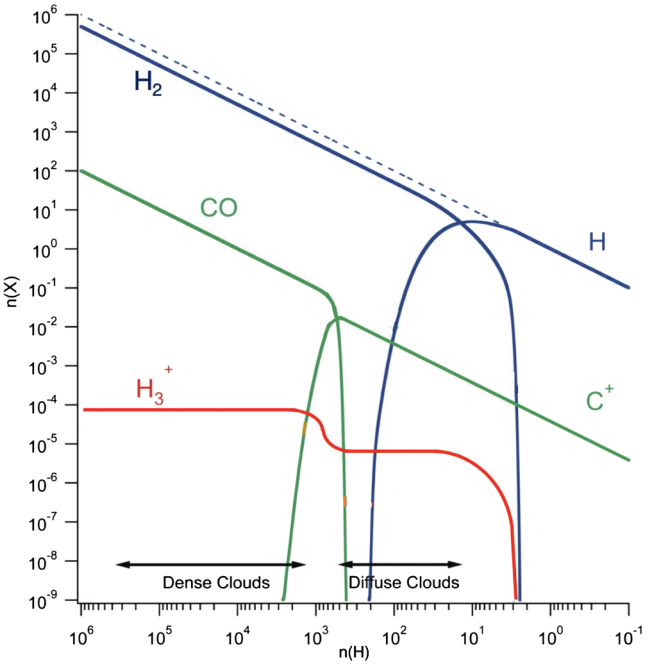

FIG. 15. Number densities $n(X)$ of H_2, CO, C^+, and H_3^+ in dense clouds and in diffuse clouds with visual extinctions > 1 magnitude as a function of cloud density $n(\mathrm{H})$. The dashed line shows the density of hydrogen atoms. Adapted from Oka, 2006.

The roughly 100-fold difference in the dominant rate coefficients for destruction of H_3^+ in diffuse and dense clouds is balanced by the roughly 100-fold difference between the densities of electrons in diffuse clouds and CO in dense clouds. Consequently, the lifetime of an H_3^+ ion in each type of cloud is roughly the same ($\sim$10 yr).

E. Physics of the low-lying rotational levels

To understand how spectroscopy of H_3^+ can quantitatively reveal some of the basic properties of interstellar clouds, it is necessary to examine the energy level structure of its low-lying rotational levels and the selection rules governing radiative transitions between them. Those characteristics of H_3^+ together with the gas density and temperature determine the relative strengths of the observed IR rovibrational lines. Conversely, the measured relative strengths of the absorption lines originating in those levels constrain the derived physical conditions in the interstellar clouds. The characteristics of these levels are especially important in interpreting the spectra of H_3^+ in diffuse clouds.

Figure 16 shows the low-lying rotational levels of the ground vibrational state along with the possible radiative transitions between them. Some pure rotational transitions are weakly allowed (see Sec. V.C). The allowed transitions are restricted to those with $\Delta J = 0$ or ± 1 that connect either two *ortho* levels of different K ($\Delta K = \pm 3$) or two *para* levels of different K ($\Delta K = \pm 1$). The radiative lifetimes of all but the two transitions connecting the three lowest levels of *para* H_3^+ are of the order of 10 h. In contrast, the lifetimes of the two levels $(J, K) = (2, 1)$ and (2,2) are several weeks.

The most common collision partner of H_3^+ in both dense and diffuse clouds is H_2. Although radiative transitions of H_3^+ preserve nuclear spin, a collision of H_3^+ with H_2, while resulting in the same two species, can result in a change of spin state for H_3^+ if the proton hops from the H_3^+ to the H_2; see, e.g., Hugo, Asvany, and Schlemmer (2009). Such collisions tend to push the relative populations of the lower levels of H_3^+ toward thermal equilibrium. In dense clouds collision times are of the order of days and are much more frequent than the radiative lifetimes of the (2,1) and (2,2) levels. There the low temperatures maintain virtually all of the H_3^+ in the lowest *ortho* (1,0) and *para* (1,1) levels. Any H_3^+ in dense clouds that is excited to the (2,1) and (2,2) levels by collisions is quickly collisionally deexcited to either (1,0) or (1,1). The ratio of the column densities in the (1,0) and (1,1) levels, which can be determined by measuring the strengths of individual rovibrational lines originating in those levels, thus acts as a thermometer, as elaborated on later, accurately reflecting the kinetic temperature of the dense cloud.

The situation is different in diffuse clouds. Collision times between H_3^+ and H_2 there are comparable to the radiative lifetimes of the $J = 2$ levels of *para* H_3^+ at the critical density of roughly 200 cm^{-3}. As illustrated in Fig. 16, a radiative

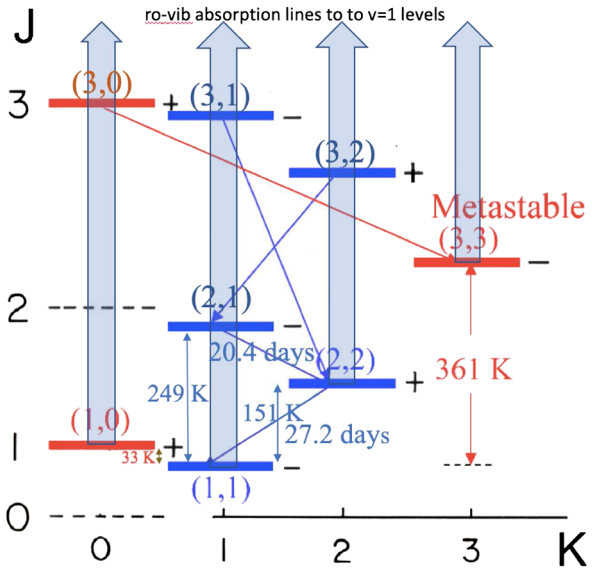

FIG. 16. Levels of H_3^+ for the lowest three rotational states of its ground vibrational state. Thick upward arrows denote IR absorption lines to $v = 1$ levels. Thin diagonal lines are allowed spontaneous radiative transitions between *ortho* (red) and *para* (blue) levels. Energies of the four lowest levels above the (1,1) state and radiative lifetimes of the $J = 2$ states are shown. From Geballe, Oka, and Goto, 2019.

pathway exists from low-lying rotational states to the ground *para* state, but not to the ground *ortho* state. Oka and Epp (2004) showed that as a result collisions of H_3^+ with H_2 transfer H_3^+ from the (1,0) to the (1,1) level, resulting in their level populations being out of thermal equilibrium. The observed *ortho-to-para* ratios in diffuse clouds are discussed in Sec. IV.F.2.

F. Analysis of spectroscopy of H_3^+ in the Galaxy's dense and diffuse clouds

Lines of H_3^+ have now been detected in a large number of dense clouds (Geballe and Oka, 1996; McCall *et al.*, 1999; Brittain *et al.*, 2004; Gibb *et al.*, 2010; Goto, Geballe, and Usuda, 2015; Goto *et al.*, 2019) and diffuse clouds (McCall *et al.*, 1998, 2002, 2003; Geballe *et al.*, 1999; ; Indriolo *et al.*, 2007, 2010; Gibb *et al.*, 2010; Crabtree *et al.*, 2011; Indriolo and McCall, 2012; Albertsson *et al.*, 2014) in the spiral arms of the Milky Way;.

The strength of an absorption line is quantitatively described by its equivalent width W_λ, whose units are wavelength and whose value corresponds to the fractional absorption integrated across the line. If the absorption line is weak, as is always the case for interstellar H_3^+, W_λ is linearly related to the column density in the absorbing level $N_{\rm level}$ by

$$N_{\rm level}(H_3^+) = \frac{3hc}{8\pi^3\mu^2} W_\lambda, \tag{13}$$

where N is in $\rm cm^{-2}$ and $\mu \sim 0.1$ D for the 3.5–4.1 μm lines of H_3^+ shown in Fig. 13; see Oka (2013), Table 2 for details.

The difference in energy between the lowest *ortho* and *para* levels is 32.86 K. In a dense cloud the ratio of the observed column densities in those levels is related to the kinetic temperature T by

$$\frac{N(1,0)}{N(1,1)} = 2e^{-32.86/T}, \tag{14}$$

where the factor of 2 comes from the ratio of the statistical weights of the two levels. Apart from clouds within approximately 150 pc of the Galactic Center, lines from these two levels are the only ones detected, making analysis particularly straightforward compared to analyses based on other molecular species with many populated energy levels.

Unlike H_3^+, most molecules in clouds are observed at radio and millimeter wavelengths via their rotational emission lines. Because the line emission originates in a column passing through the entire cloud, interpretation of emission spectra can be problematic because of (1) uncertainty in assigning portions of the velocity profile of the emission to the front or rear of the cloud, (2) radiative transfer effects such as self-absorption by molecules located in the foreground portion of the cloud, which alter the line profile, and (3) the large beam diameters associated with single dish radio telescopes. However, millimeter line emission usually occurs over a large portion of the cloud, and thus lines can be observed over most or all of the cloud.

IR absorption spectroscopy also has severe limitations, in particular, for H_3^+. Because absorption lines of H_3^+ are both weak and frequently narrow, sensitive high-resolution spectroscopy toward bright background sources is usually a requirement. In addition, suitable background sources (usually stars) must possess few or no intrinsic spectral features near the wavelengths of the weak H_3^+ lines that could obscure the weak lines. In practice these constraints limit both the number of sight lines within a cloud that can be observed and the number of clouds that can be investigated. Moreover, absorption spectroscopy of a background star samples only a narrow column of gas, meaning that the vast majority of the cloud is unobserved. However, absorption spectroscopy has a strong advantage over emission spectroscopy in that it is known that the absorbing column lies in front of the star. Thus, there is no ambiguity about the direction of the gas motion relative to the star. This is of particular importance in interpreting complex line profiles such as those presented in Sec. IV.G.

1. Dense clouds

As pointed out previously, measurements of only two spectral lines, one from $(J, K) = (1, 1)$ and one from (1,0), are needed to determine the H_3^+ column density and the gas kinetic temperature. Column densities of H_3^+ derived in this way are typically $(1–5) \times 10^{14}$ $\rm cm^{-2}$, and cloud temperatures range from 25 to 50 K (McCall *et al.*, 1999). Because the H_3^+ lines are weak, the accuracies with which these can be determined are usually limited by telescope size and instrumental sensitivity.

Particle densities in dense clouds cannot be constrained by measurements of H_3^+ alone. However, the observed column

density of CO, its abundance relative to H_2 [1.5×10^{-4} (Lee, Bettens, and Herbst, 1996)], and the path length L determined by the measurement of the H_3^+ column density (Sec. IV.D.1) can be combined to obtain an estimate of the mean density of the cloud. This technique was employed successfully by McCall *et al.* (1999), using absorption spectroscopy of lines of the first overtone band of CO toward the same background source for which spectra of H_3^+ were obtained. The cloud densities obtained range from 10^4 to 10^5 cm^{-3}. Such high mean densities imply that most of the gas associated with the absorbing H_3^+ and CO is located in dense cloud cores. Assuming that each background source is located at the center of its cloud and taking the length of the absorbing column as the radius of the cloud, the masses of the clouds are hundreds to thousands of Suns. It is expected that star formation would be proceeding or imminent within dense clouds of such masses. In fact, the background continuum sources toward which the absorption lines were measured are in all cases known to be massive young stars embedded in the clouds and in their final stages of formation.

2. Diffuse clouds in spiral arms

Since the discovery of much higher than expected abundances of H_3^+ in diffuse clouds, several studies of H_3^+ in diffuse clouds have been reported, as referenced previously. These both verified that much higher values of ζ are prevalent in diffuse clouds than in dense clouds and demonstrated that a wide range of values of ζ in diffuse clouds is required to account for the observations. This could suggest that local variations in the cosmic-ray spectrum exist, perhaps associated with local sources of cosmic rays (Indriolo, Fields, and McCall, 2009; Indriolo *et al.*, 2010; Indriolo and McCall, 2012), or that the different values are caused by variations in cloud properties (e.g., in the fraction of hydrogen in H_2 and/or fraction of carbon bound in molecules and dust).

A third interesting result of these studies is the discovery that for many diffuse clouds the excitation temperature of H_3^+, as determined by the ratios of the strengths of lines from the lowest *ortho* and *para* levels [see, e.g., McCall *et al.* (2002), Indriolo *et al.* (2007), and Albertsson *et al.* (2014)], are significantly lower than that found for the two lowest *ortho* and *para* levels of H_2 from UV spectroscopy (Rachford *et al.*, 2002, 2009). Because the samples of diffuse clouds for which observations of these two molecules were obtained only slightly overlap, there is some uncertainty in this conclusion. However, the samples are each extensive enough and the temperature difference (a few tens of kelvins) large enough [toward four of the five clouds where the samples overlap (Albertsson *et al.*, 2014)] that the difference is likely to be real. It is generally thought that the H_2 excitation temperature closely approximates the true kinetic temperature of the gas due to frequent inelastic collisions of H_2 with free protons in the cloud (Crabtree *et al.*, 2011; Albertsson *et al.*, 2014), and therefore that it is the (1,1) and (1,0) level populations of H_3^+ in diffuse clouds that are not in thermal equilibrium.

Several mechanisms have been proposed to explain the temperature differences. The most natural of these is the one described by Oka and Epp (2004) that was discussed earlier, in which in low-density gas the (1,1) level is overpopulated by radiative transitions from the $J = 2$ levels, both of which are *para* levels that can be collisionally populated by collisions of H_2 with H_3^+ in either the lowest *ortho* or the lowest *para* state; see Fig. 16. Oka and Epp (2004) used detailed balance to estimate the magnitude of the effect; see their Fig. 6. For low-temperature diffuse clouds such as those in spiral arms, they calculate temperature differences that are smaller than those observed. A more detailed calculation using selection rules might give better agreement.

Laboratory experiments by Grussie *et al.* (2012) in which H_3^+ and H_2 were collided at low temperatures indicate that, as theoretically expected, the collisions tend to thermalize the H_3^+. They, as well as Crabtree *et al.* (2011), note that because the dominant formation mechanism for H_3^+ is the ion-neutral reaction between H_2^+ and H_2, both of which are mainly in the lowest-lying *para* state at cloud temperatures, their reaction favors forming H_3^+ in the *para* (1,1) state. They suggest that the low H_3^+ excitation temperature could be explained if subsequent collisions of the newly formed H_3^+ with H_2 do not occur frequently enough to thermalize its population before the H_3^+ undergoes DR. However, during the ~10 yr lifetime of a H_3^+ molecule in a diffuse cloud of particle density 10^2 cm^{-2} an individual H_3^+ molecule is expected to undergo ~100 or more collisions with H_2, which should be more than sufficient to thermalize the population. Albertsson *et al.* (2014) suggested that the low H_3^+ excitation temperature in diffuse clouds can be explained if the DR of H_3^+ is 5 times more rapid for the (1,0) level than for the (1,1) level. However, calculations by dos Santos, Kokoouline, and Greene, 2007 suggested the opposite tendency. Thus, a detailed explanation for the observed temperature differences remains to be found.

G. Galactic Center

The location where observations of H_3^+ have had the greatest impact on our understanding of the interstellar gaseous environment is the innermost region of the Milky Way, 8 kpc from the Sun, known as the Central Molecular Zone (CMZ) (Morris and Serabyn, 1996). Spectra of H_3^+ there have revealed the existence of a vast amount of warm, low-density gas, which was hardly recognized prior to observations of H_3^+ but which appears to take up most of the volume of the CMZ. This gas is undergoing rapid radial expansion and appears to be related to a violent event or series of events that may have taken place at or near the center of the CMZ roughly 10^6 yr ago, evidence for which (unrelated to H_3^+) has been seen at the outer edge of the CMZ and well beyond it.

The CMZ, a disklike region of diameter ~300 pc and thickness ~50 pc, contains a central supermassive black hole (SMBH), Sgr A* of mass $\sim 4 \times 10^6$ $M_\odot$, currently in a quiescent phase, accreting minimally compared to SMBHs in many external galaxies. The CMZ also contains the Galaxy's densest concentration of stars, which is centered around Sgr A*; at least six giant molecular clouds, some of which are currently undergoing star formation; three clusters of hot, massive, and luminous stars that apparently formed near Sgr A* several million years ago; a disk of dense

molecular gas orbiting Sgr A* at a distance of 2 pc; and a host of other energetic phenomena.

The view from the Sun toward the Galactic Center is blocked at optical wavelengths but only partially obscured at IR wavelengths by dust associated with the gas in the spiral arms lying between the Sun and the Center. Fortuitously, none of the Galactic Center's giant molecular clouds, whose associated dust could add significantly to the IR obscuration, lies directly in front of the central part of the CMZ as viewed from the Sun, and our IR view toward the many fascinating objects within that region is minimally affected by them.

1. Early spectra

Figure 17 shows the discovery spectrum of H_3^+ in the Galactic Center. In it the spectrum of the close pair of H_3^+ absorption lines from the two $J = 1$ levels toward a bright star less than 0.3 pc in projected distance from Sgr A* (Geballe and Oka, 1996) is compared to spectra of the same pair of lines in a typical dense cloud and in a diffuse cloud, each located in a spiral arm of the Galaxy far from the Center. The contrast between the column densities of H_3^+ toward the CMZ and in the other two environments is great. The equivalent width of the absorption originating in the CMZ is roughly 20 times that of the other two, implying ∼20 times higher column densities in the two $J = 1$ levels. This is remarkable because, compared to the lines of sight to the stars in the dense and diffuse clouds, the line of sight to the star in the CMZ contains roughly only one-third as much gas and 3 times as much gas, respectively. In addition to the differences in line strengths, the H_3^+ absorption in the CMZ is broad, occurring over a much wider range of velocities than the absorptions in the two clouds.

Figure 18 shows subsequent higher resolution and higher sensitivity spectra of three lines of H_3^+, from the (1,1), (2,2), and (3,3) levels, and one line of the overtone vibrational band of CO, toward a bright star located 30 pc from the SMBH and thus fairly close to the center of the CMZ. Note that the (3,3) level is metastable; it cannot radiatively decay (Fig. 16). Note also that unlike the lines shown in Fig. 17, the line of H_3^+ from the (1,1) level shown in Fig. 18, the $R(1,1)^l$ line, is not blended with another line of H_3^+. The velocity profiles of the lines consist of various combinations of three sharp absorptions and a broad wedge-shaped absorption. The sharp absorptions are readily identifiable as characteristic of the gas in the three spiral arms of the Galaxy that are located between the CMZ and the solar neighborhood. The broad absorption features are produced by H_3^+ within the CMZ.

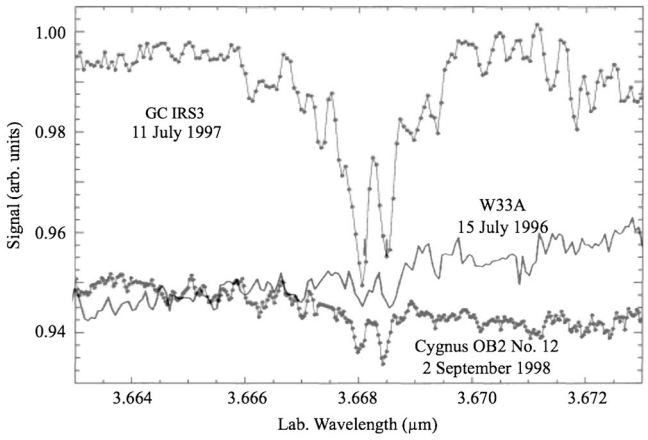

FIG. 17. Discovery spectrum of H_3^+ toward Galactic Center source IRS3 (Geballe *et al.*, 1999), compared with spectra of the same two lines toward a bright protostar in the dense cloud W33A (Geballe and Oka, 1996) and the star Cygnus OB2 No. 12, located in a diffuse cloud (Geballe, 2000). Note the much stronger absorption toward the star in the Galactic Center than toward the other stars. All three spectra were obtained at UKIRT. From Geballe, Oka, and Goto, 2019.

Together these lines reveal several distinguishing characteristics of the CMZ's gas, as elucidated by Oka *et al.* (2005). First, the gas responsible for the broad absorption is much warmer than the gas in clouds residing in spiral arms: warm enough that the $(J, K) = (3, 3)$ level, which lies 361 K above the lowest-lying (1,1) level (see Fig. 16), is significantly populated (Goto *et al.*, 2002) and produces a readily detectable absorption line. To date the CMZ is the only location for which absorption originating in this level has been detected; see Fig. 13 for another example. Because the (3,3) level has no

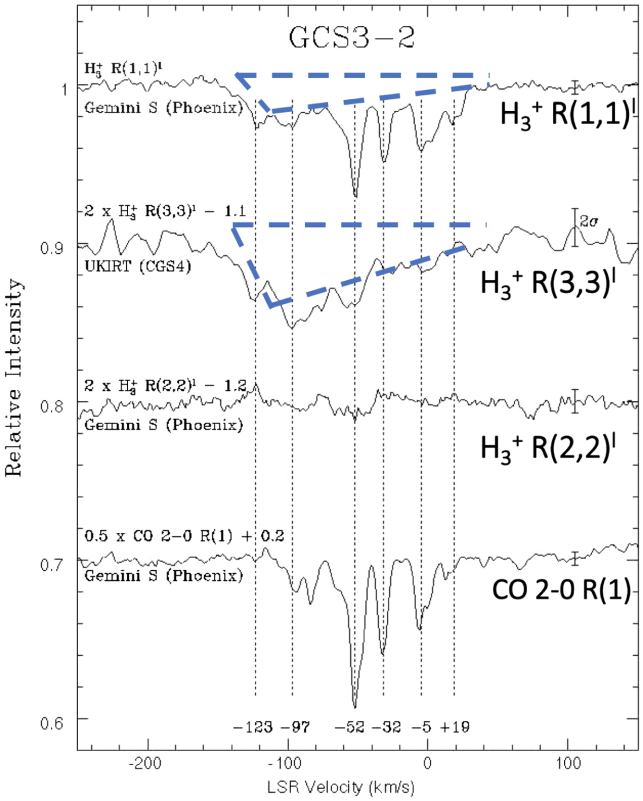

FIG. 18. Velocity profiles of three lines of H_3^+ and one line from the first overtone band of CO toward a bright IR star in the Quintuplet Cluster, near the center of the CMZ, obtained using the Gemini South Telescope and UKIRT at resolving powers of 50 000 and 37 000, respectively. The intensities of the spectra are scaled by different factors as indicated. The thick dashed lines delineate wedges of blueshifted absorption, present in the upper two spectra but absent in the lower two. The narrow vertical dashed lines mark the radial velocities of dense gas in foreground spiral arms. The velocity scale is relative to the local standard of rest (LSR). Adapted from Oka *et al.*, 2005.

radiative pathway to lower energy states, its population is in thermal equilibrium with its surroundings and, together with the (1,0) and (1,1) levels, serves as a thermometer for the gas. The relative strengths of the absorption lines from these levels yields a temperature of ~200 K for the gas in which the H_3^+ is found. This temperature appears to be roughly constant over the entire velocity range of the absorption.

A second important characteristic seen in Fig. 18 is the absence of absorption by H_3^+ in the (2,2) level, which is only 151 K above the lowest *para* level and well below the (3,3) level; see Fig. 16. Were the population of this level also in thermal equilibrium, absorption lines from $v = 0, J = 2$ levels would be easily detected. The absence of absorption in the $R(2,2)^l$ line thus implies that the density of the warm CMZ gas is well below the critical density for that level of 200 cm^{-3}.

Spectroscopy of low J lines of the first overtone vibrational band of CO near 2.35 μm, such as the one shown in Fig. 18, has also proven to be invaluable in interpreting the spectra of H_3^+. The absence of the broad absorption wedge in the spectrum of the CO 2-0 $R(1)$ line, whose lower energy level is only 5.5 K above ground, confirms that the CMZ gas is in a low-density environment in which CO is nearly entirely photodissociated. CO is abundant, however, in the cold dense clouds found in spiral arms well outside of the Galactic Center. There its low-lying overtone lines produce sharp absorption features at the characteristic radial velocities of the spiral arms, easily seen in Fig. 18 and closely matching the sharp features in H_3^+ line from the lowest (1,1) level.

Third, the vast majority of the broad absorption by H_3^+ in the warm diffuse gas is blueshifted, implying that the radial component of the gas velocity (i.e., the component perpendicular to the plane of the sky) is toward the Sun at a wide range of speeds. Both the large column density of H_3^+ and the wide range of radial velocities suggest that the column of warm low-density gas is long, with its length an appreciable fraction of the radius of the CMZ (Oka *et al.*, 2005). The highest negative velocities in H_3^+, -150 km s^{-1}, are approximately those of the front surface of a rapidly expanding ring of molecular gas [commonly referred to as the Expanding Molecular Ring (EMR)] located at the outer edge of the CMZ, observed at radio wavelengths in lines of OH (Kaifu, Kato, and Iguchi, 1972), H_2CO (Scoville, 1972), and H (Kaifu, Iguchi, and Kato, 1974). This correspondence suggests that the outward-moving CMZ gas and the EMR are physically associated with one another.

2. Recent spectra

The data described in Sec. IV.G.1 date from 2003 and earlier. Spectra obtained up until 2008 on sight lines to other bright stars in the central region of the CMZ, covering approximately 10% of its full 300 pc extent, also found large quantities of warm, low-density, and outward-moving gas (Goto *et al.*, 2008). Since then spectra of H_3^+ and CO have been obtained toward roughly 30 bright IR stars within the CMZ, extending nearly from one edge of it to the other (Geballe and Oka, 2010; Oka *et al.*, 2019). These stars were selected to have nearly featureless intrinsic spectra (Geballe *et al.*, 2019), like those of the stars in Figs. 13 and 18, so that the absorption lines of interstellar H_3^+ and CO are not seriously contaminated by lines in the photospheres of the stars.

The spectra of nearly all of these stars contain absorption lines by H_3^+ located in warm and diffuse gas, as evidenced both by absorption in the $R(1,1)^l$ and $R(3,3)^l$ lines and by the absence of absorption by lines of the CO overtone band at the velocities of the $R(3,3)^l$ absorption, similar to Fig. 18. The velocity profiles of the warm H_3^+ show a clear tendency to become narrower and less blueshifted with increasing distance on the sky from the center of the CMZ, with only narrow absorptions near zero Doppler shift observed close to the eastern and western edges (Oka *et al.*, 2019).

This trend is most simply interpreted as due to radial expansion of the warm diffuse gas from a position or region near the center of the CMZ. It also implies little or no rotation of the gas about the center. Although both the front and rear of the EMR are observed at radio wavelengths (i.e., both highly blueshifted and highly redshifted line emission from it are detected), no highly redshifted H_3^+ has been observed. This is probably a selection effect, resulting from the necessity of observing toward bright background stars and the likelihood that stars in the rear half of the CMZ are more heavily obscured by dust within the CMZ and thus significantly fainter than background stars observed to date.

3. Analysis and interpretation

As described in Sec. IV.D, it is fairly straightforward to estimate the number density of H_3^+ and the cosmic-ray ionization rate in diffuse clouds outside of the Galactic Center from the observed absorption strengths of lines of H_3^+. Using the simple steady state analysis of Sec. IV.D.2 led to values of ζ in the warm diffuse gas of the CMZ that are an order of magnitude higher than in colder diffuse clouds in the spiral arms (Oka *et al.*, 2005). However, in the harsh environment of the CMZ the creation and destruction of H_3^+ in its diffuse gas are more complex processes than in external diffuse clouds, which significantly complicates the analysis.

In the CMZ atomic hydrogen is likely to be as or more abundant than H_2 in the CMZ, resulting in significant competition between the ion-molecule reaction that creates H_3^+ from collisions between H_2^+ and H_2 and the charge-exchange reaction between H_2^+ and H that electrically neutralizes the H_2^+ before it reacts with H_2 to form H_3^+. In addition, free electrons, the principle destroyer of H_3^+, are available not only from the ionization of carbon by UV radiation but also from the ionization of atomic hydrogen by cosmic rays. Both of these phenomena greatly reduce the abundance of H_3^+ and require considerably higher values of ζL than derived by Oka *et al.* (2005) to account for the observed column densities of H_3^+.

Oka *et al.* (2019) found that the most likely values of ζ and L in the CMZ are approximately 2×10^{-14} s^{-1} and 100 pc, respectively. The former, which is nearly 2 orders of magnitude higher than in Galactic diffuse clouds and 3 orders of magnitude higher than in Galactic dense clouds, is almost unprecedented outside of the Galactic Center but is broadly

consistent with values of ζ derived by Yusef-Zadeh *et al.* (2007, 2013), Indriolo *et al.* (2015), and Le Petit *et al.* (2016) for the CMZ. The most likely value of L implies that the warm diffuse gas has a filling factor of $\sim 2/3$, which would make it by far the most voluminous gaseous environment in the CMZ.

The average number densities estimated by Oka *et al.* (2019) for the warm diffuse gas are $n(\mathrm{H}) \approx 30$, $n(\mathrm{H_2}) \approx 20$, $n(\mathrm{H_3^+}) \approx 1 \times 10^{-5}$, and $n(\mathrm{H^+}) \approx n_e \approx 0.3\ \mathrm{cm^{-3}}$. This composition is quite different from that of the cold diffuse gas found in spiral arms far from the Galactic Center, although the mean density of H_3^+ is similar to its density in diffuse clouds in Galactic spiral arms; see Fig. 15. Finally, it must be noted that although the CMZ takes up a miniscule fraction ($\sim$0.000 01) of the volume of the Milky Way, the amount of H_3^+ that it contains $\sim 2.5\ M_\odot$ greatly exceeds the amount in the rest of the Galaxy.

Assuming that the diffuse gas in the rear half of the CMZ has similar properties to that observed in the front half, the mass of the warm diffuse expanding gas is approximately $6 \times 10^6\ M_\odot$. Its radial momentum is $\sim 3 \times 10^8\ M_\odot\ \mathrm{km\ s^{-1}}$, an amount comparable to that generated by 10 000 core collapse supernovae. A characteristic time for the expansion, obtained by dividing the radius of the CMZ by the average expansion velocity $\sim 75\ \mathrm{km\ s^{-1}}$, is $\sim 2 \times 10^6$ yr. To maintain the currently state requires $\sim 2\ M_\odot$ of gas to be injected into the CMZ per year (perhaps by stellar winds) and a mechanism for driving it to the outer edge of the CMZ.

Alternatively, as discussed by Geballe, Oka, and Goto (2019), the radially expanding gas may have been produced by one or more explosive events in the last several million years occurring near or at the exact center of the Galaxy and possibly associated with the SMBH Sgr A*. Similar scenarios have been invoked by others to account for the EMR itself (Scoville, 1972; Kaifu, Iguchi, and Kato, 1974) and for other energetic phenomena such as the "Fermi bubbles" of gamma ray emission that are centered on the Galactic nucleus and extend several kiloparsecs above and below the Galactic plane (Su, Slatyer, and Finkbeiner, 2010).

Estimates of the age of the Fermi bubbles, which are greatly model dependent, range from 10^6 yr to a few tens of millions of years (Mou, Sun, and Xie, 2018; Yang, Ruszkowski, and Zweibel, 2018). Thus, it is uncertain if the creation of the Fermi bubbles is associated with the event or series of events that produced the EMR and the radially expanding gas in the CMZ. Geballe, Oka, and Goto (2019) estimated that if gravity from the enclosed mass of the Galaxy is the dominant force acting on the warm diffuse gas, the radial expansion of that gas should end within the next $\sim 1 \times 10^6$ yr and infall should begin. This could result after an additional $\sim 1 \times 10^6$ yr in new episodes of star formation and in explosive events associated with gas accreting onto Sgr A*.

H. Isotopomers of H_3^+

Deuterium was created roughly 20 min after the big bang. Almost all of it fused at that time to form ^{4}He, leaving only a trace deuterium abundance of 2.6×10^{-5} relative to hydrogen. Since then it is estimated that in the local ISM there has been a 10% decrease in the abundance of D due to nuclear burning of it in stars (Linsky *et al.*, 2006; Weinberg, 2017). Just as most hydrogen in interstellar clouds in is the form of H_2, most of the deuterium in interstellar clouds is in the form of hydrogen deuteride HD.

In cold ($T < 30$ K) and dense interstellar clouds, the lower zero point energies of deuterated molecules cause chemical reaction rates to enhance the abundances of them relative to nondeuterated molecules of the same species, a process known as fractionation. The starting point for this is usually the exothermic ion-molecule reaction $\mathrm{H_3^+ + D \rightarrow H_2D^+ + H_2 + 230\ K}$, where 230 K specifies the exothermicity of the reaction. This reaction runs forward at temperatures of less than 30 K. At higher temperatures the reaction runs in the opposite direction because of the overwhelmingly larger abundance of H_2 than H_2D^+. Reactions with D_2, and D may also contribute to the production of H_2D^+ (Albertsson *et al.*, 2013), but these species are considerably less abundant than HD in cold clouds. In addition, recent laboratory measurements by Hillenbrand *et al.* (2019) found a barrier to the reaction $\mathrm{H_3^+ + D \rightarrow H_2D^+ + H}$ that will impede it at cloud temperatures.

At low temperatures further reactions of H_2D^+ with HD favor the production of D_2H^+ and then D_3^+ (Roberts, Herbst, and Millar, 2003; Flower, Pineau des Forêts, and Walmsley, 2004). Because CO and O, the principal destroyers of all three of these molecular ions, are mostly frozen on grains in the coldest clouds, the lifetimes of H_3^+ and its isotopomers in cold clouds are considerably longer than in warmer clouds and more of the deuterium-bearing isotopomers of H_3^+ are produced.

In addition to the increased abundances of H_2D^+, D_2H^+, and D_3^+, fractionation occurs in other deuterium-bearing molecules as the isotopomers of H_3^+ transfer their deuterium to neutral species. Perhaps the most extreme observed examples of this are the triply deuterated species of ammonia and methanol ND_3 and CD_3OH found in three cold clouds (Lis *et al.*, 2002; van der Tak *et al.*, 2002; Parise *et al.*, 2004).

Unlike H_3^+, both H_2D^+ and D_2H^+ possess permanent electric dipole moments. Rotational transitions of both have been detected in emission at millimeter wavelengths in cold dense clouds (Stark, van der Tak, and van Dishoeck, 1999; Caselli *et al.*, 2003; Vastel, Phillips, and Yoshida, 2004). More recent spectra of them are shown in Fig. 19. Models of the evolution of clouds show that the relative abundance of *ortho* and *para* H_2D^+, both of which have observable lines, changes with the age of the cloud core, as *ortho* H_2D^+ is slowly converted to *para* H_2D^+ via collisions with *ortho* H_2 (the dominant form of H_2 in cold clouds due to its 3 times higher production rate than *para* H_2 on dust grains and its slow thermalization in the gas phase). Thus, the *ortho*- to *para*-H_2D^+ line ratio can act as a chemical clock that measures the age of a cold cloud core (Brünken *et al.*, 2014), an important constraint for understanding star formation.

D_3^+ has a similar equilateral triangular structure as H_3^+, which requires that it be detected via its IR rovibrational band. It is expected that it too will be abundant in the coldest dense clouds (Harju *et al.*, 2017). A few attempts have been made to detect D_3^+ and IR lines of the vibrational bands of H_2D^+ and D_2H^+ (Roueff *et al.*, 2006; Goto *et al.*, 2019), and it is clear

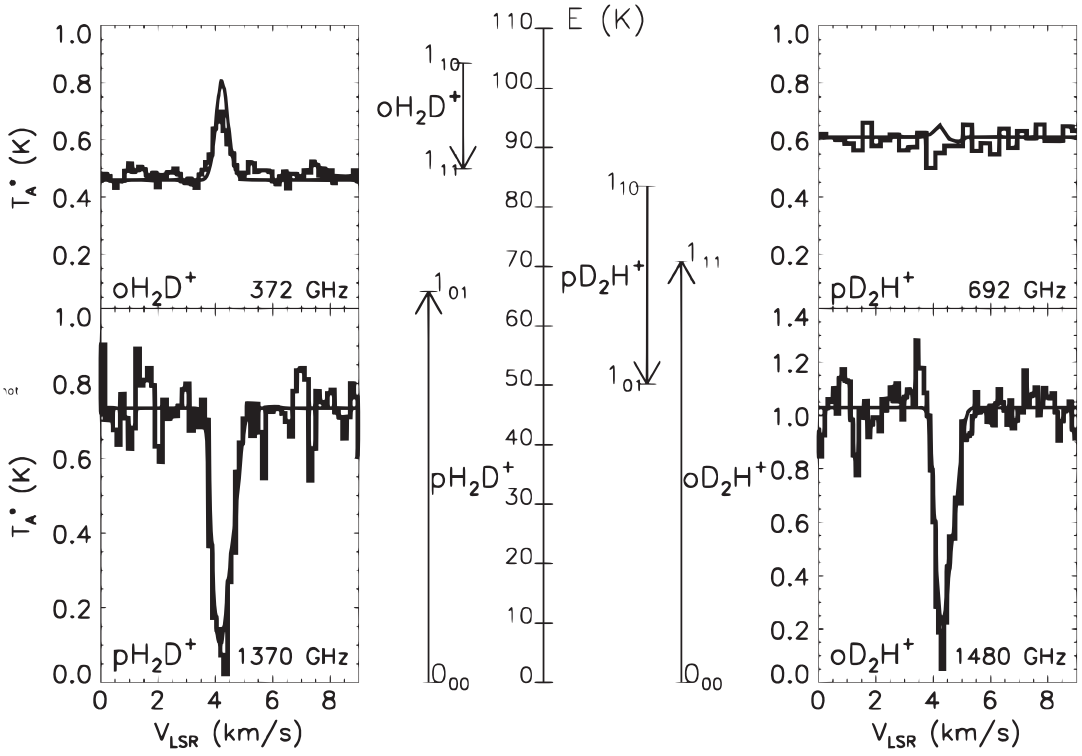

FIG. 19. Spectra of lines of *ortho* H_2D^+, *para* H_2D^+, *para* D_2H^+, and *ortho* D_2H^+ in the cold dense cloud IRAS 16293-2422. The rotational energy levels (e.g., 1_{10}) are specified by the three quantum numbers J, K_a, and K_c (Mizus *et al.*, 2017). The black histograms are observed spectra obtained by Brünken *et al.* (2014) and Harju *et al.* (2017). The solid lines are model spectra. The four transitions are shown schematically in the center of the figure and their frequencies are shown below each spectrum. The velocity scale is relative to the LSR. From Caselli, Sipilä, and Harju, 2019.

that detection poses severe challenges. The IR sources within or behind the densest and coldest clouds are faint. In addition, the wavelengths of some of the strongest lines of the isotopomers are poorly transmitted by Earth's atmosphere. It is hoped that the next generation of large ground-based and space-based telescopes will be able to overcome those difficulties and allow the abundances of H_3^+ and all three of its deuterated species to be measured on the same sight lines.

V. H_3^+ IN OTHER ASTROPHYSICAL ENVIRONMENTS

A. Extragalactic H_3^+

Spectroscopy of H_3^+ in external galaxies is potentially an important tool for studying interstellar gaseous environments beyond the Milky Way. This subfield is in its infancy and naturally is much more challenging than spectroscopy of interstellar clouds within our Galaxy because the background sources in distant galaxies are much fainter. It is likely to become a fruitful field in the next decade with the advent of the James Webb Space Telescope and the completion of ground-based telescopes much larger than the ones presently available.

In particular, the discovery of a large amount of H_3^+ toward the center of the Galaxy, as described previously, suggests that it might be possible to observe H_3^+ toward the nuclei of suitable external galaxies, those with sufficiently bright and compact sources of IR continuum radiation and large column densities of interstellar molecular gas along their lines of sight. To date spectroscopy of two such galaxies have yielded detections.

The detection of absorption lines of H_3^+ in one of these galaxies, IRAS 08572+3915, which is receding from the Sun at 6% of the speed of light and, at IR wavelengths, is probably the most luminous galaxy in the local Universe, was reported by Geballe *et al.* (2006) and is shown in Fig. 20. This galaxy is thought not only to have a rapidly accreting massive black hole at its center but also to be undergoing an intense burst of star formation in its nucleus (Efstathiou *et al.*, 2014). Both of these heat the dust in their vicinity, creating a bright source of IR continuum that is unresolved at such a large distance. The lines of H_3^+, seen in absorption against the continuum radiation, probably arise predominantly in diffuse gas since the spectral signature of a large column density of complex hydrocarbons, well known to be found in diffuse gas, is present at 3.4 μm (Geballe *et al.*, 2006). The column density of H_3^+ derived from these lines is comparable to that seen in the CMZ; see Fig. 20. Its temperature is ~100 K, significantly lower than the temperature of the CMZ diffuse gas, although with high uncertainty. It is possible that the line of sight includes H_3^+ in both cold and dense gas and warm diffuse gas, similar to the sight lines toward the Galactic Center.

The other galaxy in which H_3^+ has been detected is the much closer prototypical type II Seyfert galaxy NGC 1068 (Geballe, Mason, and Oka, 2015). H_3^+ is the only small interstellar

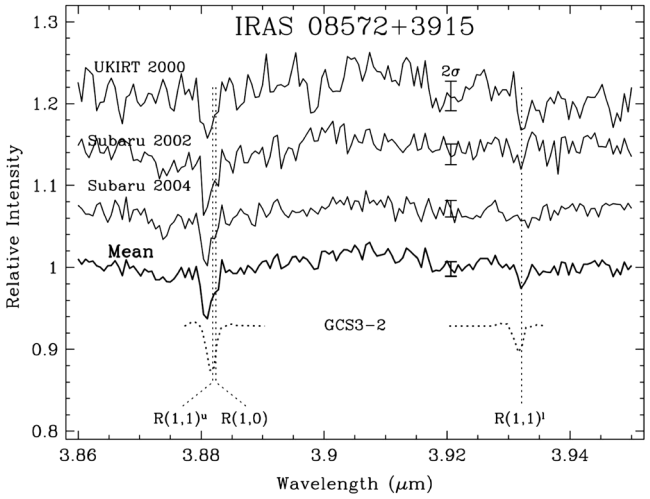

FIG. 20. Three spectra of H_3^+ lines toward the nucleus of the galaxy IRAS 08573+3915, obtained using UKIRT and the Subaru Telescope. The spectra are displayed at a resolving power of 5000. At bottom the mean of the spectra is shown along with the profiles of the same lines toward a star in the Galactic Center, redshifted to the radial velocity of IRAS 08572+3915 and binned to the same resolving power. From Geballe *et al.*, 2006.

molecule in NGC 1068 that has been detected in absorption toward its nucleus. Its presence is consistent with the existence in front of the active galactic nucleus of a significant column density of diffuse gas, already known to be present based on the strength of the 3.4 μm hydrocarbon feature (Geballe *et al.*, 2009). The observed column density of absorbing H_3^+ is both considerably less than that toward the Galactic Center and considerably less than expected based on the strength of the 3.4 μm feature. Because the plane of this spiral galaxy is tilted at approximately 45° relative to the line of sight, it is thought that the gas producing these absorptions lies within a few tens of parsecs of the bright galactic nucleus, which is powered by infall of matter onto a SMBH.

B. Supernova 1987A

On the night of February 24, 1987, a bright supernova was detected in a satellite galaxy near the Milky Way, the Large Magellanic Cloud. It became clear that this supernova was just a day old, and a worldwide campaign of observations was instigated to ensure that what was probably a once-in-a-lifetime event was studied in as much detail, at as many wavelengths, and for as long as possible. [See Spyromilio *et al.* (2017) for a review.] SN1987A was identified as a type II supernova with a relatively unusual blue supergiant progenitor. Detailed IR spectra were presented by Meikle *et al.* (1989) for the first few hundred days post explosion.

Among the host of other lines and features (atomic and molecular), Miller *et al.* (1992) identified two at 3.41 and 3.53 μm with groupings of transitions that were routinely being used to monitor Jupiter's H_3^+ auroral regions; see, e.g. Connerney *et al.* (1993). These features were particularly evident in the Day 192 spectrum (Meikle *et al.*, 1989) but were also, less distinctly, visible at later times (Miller *et al.*, 1992). This led to the conclusion that H_3^+ was indeed being formed in the shock-heated envelope gas that had been given off in the period when the SN1987A progenitor was undergoing rapid mass loss.

The quality of spectra and the possible contamination of the features by other emitters made it hard to determine the exact temperatures and H_3^+ densities, so a range was used, bearing in mind that thermal dissociation was likely to set in at $T \sim$ 4000 K (Kylänpää and Rantala, 2011). The relatively low gas temperature (1000 and 2050 K were used to generate spectra that could fit the observed features) and the existence of a few $\times 10^{-8}$ $M_\odot$ of H_3^+ meant that microscopic mixing of the envelope gas and the ejecta material could not have happened: in particular, O-, C-, and N-containing molecules, which could be seen in the overall SN1987A spectra, would have destroyed H_3^+ had microscopic mixing occurred.

The identification of the Day 192 features at 3.41 and 3.53 μm with H_3^+ has not been accepted universally (Oka, 1992). Spectroscopists usually like clean line transitions or features to identify novel species in previously unexpected environments. Subsequent modeling by Yan and Dalgarno (1998) confirmed that the spectroscopic identification was consistent with an H_3^+ mass of 1.6×10^{-7} $M_\odot$, emitting at 2000 K, and with an expansion velocity of 2350 km s^{-1}. They were able to explain the absence of some spectral features between 3.0 and 3.3 μm as being due to telluric (mainly water) absorption. Their model also made use of the macroscopic mixing approach, which kept metal-rich ejecta gas from mixing microscopically with the original envelope gas, for at least some hundreds of days. This is an important conclusion should it be possible to monitor another such supernova in as much detail as SN1987A since it would predict certain features of the way in which the various gases (ejecta and envelope) might or might not mix during the first year or so post explosion.

C. Exoplanetary systems

The detection of a Hot Jupiter exoplanet by Mayor and Queloz (1995) prompted discussions about what would characterize its atmosphere and the resulting emissions, should they be detectable. The role played by H_3^+ in the Solar System's giant planets added to these discussions: would emission from this molecule be observable, and what role might it play in the dynamics, heating, cooling, and chemistry there (Miller *et al.*, 2000)? Several attempts have been made to observe H_3^+ emission from exoplanetary systems: the planets themselves and/or the circumstellar disks from which they are forming.

Modeling studies have looked at the possible occurrence and role of H_3^+ in exoplanetary atmsopheres. Using a 1D, nonhydrostatic model to simulate the Hot Jupiter HD209458B, which orbits at 0.047 AU from its host star, Yelle (2004) demonstrated that the upper atmosphere was too hot for H_3^+ to form. Instead the dominant ion was H^+ and the upper atmosphere was extremely distended out to several planetary radii. This corroborated observations by Vidal-Madjar *et al.* (2003) that this planet did indeed have an extended atmosphere. The JIM model (Achilleos *et al.*, 1998) had already been used to probe the effect of increasing the

level of ionizing EUV radiation on the atmosphere of an exoplanet (Miller *et al.*, 2000).

Koskinen *et al.* (2007) used a new 3D exoplanet model to simulate the effects of a "Jupiter" migrating in from its current position 5 AU from the Sun (Koskinen, Aylward, and Miller, 2007). They found that as this hot Jupiter moved in toward the "Sun" it would heat up, with H_3^+ acting as a thermostat and the model remaining stable. This stable situation persisted until the Jupiter-Sun distance was ~0.16 AU, with H_3^+ emission balancing the extra heating due to EUV insolation, the H_3^+ thermostat effect really coming into its own. At this point, the Sun-facing hemisphere reached a temperature of ~3600 K and the planet's radius was roughly the same as Jupiter's (Koskinen *et al.*, 2007). Closer to the Sun, at 0.14 AU, EUV heating caused molecular hydrogen to dissociate to an extent that H_3^+ could not form: the temperature at the top of the atmosphere exceeded 23 000 K and the planetary radius more than doubled; the hydrostatic equilibrium approximation used by the model became invalid, and hydrodynamic escape of the atmosphere ensued. Koskinen and his coauthors speculated that since when the Sun was forming it would have emitted much higher EUV levels (Ribas, 2006) H_3^+ cooling might have been important in ensuring the formation and stability of Jupiter (and other gas giant planets), playing a key role in the evolution of the early Solar System (Koskinen *et al.*, 2007).

Koskinen, Aylward, and Miller (2009) then modeled the fluctuating levels of H_3^+ caused by the 27-fold variation in stellar irradiation from the eccentric orbit of exoplanet HD17156b. Unlike typical Hot Jupiters, this planet was able to maintain a stable atmosphere, even close to the star. This may provide a strong candidate for future H_3^+ detection, but it is currently beyond our instrument sensitivity limits (Shkolnik, Gaidos, and Moskovitz, 2006). Shaikhislamov *et al.* (2014) described the mass loss from giant exoplanets 0.05 AU from a Sun-like star. This model suggests that some H_3^+ may exist at the inner boundary of their model. At this distance, exospheric temperatures are large ($T_{exo} = 9000$ K), resulting in a significant mass loss rate of 5.5×10^7 kg s^{-1}. However, without H_3^+ cooling, the rate would have been about twice as much.

But what of observational studies? Ceccarelli *et al.* (2004, 2005) reported the detection of H_2D^+ in the disks surrounding the young star DM Tauri (and a more tentative detection in the TW Hydrae disk), raising the possibility that H_3^+ emission from exoplanetary systems might be possible. In 2002, Brittain and Rettig (2002) claimed to have observed line emission from the $Q(1, 0^-)(3.953\ \mu m)$ and $Q(3, 0^-)(3.986\ \mu m)$ lines from HD141569A, a Herbig AeBe star that is $(5–10) \times 10^6$ yr old, which they attributed to planet-forming gas surrounding the star. Their observations were made using the echelle spectrograph CSHELL (resolving power $\lambda/\Delta\lambda = 21\,500$) on the 3-m NASA IRTF. Brittain and Rettig (2002) derived a column density of 10^{20} m^{-3} for an extended protoplanet with a diameter of 2 AU and a rovibrational temperature of 420 K. Commenting on this report, however, Oka (2002) remarked that these observers had not been able to detect other equally intense H_3^+ lines.

Follow-up studies by Goto *et al.* (2005) and (for other systems) by Shkolnik, Gaidos, and Moskovitz (2006) failed to confirm the Brittain and Rettig (2002) detections, however. Goto *et al.* (2005), in particular, used larger telescopes: the 3.8 m UKIRT, with its spectrometer set at $\lambda/\Delta\lambda = 33\,000$, and the 8 m Subaru telescope with its spectrometer set to $\lambda/\Delta\lambda = 20\,000$. Neither telescope was able to confirm the Brittain and Rettig (2002) detections. Goto *et al.* (2005) concluded that the line intensities from the HD141569 system had upper limits of 3×10^{-19} W m^{-2}, some 10^2 less than those proposed by Miller *et al.* (2000) to be observable from Earth. Lenz *et al.* (2016) also reported a failure to find H_3^+ emission from HD209458 using VLT CRIRES and suggested that there is a lack of some 1–3 magnitudes of sensitivity at present for such emission to be detected, but that such planet's H_3^+ emissions might be detectable using future ~30-m-class telescopes like the Thirty Meter Telescope and the Extremely Large Telescope; to date no convincing detection of exoplanetary H_3^+ emission has been reported.

This difficulty in observing H_3^+ emission from Hot Jupiters was confirmed in modeling by Chadney *et al.* (2016), who showed that H_2 dissociation in highly irradiated planets effectively prevents H_3^+ from forming. However, planets at larger orbital distances have stable upper atmospheres without significant mass loss. As a result, the best candidate planets for H_3^+ detection would be those with moderate levels of EUV ionization, below that of Hot Jupiters but above that of Jupiter. However, even in these cases, H_3^+ emission is predicted to be too weak to observe with current instrumentation. Current attempts to detect exoplanetary system H_3^+ emissions have stalled somewhat, although future space missions such as Ariel (Tinetti *et al.*, 2018) offer a possible route forward.

Nonetheless, investigations into aurora from brown dwarf atmospheres continue to present the possibility of extrasolar gas giant aurora. Radio aurora have been detected emitting from brown dwarfs in orbit around host stars, as well as one planetary-mass brown dwarf that was potentially previously ejected from a planetary system (Hallinan *et al.*, 2015; Kao *et al.*, 2018). Modeling of brown dwarf atmospheres has shown that H_3^+ should be generated within the upper atmospheres of these stars, as a result of energetic particle precipitation, through ionization from interstellar UV radiation and galactic cosmic rays or by lightning (Helling and Rimmer, 2019). This suggests that the detection of H_3^+ in the upper atmosphere of a brown dwarf may prove to be the first step toward a fuller understanding of the ionospheres of both brown dwarfs and giant planets outside our Solar System.

D. Early Universe

Since only H, He, D, and Li had time to form before the Era of Recombination (some 300 000 years after the end of the hot big bang that started our Universe), the chemistry in the Early Universe was relatively simple. And since over 90% of all atoms are hydrogen atoms, H-bearing molecules feature significantly; see Lepp, Stancil, and Dalgarno (2002), Oka (2013), and Coppola and Galli (2019). Chief among these are H_2, HD, and H_2^+: H_2 reaches a relative abundance of over 10^{-5} (compared with the relative abundance of H, which is ~1) at

redshift $z = 100$ [$\sim 17 \times 10^6$ yr post big bang (PBB)]; all other molecules are several orders of magnitude less abundant. The H_3^+ molecular ion comes in at seventh or eighth most abundant at $z \sim 18$, the peak time for the formation of Population III stars ($\sim 200 \times 10^6$ yr PBB), with a relative abundance of $\sim 10^{-18}$ to 10^{-17} (Lepp, Stancil, and Dalgarno, 2002), although other models showed it peaking at a relative abundance of 10^{-17} to 10^{-16} much earlier: $z \sim 300/3 \times 10^6$ yr PBB (Gay *et al.*, 2011).

In the process of star formation, molecules are important once the protostellar gas cools to temperatures of a few thousand kelvins, temperatures that are low enough to prevent them from thermally dissociating. With no permanent dipole moment, H_2 is a relatively poor coolant per molecule. Nonetheless, H_2 is so abundant compared with other molecules that it is still the dominant coolant at all stages relevant to star formation in the Early Universe; see Glover (2011). H_2^+ is also a poor per-molecule coolant. The other molecules that are more abundant than H_3^+, HD, HD^+, HeH^+, and LiH^+, have permanent dipoles that make them more effective at cooling at low temperatures; HD^+ has a significant dipole due to the displacement of the center of mass from the center of charge, while HD's dipole is small.

Although its concentration is small at the crucial values of z, the high per-molecule cooling rate of H_3^+ (noted in Sec. III.B.2) prompted Glover and Savin (2009) to ask, "Is H_3^+ cooling ever important in the Early Universe?" Their standard modeling was able to produce a maximum contribution of $\sim 3\%$ of the cooling of the gas at densities of around 10^{14} m^{-3} and $T \sim 800$ K: this temperature corresponds to a black-body peak emission at 3.75 μm close to the center of the H_3^+ ν_2 band. Under certain (by Glover and Savin's own admission) unlikely circumstances of high cosmic-ray or x-ray fluxes, H_3^+ could even become the dominant cooling agent for a limited period of time, although overall "its effects on the temperature evolution of the gas remain small" (Glover and Savin, 2009). Work is currently under way to see if these conclusions are too pessimistic with respect to the role of H_3^+ in the Early Universe (Chen and Oka, 2019).

VI. CONCLUSIONS

This review of 30 years of H_3^+ astronomy has had of necessity to provide some of the physical chemistry and chemical physics of the molecule so that its role in planetary atmospheres and the ISM could be understood. It has always been a challenging species for both experimental spectroscopy and quantum calculations of the highest precision. One of the key challenges still to be fully met is that of understanding the near-dissociation spectrum of Carrington, Buttenshaw, and Kennedy (1982). For future applications to planetary science and studies of the ISM, it may well be that state-specific values for H_3^+ DR rate coefficients are required.

H_3^+ has long been used as a benchmark of *ab initio* studies: calculations on the H_2 molecule have reached an exquisite level of accuracy that is matched by the highest accuracy experiments based on the use of frequency combs. While experiments of similar accuracy are available for H_3^+, theoretical studies lag well behind, many orders of magnitude (at least 10^4) less accurate. H_3^+ should now become the test bed for developing high accuracy procedures that can accurately treat systems having more than 1 vibrational degree of freedom.

There is no doubt that the detection of H_3^+ on Jupiter by Drossart *et al.* (1989) laid the basis for what might be called an industry involving scores of researchers either making observations or creating models to understand how the ion was formed and where, its role in heating and cooling planetary atmospheres, and its potential for stabilizing (exo)planets close to their central star. The past 30 years have been a time of enormous riches for planetary scientists, with the Hubble Space Telescope, *Galileo* (Jupiter), and *Cassini* (Saturn) delivering much more than could possibly have been hoped for, and with the development of new, larger telescopes and of instruments that have transformed the sensitivity of telescopes old and new.

The continuing *Juno* mission, along with associated supporting observations, holds out the prospect of a wealth of new morphological information. These promise to reveal new details about the nature of Jupiter's aurora and have been heralded by recent conference proceedings, describing, for example, detailed measurements of the polar aurora producing flare emissions that evolve in such a way as to be reminiscent of raindrops striking a pond, and yet, alongside all other polar emissions, completely switching off at night (Greathouse *et al.*, 2017). *Juno* will be followed by data from JUICE and TANDEM to Jupiter in the 2030s, and missions to other giant planetary systems are being planned in which H_3^+ studies will play their role in enhancing how we understand the workings of these planets: they may even solve the problem of explaining the energy gap. And it is clear we must explain that, for how can we understand exoplanetary systems without understanding our own Solar System?

Indeed, work to try to sort out the energy gap in the upper atmospheres is now proceeding on a number of modeling fronts. Yates *et al.* (2020) produced new Jovian model results that now show a much greater flow of heat from higher to lower latitudes. They describe their model of the coupled magnetosphere ionosphere thermosphere of Jupiter as an "intermediate model" since the magnetosphere remains axisymmetric. Their next step is to include "realistic mapping from the magnetosphere to the ionosphere and local time variation," a more detailed ionosphere, and the inclusion of atmospheric waves. Müller-Wodarg *et al.* (2019) published recent results that concluded that energy from the auroral-polar regions can be transported to lower latitudes more effectively than previously thought if Rayleigh drag due to atmospheric waves, to slow down zonal (west-east) winds, is enhanced. Vriesema *et al.* (2019) and Vriesema, Koskinen, and Yelle (2020)reported on results from models of currents in the lower ionosphere may play some part in bridging the gap, even if they cannot supply all of the heating needed. And Lian and Yelle (2019) returned to gravity waves, generated in the lower atmosphere and breaking in the thermosphere, themselves as a source of heating. Further developments, and others that may help to resolve the giant planet energy gap, are eagerly awaited.

In interstellar gas, where hydrogen and helium are by far the dominant elements, H_3^+ is ubiquitous whenever that gas is cold and dense enough that molecules can form. While only a trace constituent of molecular interstellar gas, its fully allowed rovibrational absorption spectrum is much stronger than that of H_2, which can be observed only via its quadrupole lines. H_3^+ has several characteristics that make spectroscopy of it a unique and valuable probe of physical conditions in the gas. The most important of these are its suitability as both a thermometer and at low densities a densitometer. Moreover, because it is a charged molecule and is created in a simple, straightforward manner following cosmic-ray ionization of H_2, it also is a powerful *in situ* probe for measuring the cosmic-ray flux. With the imminent advent of larger telescopes and more sensitive IR spectrographs, both on Earth and in space, astronomers will soon be using H_3^+ as a tool to characterize more molecular environments in the Milky Way, as well as using it to study physical conditions in molecular gas in the more distant Universe.

Improvements on existing telescopes, such as the CRIRES instrument at ESO, have resulted in an order-of-magnitude increase in the wavelength coverage at resolving powers $\sim 10^5$, although at a restriction in the slit length from 60 to 10 in. This upgrade makes CRIRES even more attractive for studies of Saturn and Uranus (and potentially Neptune); for Jupiter increased wavelength coverage will improve the measurement of vertical temperature and density profiles and other local effects, although planetwide studies (limb-to-limb temperature, density, and velocity profiles) may be more challenging. The launch of the James Webb Space Telescope, which will carry out IR measurements (among others) above Earth's troublesome atmosphere, holds out the prospect of improvements of sensitivity by several orders of magnitude, perhaps enough to measure the H_3^+ signature of Neptune or an extrasolar planet. That said, recent laboratory studies aimed at modeling the upper atmospheres of heavily irradiated exoplanets have shown that while H_3^+ does form it also rapidly protonates other species (Bourgalais *et al.*, 2020). Thus, it may be difficult to detect directly, and we shall rely on spectral signatures such as that from H_3O^+ to know that it is forming.

The new generation of ~30-m-class telescopes being planned will give at least a threefold-to-fourfold increase in signal-to-noise ratio compared with their current largest ground-based "rivals"; depending on the nature of the objects being studied, order-of-magnitude increases in sensitivity may be anticipated. As has proved to be the case in the past, however, how much of an overall improvement we can expect in H_3^+ astronomy will depend on the sensitivity of the instruments that accompany the coming generation of large telescopes and other parameters such as wavelength coverage and optimization, and image or spectrometer spatial and spectral resolutions. The quality of their AO systems, their ability to "cancel out" fluctuations due to Earth's own atmosphere, is another area where continuing developments may be expected.

And, finally, may we make a plea for progress toward fully understanding the spectrum of Carrington *et al.* (Carrington and Kennedy, 1984; Carrington and McNab, 1989; Carrington, McNab, and West, 1993)?

ACKNOWLEDGMENTS

We thank the three referees of this paper, whose criticisms and amendments have made it more precise and more accessible for nonspecialists. We are indebted to our many collaborators in research on H_3^+, in particular, N. Achilleos, M. Goto, N. Indriolo, B. J. McCall, H. Melin, and O. L. Polyansky. The authors especially thank Professor Takeshi Oka for his enthusiastic support. We acknowledge the countless fruitful discussions over three decades that we, individually and collectively, have had together, for his unflagging championing of the importance of H_3^+ as a molecule of great chemical, physical, and astronomical importance, and for organizing meetings and conferences that have brought together and underpinned the community that has grown up around it. In part, this review was enabled and underpinned by support from the Royal Society of London, under whose auspices a series of highly successful meetings have been held on the subjects of H_3^+ and related topics since 2000. We gratefully acknowledge the Society's past and continuing support with these gatherings. We also acknowledge the support of the UK's Royal Astronomical Society. S. M is grateful to University College London for his award of an emeritus professorship. His work has been variously enabled and funded by the Maunakea Observatory (Hawaii) and its component observatories, by the UK Science and Technology Facilities Council, and by the European Commission, especially through its funding of the Europlanet Research Infrastructure of European planetary scientists. T. R. G gratefully acknowledges the support of the international Gemini Observatory, a program of NSF's NOIRLab, which is managed by the Association of Universities for Research in Astronomy (AURA) under a cooperative agreement with the National Science Foundation on behalf of the Gemini Observatory partnership: the National Science Foundation (United States), National Research Council (Canada), Agencia Nacional de Investigación y Desarrollo (Chile), Ministerio de Ciencia, Tecnología e Innovación (Argentina), Ministério da Ciência, Tecnologia, Inovações e Comunicações (Brazil), and Korea Astronomy and Space Science Institute (Republic of Korea). T. S is grateful for the continued support from the University of Leicester. His work has previously been directly supported by the UK Science and Technology Facilities Council, who continue to provide studentship funding to his Ph.D. students. His work would also be impossible without the continued observations from various telescopes in both Maunakea, Hawaii, and Paranal, Chile, and especially the sustained support of the various staff members at those telescope facilities.

REFERENCES

Abel, B., and R. M. Thorne, 2003, Icarus **166**, 311.

Achilleos, N., S. Miller, B. M. Dinelli, H. A. Lam, J. Tennyson, M. F. Jagod, T. R. Geballe, L. M. Trafton, R. D. Joseph, and G. E. Ballester, 1995, in *Proceedings of the European SL-9/Jupiter Workshop, Garching, Germany*, Vol. 52, edited by R. M. West and Hermann Böhnhardt (European Southern Observatory, Garching, Germany), pp. 375–380.

Achilleos, N., S. Miller, R. Prangé, G. Millward, and M. K. Dougherty, 2001, New J. Phys. **3**, 3.

Achilleos, N., S. Miller, J. Tennyson, A. D. Aylward, I. Mueller-Wodarg, and D. Rees, 1998, J. Geophys. Res. **103**, 20089.

Acuna, M. H., K. W. Behannon, and J. E. P. Connerney, 1983, in *Physics of the Jovian Magnetosphere*, edited by A. J. Dessler (Cambridge University Press, Cambridge, England), pp. 1–50.

Adriani, A., A. Mura, M. L. Moriconi, B. M. Dinelli, F. Fabiano, F. Altieri, G. Sindoni, S. J. Bolton, J. E. P. Connerney, and S. K. Atreya, 2017, Geophys. Res. Lett. **44**, 4633.

Adriani, A., *et al.*, 2017, Space Sci. Rev. **213**, 393.

Aguado, A., O. Roncero, C. Tablero, C. Sanz, and M. Paniagua, 2000, J. Chem. Phys. **112**, 1240.

Albertsson, T., N. Indriolo, H. Kreckel, D. Semenov, K. N. Crabtree, and T. Henning, 2014, Astrophys. J. **787**, 44.

Albertsson, T., D. A. Semenov, A. I. Vasyunin, T. Henning, and E. Herbst, 2013, Astrophys. J. Suppl. Ser. **207**, 27.

Altieri, F., B. M. Dinelli, A. Migliorini, M. L. Moriconi, G. Sindoni, A. Adriani, A. Mura, and F. Fabiano, 2016, Geophys. Res. Lett. **43**, 11 558.

Alvarez, I., F. B. Yousif, J. de Urquijo, and C. Cisneros, 2000, J. Phys. B **33**, L317.

Amano, T., 1988, Astrophys. J. **329**, L121.

Amaral, P. H. R., M. Stanke, L. Adamowicz, L. G. Diniz, J. R. Mohallem, and A. Alijah, 2019, Phil. Trans. R. Soc. A **377**, 20180411.

Anderson, J. B., 1992, J. Chem. Phys. **96**, 3702.

Andrews, D. J., E. J. Bunce, S. W. H. Cowley, M. K. Dougherty, G. Provan, and D. J. Southwood, 2008, J. Geophys. Res. Space Phys. **113**, A09205.

Anicich, V., and J. Futrell, 1984, Int. J. Mass Spectrom. Ion Process. **55**, 189.

Anicich, V. G., and T. R. Huntress, Jr., 1986, Astrophys. J. Suppl. Ser. **62**, 553.

Aptaker, I. M., 1987, Proc. SPIE Int. Soc. Opt. Eng. **0834**, 196.

Armstrong, T. P., M. T. Paonessa, S. T. Brandon, S. M. Krimigis, and L. J. Lanzerotti, 1981, J. Geophys. Res. **86**, 8343.

Atreya, S. K., and T. M. Donahue, 1975, Icarus **24**, 358.

Atreya, S. K., T. M. Donahue, and M. B. McElroy, 1974, Science **184**, 154.

Bachorz, R. A., W. Cencek, R. Jaquet, and J. Komasa, 2009, J. Chem. Phys. **131**, 024105.

Bader, A., S. V. Badman, J. Kinrade, S. W. H. Cowley, G. Provan, and W. R. Pryor, 2018, J. Geophys. Res. Space Phys. **123**, 8459.

Badman, S. V., N. Achilleos, C. S. Arridge, K. H. Baines, R. H. Brown, E. J. Bunce, A. J. Coates, S. W. H. Cowley, M. K. Dougherty, and M. Fujimoto, 2012, J. Geophys. Res. Space Phys. **117**, A01211.

Badman, S. V., D. J. Andrews, S. W. H. Cowley, L. Lamy, G. Provan, C. Tao, S. Kasahara, T. Kimura, M. Fujimoto, and H. Melin, 2012, J. Geophys. Res. Space Phys. **117**, A09228.

Ballester, G. E., S. Miller, J. Tennyson, L. M. Trafton, and T. R. Geballe, 1994, Icarus **107**, 189.

Baron, R., R. D. Joseph, T. Owen, J. Tennyson, S. Miller, and G. E. Ballester, 1991, Nature (London) **353**, 539.

Barrow, D., K. I. Matcheva, and P. Drossart, 2012, Icarus **219**, 77.

Barthelemy, M., M. B. Lystrup, H. Menager, S. Miller, and J. Lilensten, 2011, Astron. Astrophys. **530**, A139.

Bates, D. R., M. F. Guest, and R. A. Kendall, 1993, Planet. Space Sci. **41**, 9.

Berblinger, M., C. Schlier, and E. Pollak, 1989, J. Chem. Phys. **93**, 2319.

Berg, M., A. Wolf, and A. Petrignani, 2012, Phil. Trans. R. Soc. A **370**, 5028.

Bhardwaj, A., and G. R. Gladstone, 2000, Rev. Geophys. **38**, 295.

Bohr, N., 1919, Medd. K. Vetenskapsakad. Nobelinst. **5**, 1.

Bonfond, B., D. Grodent, J. C. Gérard, T. Stallard, J. T. Clarke, M. Yoneda, A. Radioti, and J. Gustin, 2012, Geophys. Res. Lett. **39**, L01105.

Bougher, S. W., J. H. Waite, T. Majeed, and G. R. Gladstone, 2005, J. Geophys. Res. Planets **110**, E04008.

Bourgalais, J., N. Carrasco, Q. Changeat, O. Venot, L. Javanović, P. Pernot, J. Tennyson, K. L. Chubb, S. N. Yurchenko, and G. Tinetti, 2020, Astrophys. J. **895**, 77.

Brass, O., J. Tennyson, and E. Pollak, 1990, J. Chem. Phys. **92**, 3377.

Brice, N., and T. R. Mcdonough, 1973, Icarus **18**, 206.

Brittain, S. D., and T. W. Rettig, 2002, Nature (London) **418**, 57.

Brittain, S. D., T. Simon, C. Kulesa, and T. W. Rettig, 2004, Astrophys. J. **606**, 911.

Broadfoot, A. L., *et al.*, 1979, Science **204**, 979.

Broadfoot, A. L., *et al.*, 1989, Science **246**, 1459.

Brown, R. H., D. P. Cruikshank, A. T. Tokunaga, R. G. Smith, and R. N. Clark, 1988, Icarus **74**, 262.

Brown, R. H., *et al.*, 2004, Space Sci. Rev. **115**, 111.

Brünken, S., *et al.*, 2014, Nature (London) **516**, 219.

Carbary, J. F., 2013, Geophys. Res. Lett. **40**, 1902.

Carrington, A., J. Buttenshaw, and R. Kennedy, 1982, Mol. Phys. **45**, 753.

Carrington, A., and R. A. Kennedy, 1984, J. Chem. Phys. **81**, 91.

Carrington, A., and I. R. McNab, 1989, Acc. Chem. Res. **22**, 218.

Carrington, A., I. R. McNab, and Y. D. West, 1993, J. Chem. Phys. **98**, 1073.

Caselli, P., O. Sipilä, and J. Harju, 2019, Phil. Trans. R. Soc. A **377**, 20180401.

Caselli, P., F. F. S. van der Tak, C. Ceccarelli, and A. Bacmann, 2003, Astron. Astrophys. **403**, L37.

Ceccarelli, C., C. Dominik, E. Caux, B. Lefloch, and P. Caselli, 2005, Astrophys. J. **631**, L81.

Ceccarelli, C., C. Dominik, B. Lefloch, P. Caselli, and E. Caux, 2004, Astrophys. J. **607**, L51.

Cencek, W., J. Rychlewski, R. Jaquet, and W. Kutzelnigg, 1998, J. Chem. Phys. **108**, 2831.

Chadney, J. M., M. Galand, T. T. Koskinen, S. Miller, J. Sanz-Forcada, Y. C. Unruh, and R. V. Yelle, 2016, Astron. Astrophys. **587**, A87.

Chandler, M. O., and J. H. Waite, 1986, Geophys. Res. Lett. **13**, 6.

Chapman, R., S. Beard, M. Mountain, D. Pettie, A. Pickup, and R. Wade, 1990, Proc. SPIE Int. Soc. Opt. Eng. **1235**, 34.

Chaufray, J. Y., G. R. Gladstone, J. H. Waite, and J. T. Clarke, 2010, J. Geophys. Res. Planets **115**, E05002.

Chaufray, J. Y., T. K. Greathouse, G. R. Gladstone, J. H. Waite, J. P. Maillard, T. Majeed, S. W. Bougher, E. Lellouch, and P. Drossart, 2011, Icarus **211**, 1233.

Chen, Y.-S. M., and T. Oka, 2019, in *Proceedings of the 74th International Symposium on Molecular Spectroscopy, Urbana–Champaign, IL*, https://doi.org/10.15278/isms.2019.FA03.

Chowdhury, M. N., T. S. Stallard, H. Melin, and R. E. Johnson, 2019, Geophys. Res. Lett. **46**, 7137.

Christoffersen, R. E., S. Hagstrom, and F. Prosser, 1964, J. Chem. Phys. **40**, 236.

Clarke, J. T., G. E. Ballester, J. Trauger, R. Evans, J. E. P. Connerney, K. Stapelfeldt, D. Crisp, P. D. Feldman, C. J. Burrows, and S. Casertano, 1996, Science **274**, 404.

Clarke, J. T., L. Ben Jaffel, and J.-C. Gérard, 1998, J. Geophys. Res. **103**, 20217.

Clarke, J. T., D. Grodent, S. W. H. Cowley, E. J. Bunce, P. Zarka, J. E. P. Connerney, and T. Satoh, 2004, *Jupiter's Aurora*, Vol. 1 (Cambridge University Press, Cambridge, England), pp. 639–670.

Clarke, J. T., H. A. Weaver, P. D. Feldman, H. W. Moos, W. G. Fastie, and C. B. Opal, 1980, Astrophys. J. **240**, 696.

Clarke, J. T., *et al.*, 2002, Nature (London) **415**, 997.

Clarke, J. T., *et al.*, 2005, Nature (London) **433**, 717.

Clarke, K. E., D. J. Andrews, A. J. Coates, S. W. H. Cowley, and A. Masters, 2010, J. Geophys. Res. Space Phys. **115**, A05202.

Connerney, J. E. P., M. H. Acuna, and N. F. Ness, 1981, Bull. Am. Astron. Soc. **13**, 724.

Connerney, J. E. P., M. H. Acuña, N. F. Ness, and T. Satoh, 1998, J. Geophys. Res. **103**, 11929.

Connerney, J. E. P., R. Baron, T. Satoh, and T. Owen, 1993, Science **262**, 1035.

Connerney, J. E. P., S. Kotsiaros, R. J. Oliversen, J. R. Espley, J. L. Joergensen, P. S. Joergensen, J. M. G. Merayo, M. Herceg, J. Bloxham, and K. M. Moore, 2018, Geophys. Res. Lett. **45**, 2590.

Connerney, J. E. P., and J. H. Waite, 1984, Nature (London) **312**, 136.

Conroy, H., 1964, J. Chem. Phys. **41**, 1341.

Coppola, C. M. and D. Galli, 2019, in *Gas-Phase Chemistry in Space: From Elementary Particles to Complex Organic Molecules*, edited by F. Lique and A. Faure (IOP Astronomy, New York).

Cordonnier, M., D. Uy, R. M. Dickson, K. E. Kerr, Y. Zhang, and T. Oka, 2000, J. Chem. Phys. **113**, 3181.

Coulson, C. A., 1935, Math. Proc. Cambridge Philos. Soc. **31**, 244.

Cowley, S. W. H., and E. J. Bunce, 2001, Planet. Space Sci. **49**, 1067.

Cowley, S. W. H., E. J. Bunce, and R. Prangé, 2004, Ann. Geophys. **22**, 1379.

Cowley, S. W. H., E. J. Bunce, T. S. Stallard, and S. Miller, 2003, Geophys. Res. Lett. **30**, 1220.

Crabtree, K. N., N. Indriolo, H. Kreckel, B. A. Tom, and B. J. McCall, 2011, Astrophys. J. **729**, 15.

Cravens, T. E., 1994, Geophys. Res. Lett. **21**, 1075.

Cravens, T. E., and A. Dalgarno, 1978, Astrophys. J. **219**, 750.

Cravens, T. E., L. Moore, J. H. Waite, R. Perryman, M. Perry, J. E. Wahlund, A. Persoon, and W. S. Kurth, 2019, Geophys. Res. Lett. **46**, 6315.

Dessler, A. J., 1983, *Physics of the Jovian Magnetosphere* (Cambridge University Press, Cambridge, England).

Dinelli, B. M., N. Achilleos, H. A. Lam, J. Tennyson, S. Miller, M. F. Jagod, T. Oka, and T. R. Geballe, 1995, in *Proceedings of the European SL-9/Jupiter Workshop*, Vol. 52 (ESO, Garching, Germany), pp. 245–249.

Dinelli, B. M., A. Adriani, A. Mura, F. Altieri, A. Migliorini, and M. L. Moriconi, 2019, Phil. Trans. R. Soc. A **377**, 20180406.

Dinelli, B. M., F. Fabiano, A. Adriani, F. Altieri, M. L. Moriconi, A. Mura, G. Sindoni, G. Filacchione, F. Tosi, and A. Migliorini, 2017, Geophys. Res. Lett. **44**, 4625.

Dinelli, B. M., C. R. Le Sueur, J. Tennyson, and R. D. Amos, 1995, Chem. Phys. Lett. **232**, 295.

Dinelli, B. M., S. Miller, N. Achilleos, H. An Lam, M. Cahill, J. Tennyson, M.-F. Jagod, T. Oka, J.-C. Hilico, and T. R. Geballe, 1997, Icarus **126**, 107.

Dinelli, B. M., S. Miller, and J. Tennyson, 1992, J. Mol. Spectrosc. **153**, 718 .

Diniz, L. G., J. R. Mohallem, A. Alijah, M. Pavanello, L. Adamowicz, O. L. Polyansky, and J. Tennyson, 2013, Phys. Rev. A **88**, 032506.

Dols, V., J. C. Gerard, F. Paresce, R. Prange, and A. Vidal-Madjar, 1992, Geophys. Res. Lett. **19**, 1803.

dos Santos, S. F., V. Kokoouline, and C. H. Greene, 2007, J. Chem. Phys. **127**, 124309.

Drossart, P., 2019, Phil. Trans. R. Soc. A **377**, 20180404.

Drossart, P., J. P. Maillard, J. Caldwell, S. J. Kim, J. K. G. Watson, W. A. Majewski, J. Tennyson, S. Miller, S. K. Atreya, and J. T. Clarke, 1989, Nature (London) **340**, 539.

Drossart, P., J. P. Maillard, J. Caldwell, and J. Rosenqvist, 1993, Astrophys. J. **402**, L25.

Dungey, J. W., 1961, Phys. Rev. Lett. **6**, 47.

Efstathiou, A., *et al.*, 2014, Mon. Not. R. Astron. Soc. **437**, L16.

Egert, A., J. H. Waite, and J. Bell, 2017, J. Geophys. Res. Space Phys. **122**, 2210.

Elias, J. H., *et al.*, 1998, Proc. SPIE Int. Soc. Opt. Eng. **3354**, 555.

Encrenaz, T., B. Schulz, P. Drossart, E. Lellouch, H. Feuchtgruber, and S. K. Atreya, 2000, Astron. Astrophys. **358**, L83.

Encrenaz, T., R. Schulz, J. A. Stuewe, G. Wiedemann, P. Drossart, and J. Crovisier, 1994, The Messenger **77**, 40.

Eyring, H., J. O. Hirschfelder, and H. S. Taylor, 1936, J. Chem. Phys. **4**, 570.

Farnik, M., S. Davis, M. A. Kostin, O. L. Polyansky, J. Tennyson, and D. J. Nesbitt, 2002, J. Chem. Phys. **116**, 6146.

Fehsenfeld, F. C., 1976, Astrophys. J. **209**, 638.

Festou, M. C., and S. K. Atreya, 1982, Geophys. Res. Lett. **9**, 1147.

Feuchtgruber, H., and T. Encrenaz, 2003, Astron. Astrophys. **403**, L7.

Flower, D. R., G. Pineau des Forêts, and C. M. Walmsley, 2004, Astron. Astrophys. **427**, 887.

Friedrich, O., A. Alijah, Z. Xu, and A. J. C. Varandas, 2001, Phys. Rev. Lett. **86**, 1183.

Furtenbacher, T., T. Szidarovszky, C. Fábri, and A. G. Császár, 2013, Phys. Chem. Chem. Phys. **15**, 10181.

Furtenbacher, T., T. Szidarovszky, E. Mátyus, C. Fábri, and A. G. Császár, 2013, J. Chem. Theory Comput. **9**, 5471.

Galand, M., L. Moore, I. Mueller-Wodarg, M. Mendillo, and S. Miller, 2011, J. Geophys. Res. Space Phys. **116**, A09306.

Gay, C. D., P. C. Stancil, S. Lepp, and A. Dalgarno, 2011, Astrophys. J. **737**, 44.

Geballe, T. R., 2000, Phil. Trans. R. Soc. A **358**, 2359.

Geballe, T. R., M. Goto, T. Usuda, T. Oka, and B. J. McCall, 2006, Astrophys. J. **644**, 907.

Geballe, T. R., M. F. Jagod, and T. Oka, 1993, Astrophys. J. **408**, L109.

Geballe, T. R., E. Lambrides, B. Schlegelmilch, S. C. C. Yeh, M. Goto, C. Westrick, T. Oka, and F. Najarro, 2019, Astrophys. J. **872**, 103.

Geballe, T. R., R. E. Mason, and T. Oka, 2015, Astrophys. J. **812**, 56.

Geballe, T. R., R. E. Mason, A. Rodríguez-Ardila, and D. J. Axon, 2009, Astrophys. J. **701**, 1710.

Geballe, T. R., B. J. McCall, K. H. Hinkle, and T. Oka, 1999, Astrophys. J. **510**, 251.

Geballe, T. R., and T. Oka, 1989, Astrophys. J. **342**, 855.

Geballe, T. R., and T. Oka, 1996, Nature (London) **384**, 334.

Geballe, T. R., and T. Oka, 2010, Astrophys. J. **709**, L70.

Geballe, T. R., T. Oka, and M. Goto, 2019, Phil. Trans. R. Soc. A **377**, 20180400.

Gehrels, N., E. C. Stone, and J. H. Trainor, 1981, J. Geophys. Res. **86**, 8906.

Gérard, J. C., B. Bonfond, J. Gustin, D. Grodent, J. T. Clarke, D. Bisikalo, and V. Shematovich, 2009, Geophys. Res. Lett. **36**, L02202.

Gérard, J. C., *et al.*, 2018, Icarus **312**, 145.

Gérard, J.-C., A. Saglam, D. Grodent, and J. T. Clarke, 2006, J. Geophys. Res. Space Phys. **111**, A04202.

Gerlich, D., E. Herbst, and E. Roueff, 2002, Planet. Space Sci. **50**, 1275.

Gibb, E. L., S. D. Brittain, T. W. Rettig, M. Troutman, T. Simon, and C. Kulesa, 2010, Astrophys. J. **715**, 757.
Giles, R. S., L. N. Fletcher, P. G. J. Irwin, H. Melin, and T. S. Stallard, 2016, Astron. Astrophys. **589**, A67.
Glocer, A., T. I. Gombosi, G. Toth, K. C. Hansen, A. J. Ridley, and A. Nagy, 2007, J. Geophys. Res. Space Phys. **112**, A01304.
Glosik, J., P. Dohnal, P. Rubovic, A. Kalosi, R. Plasil, S. Roucka, and R. Johnsen, 2015, Plasma Sources Sci. Technol. **24**, 065017.
Glosik, J., R. Plasil, V. Poterya, P. Kudrna, M. Tichy, and A. Pysanenko, 2001, J. Phys. B **34**, L485.
Glover, S. C. O., 2011, in *The Molecular Universe*, IAU Symposium Vol. 280, edited by J. Cernicharo and R. Bachiller (Cambridge University Press, Cambridge, England), pp. 313–324.
Glover, S. C. O., and D. W. Savin, 2009, Mon. Not. R. Astron. Soc. **393**, 911.
Gomez Llorente, J. M., and E. Pollak, 1988, J. Chem. Phys. **89**, 1195.
Goto, M., T. R. Geballe, J. Harju, P. Caselli, O. Sipilä, K. M. Menten, and T. Usuda, 2019, Astron. Astrophys. **632**, A29.
Goto, M., T. R. Geballe, B. J. McCall, T. Usuda, H. Suto, H. Terada, N. Kobayashi, and T. Oka, 2005, Astrophys. J. **629**, 865.
Goto, M., T. R. Geballe, and T. Usuda, 2015, Astrophys. J. **806**, 57.
Goto, M., B. J. McCall, T. R. Geballe, T. Usuda, N. Kobayashi, H. Terada, and T. Oka, 2002, Publ. Astron. Soc. Jpn. **54**, 951.
Goto, M., T. Usuda, T. R. Geballe, N. Indriolo, B. J. McCall, T. Henning, and T. Oka, 2011, Publ. Astron. Soc. Jpn. **63**, L13.
Goto, M., T. Usuda, T. Nagata, T. R. Geballe, B. J. McCall, N. Indriolo, H. Suto, T. Henning, C. P. Morong, and T. Oka, 2008, Astrophys. J. **688**, 306.
Gottfried, J.-L., 2006, Phil. Trans. R. Soc. A **364**, 2917.
Greathouse, T. K., *et al.*, 2017, in *Proceedings of the AGU Fall Meeting Abstracts*, Vol. 2017 (American Geophysical Union, Washington, DC), pp. P24A–07.
Grechko, M., O. V. Boyarkin, T. R. Rizzo, P. Maksyutenko, N. F. Zobov, S. Shirin, L. Lodi, J. Tennyson, A. G. Császár, and O. L. Polyansky, 2009, J. Chem. Phys. **131**, 221105.
Grechko, M., P. Maksyutenko, T. R. Rizzo, and O. V. Boyarkin, 2010, J. Chem. Phys. **133**, 081103.
Greene, T. P., A. T. Tokunaga, D. W. Toomey, and J. B. Carr, 1993, Proc. SPIE Int. Soc. Opt. Eng. **1946**, 313.
Griffiths, R., 1990, Hubble Space Telescope: Wide field and planetary camera instrument handbook, version 2.1.
Grodent, D., B. Bonfond, J.-C. Gérard, A. Radioti, J. Gustin, J. T. Clarke, J. Nichols, and J. E. P. Connerney, 2008, J. Geophys. Res. Space Phys. **113**, A09201.
Grodent, D., J. T. Clarke, J. Kim, J. H. Waite, and S. W. H. Cowley, 2003, J. Geophys. Res. Space Phys. **108**, 1389.
Grodent, D., J. T. Clarke, J. H. Waite, S. W. H. Cowley, J. C. Gérard, and J. Kim, 2003, J. Geophys. Res. Space Phys. **108**, 1366.
Grodent, D., J. C. Gérard, S. W. H. Cowley, E. J. Bunce, and J. T. Clarke, 2005, J. Geophys. Res. Space Phys. **110**, A07215.
Grodent, D., J. H. Waite, Jr., and J.-C. Gérard, 2001, J. Geophys. Res. **106**, 12933.
Grussie, F., M. H. Berg, K. N. Crabtree, S. Gaertner, B. J. McCall, S. Schlemmer, A. Wolf, and H. Kreckel, 2012, Astrophys. J. **759**, 21.
Guan, Y.-C., Y.-H. Chang, Y.-C. Liao, J.-L. Peng, L.-B. Wang, and J.-T. Shy, 2018, J. Chem. Phys. **148**, 124310.
Guberman, S. L., 1994, Phys. Rev. A **49**, R4277.
Gurnett, D. A., A. Lecacheux, W. S. Kurth, A. M. Persoon, J. B. Groene, L. Lamy, P. Zarka, and J. F. Carbary, 2009, Geophys. Res. Lett. **36**, L16102.
Gurnett, D. A., A. M. Persoon, W. S. Kurth, J. B. Groene, T. F. Averkamp, M. K. Dougherty, and D. J. Southwood, 2007, Science **316**, 442.
Hallinan, G., *et al.*, 2015, Nature (London) **523**, 568.
Hamilton, D. C., D. C. Brown, G. Gloeckler, and W. I. Axford, 1983, J. Geophys. Res. **88**, 8905.
Hamilton, D. C., G. Gloeckler, S. M. Krimigis, C. O. Bostrom, T. P. Armstrong, W. I. Axford, C. Y. Fan, L. J. Lanzerotti, and D. M. Hunten, 1980, Geophys. Res. Lett. **7**, 813.
Hamilton, D. C., G. Gloeckler, S. M. Krimigis, and L. J. Lanzerotti, 1981, J. Geophys. Res. **86**, 8301.
Hammel, H. B., *et al.*, 1995, Science **267**, 1288.
Harju, J., *et al.*, 2017, Astrophys. J. **840**, 63.
Helling, C., and P. Rimmer, 2019, Phil. Trans. R. Soc. A **377**, 20180398.
Henderson, J. R., and J. Tennyson, 1996, Mol. Phys. **89**, 953.
Herbst, E., and W. Klemperer, 1973, Astrophys. J. **185**, 505.
Hill, T. W., 1979, J. Geophys. Res. **84**, 6554.
Hill, T. W., 2001, J. Geophys. Res. **106**, 8101.
Hillenbrand, P.-M., K. P. Bowen, J. Liévin, X. Urbain, and D. W. Savin, 2019, Astrophys. J. **877**, 38.
Hily-Blant, P., A. Faure, C. Rist, G. P. des Forets, and D. R. Flower, 2018, Mon. Not. R. Astron. Soc. **477**, 4454.
Hirschfelder, J., H. Diamond, and H. Eyring, 1937, J. Chem. Phys. **5**, 695.
Hirschfelder, J., H. Eyring, and N. Rosen, 1936a, J. Chem. Phys. **4**, 121.
Hirschfelder, J., H. Eyring, and N. Rosen, 1936b, J. Chem. Phys. **4**, 130.
Hirschfelder, J., H. Eyring, and B. Topley, 1936, J. Chem. Phys. **4**, 170.
Hirschfelder, J. O., 1938, J. Chem. Phys. **6**, 795.
Hirschfelder, J. O., and C. N. Weygandt, 1938, J. Chem. Phys. **6**, 806.
Hogness, T. R., and E. G. Lunn, 1925, Phys. Rev. **26**, 0044.
Hoyland, J. R., 1964, J. Chem. Phys. **41**, 1370.
Huang, T. S., and T. W. Hill, 1989, J. Geophys. Res. **94**, 3761.
Hubbard, W., R. E. Nather, D. S. Evans, R. G. Tull, D. C. Wells, G. W. van Citters, B. Warner, and P. vanden Bout, 1972, Astron. J. **77**, 41.
Hugo, E., O. Asvany, and S. Schlemmer, 2009, J. Chem. Phys. **130**, 164302.
Hunt, G. J., S. W. H. Cowley, G. Provan, E. J. Bunce, I. I. Alexeev, E. S. Belenkaya, V. V. Kalegaev, M. K. Dougherty, and A. J. Coates, 2014, J. Geophys. Res. Space Phys. **119**, 9847.
Indriolo, N., G. A. Blake, M. Goto, T. Usuda, T. R. Geballe, T. Oka, and B. J. McCall, 2010, Astrophys. J. **724**, 1357.
Indriolo, N., B. D. Fields, and B. J. McCall, 2009, Astrophys. J. **694**, 257.
Indriolo, N., T. R. Geballe, T. Oka, and B. J. McCall, 2007, Astrophys. J. **671**, 1736.
Indriolo, N., and B. J. McCall, 2012, Astrophys. J. **745**, 91.
Indriolo, N., *et al.*, 2015, Astrophys. J. **800**, 40.
Ingersoll, A. P., G. Muench, G. Neugebauer, D. J. Diner, G. S. Orton, B. Schupler, M. Schroeder, S. C. Chase, R. D. Ruiz, and L. M. Trafton, 1975, Science **188**, 472.
Jaquet, R., and M. V. Khoma, 2018, Mol. Phys. **116**, 3507.
Jia, X., M. G. Kivelson, and T. I. Gombosi, 2012, J. Geophys. Res. Space Phys. **117**, A04215.
Johnsen, R., and S. L. Guberman, 2010, E. Arimondo, P. R. Berman, and C. C. Lin, Adv. At. Mol. Opt. Phys. **59**, 75.
Johnson, R. E., H. Melin, T. S. Stallard, C. Tao, J. D. Nichols, and M. N. Chowdhury, 2018, J. Geophys. Res. Space Phys. **123**, 5990.
Johnson, R. E., T. S. Stallard, H. Melin, S. Miller, and J. D. Nichols, 2016, Icarus **280**, 249.
Johnson, R. E., T. S. Stallard, H. Melin, J. D. Nichols, and S. W. H. Cowley, 2017, J. Geophys. Res. Space Phys. **122**, 7599.

Jones, K., M. Formanek, and L. Adamowicz, 2017, Chem. Phys. Lett. **669**, 188.
Kaeufl, H.-U., *et al.*, 2004, Proc. SPIE Int. Soc. Opt. Eng. **5492**, 1218.
Kaifu, N., T. Iguchi, and T. Kato, 1974, Publ. Astron. Soc. Jpn. **26**, 117.
Kaifu, N., T. Kato, and T. Iguchi, 1972, Nature (London) Phys. Sci. **238**, 105.
Kao, L., T. Oka, S. Miller, and J. Tennyson, 1991, Astrophys. J. Suppl. Ser. **77**, 317.
Kao, M. M., G. Hallinan, J. S. Pineda, D. Stevenson, and A. Burgasser, 2018, Astrophys. J. Suppl. Ser. **237**, 25.
Kedziora-Chudczer, L., D. V. Cotton, D. J. Kedziora, and J. Bailey, 2017, Icarus **294**, 156.
Kemp, F., C. E. Kirk, and I. R. McNab, 2000, Phil. Trans. R. Soc. A **358**, 2403.
Khurana, K. K., M. K. Dougherty, G. Provan, G. J. Hunt, M. G. Kivelson, S. W. H. Cowley, D. J. Southwood, and C. T. Russell, 2018, Geophys. Res. Lett. **45**, 10 068.
Kim, S., P. Drossart, J. Caldwell, and J. P. Maillard, 1990, Icarus **84**, 54.
Kim, S. J., P. Drossart, J. Caldwell, J.-P. Maillard, T. Herbst, and M. Shure, 1991, Nature (London) **353**, 536.
Kim, Y. H., 2012, J. Korean Astron. Soc. **45**, 39.
Kim, Y. H., J. L. Fox, and H. S. Porter, 1992, J. Geophys. Res. **97**, 6093.
Kim, Y. H., S. J. Kim, J. A. Stuewe, J. Caldwell, and T. M. Herbst, 1994, Icarus **112**, 326.
Kita, H., S. Fujisawa, C. Tao, M. Kagitani, T. Sakanoi, and Y. Kasaba, 2018, Icarus **313**, 93.
Kita, H., H. Misawa, A. Bhardwaj, F. Tsuchiya, T. Sakanoi, Y. Kasaba, C. Tao, Y. Miyoshi, and A. Morioka, 2015, J. Geophys. Res. Space Phys. **120**, 6614.
Kivelson, M. G., and C. T. Russell, 1995, *Introduction to Space Physics*, Cambridge Atmospheric and Space Science Series (Cambridge University Press, Cambridge, England).
Kobayashi, N., *et al.*, 2000, Proc. SPIE Int. Soc. Opt. Eng. **4008**, 1056.
Kokoouline, V., C. H. Greene, and B. D. Esry, 2001, Nature (London) **412**, 891.
Korobov, V. I., 2006, Phys. Rev. A **74**, 052506.
Koskinen, T. T., A. D. Aylward, and S. Miller, 2007, Nature (London) **450**, 845.
Koskinen, T. T., A. D. Aylward, and S. Miller, 2009, Astrophys. J. **693**, 868.
Koskinen, T. T., A. D. Aylward, C. G. A. Smith, and S. Miller, 2007, Astrophys. J. **661**, 515.
Kragh, H., 2010, Astron. Geophys. **51**, 6.25.
Kragh, H., 2012, Phil. Trans. R. Soc. A **370**, 5225.
Kreckel, H., O. Novotny, and A. Wolf, 2019, Phil. Trans. R. Soc. A **377**, 20180412.
Kreckel, H., A. Petrignani, O. Novotny, K. Crabtree, H. Buhr, B. J. McCall, and A. Wolf, 2012, Phil. Trans. R. Soc. A **370**, 5088.
Kreckel, H., D. Schwalm, J. Tennyson, A. Wolf, and D. Zajfman, 2004, New J. Phys. **6**, 151.
Kreckel, H., *et al.*, 2002, Phys. Rev. A **66**, 052509.
Kreckel, H., *et al.*, 2005, Phys. Rev. Lett. **95**, 263201.
Kreckel, H., *et al.*, 2010, Phys. Rev. A **82**, 042715.
Krimigis, S. M., T. P. Armstrong, W. I. Axford, C. O. Bostrom, G. Gloeckler, E. P. Keath, L. J. Lanzerotti, J. F. Carbary, D. C. Hamilton, and E. C. Roelof, 1982, Science **215**, 571.
Kylänpää, I., and T. T. Rantala, 2011, J. Chem. Phys. **135**, 104310.
Lam, H. A., N. Achilleos, S. Miller, J. Tennyson, L. M. Trafton, T. R. Geballe, and G. E. Ballester, 1997, Icarus **127**, 379.
Lam, H. A., S. Miller, R. D. Joseph, T. R. Geballe, L. M. Trafton, J. Tennyson, and G. E. Ballester, 1997, Astrophys. J. **474**, L73.
Lamy, L., R. Prangé, W. Pryor, J. Gustin, S. V. Badman, H. Melin, T. Stallard, D. G. Mitchell, and P. C. Brandt, 2013, J. Geophys. Res. Space Phys. **118**, 4817.
Lamy, L., *et al.*, 2012, Geophys. Res. Lett. **39**, L07105.
Lamy, L., *et al.*, 2017, J. Geophys. Res. Space Phys. **122**, 3997.
Larsson, M., B. J. McCall, and A. E. Orel, 2008, Chem. Phys. Lett. **462**, 145.
Leblanc, Y., and H. P. Ladreiter, 1992, Adv. Space Res. **12**, 23.
Lee, H. H., R. P. A. Bettens, and E. Herbst, 1996, Astron. Astrophys. Suppl. Ser. **119**, 111.
Lellouch, E., 2006, Phil. Trans. R. Soc. A **364**, 3139.
Lenz, L. F., A. Reiners, A. Seifahrt, and H. U. Käufl, 2016, Astron. Astrophys. **589**, A99.
Le Petit, F., M. Ruaud, E. Bron, B. Godard, E. Roueff, D. Languignon, and J. Le Bourlot, 2016, Astron. Astrophys. **585**, A105.
Lepp, S., P. C. Stancil, and A. Dalgarno, 2002, J. Phys. B **35**, R57.
Lester, D. F., P. M. Harvey, and J. Carr, 1988, Astrophys. J. **329**, 641.
Le Sueur, C. R., J. R. Henderson, and J. Tennyson, 1993, Chem. Phys. Lett. **206**, 429.
Lian, Y., and R. V. Yelle, 2019, Icarus **329**, 222.
Lindley, D., 1995, Science **267**, 1245.
Lindsay, C. M., and B. J. McCall, 2001, J. Mol. Spectrosc. **210**, 60.
Linsky, J. L., *et al.*, 2006, Astrophys. J. **647**, 1106.
Lis, D. C., E. Roueff, M. Gerin, T. G. Phillips, L. H. Coudert, F. F. S. van der Tak, and P. Schilke, 2002, Astrophys. J. **571**, L55.
Lodi, L., O. L. Polyansky, A. A. J. Tennyson, and N. F. Zobov, 2014, Phys. Rev. A **89**, 032505.
Lyons, J. R., 1995, Science **267**, 648.
Lystrup, M. B., S. Miller, N. Dello Russo, J. Vervack, R. J., and T. Stallard, 2008, Astrophys. J. **677**, 790.
Lystrup, M. B., S. Miller, T. Stallard, C. G. A. Smith, and A. Aylward, 2007, Ann. Geophys. **25**, 847.
Macchetto, F., 1982, in, NASA Conference Publication No. 2244, pp. 40–54.
Maillard, J. P., 2000, Astron. Soc. Pac. Conf. Ser. **195**, 185.
Maillard, J. P., and G. Michel, 1982, Astrophys. Space Sci. Libr. **92**, 213.
Maillard, J.-P., P. Drossart, J. K. G. Watson, S. J. Kim, and J. Caldwell, 1990, Astrophys. J. **363**, L37.
Majeed, T., and J. C. McConnell, 1991, Planet. Space Sci. **39**, 1715.
Majumdar, L., P. Gratier, M. Ruaud, V. Wakelam, C. Vastel, O. Sipilä, F. Hersant, A. Dutrey, and S. Guilloteau, 2017, Mon. Not. R. Astron. Soc. **466**, 4470.
Markus, C. R., and B. J. McCall, 2019, J. Chem. Phys. **150**, 214303.
Marten, A., C. de Bergh, T. Owen, D. Gautier, J. P. Maillard, P. Drossart, B. L. Lutz, and G. S. Orton, 1994, Planet. Space Sci. **42**, 391.
Martin, D. W., E. W. McDaniel, and M. L. Meeks, 1961, Astrophys. J. **134**, 1012.
Masters, A., 2015, J. Geophys. Res. Space Phys. **120**, 479.
Matcheva, K. I., and D. F. Strobel, 1999, Icarus **140**, 328.
Mayor, M., and D. Queloz, 1995, Nature (London) **378**, 355.
McCall, B. J., 2001, Ph.D. thesis (University of Chicago).
McCall, B. J., T. R. Geballe, K. H. Hinkle, and T. Oka, 1998, Science **279**, 1910.
McCall, B. J., T. R. Geballe, K. H. Hinkle, and T. Oka, 1999, Astrophys. J. **522**, 338.

McCall, B. J., K. H. Hinkle, T. R. Geballe, G. H. Moriarty-Schieven, I. Evans, N. J., K. Kawaguchi, S. Takano, V. V. Smith, and T. Oka, 2002, Astrophys. J. **567**, 391.
McCall, B. J., *et al.*, 2003, Nature (London) **422**, 500.
McCall, B. J., *et al.*, 2004, Phys. Rev. A **70**, 052716.
McLean, I. S., *et al.*, 1998, *Infrared Astronomical Instrumentation*, edited by A. M. Fowler, International Society for Optics and Photonics Vol. 3354 (SPIE), pp. 566–578.
Meikle, W. P. S., D. A. Allen, J. Spyromilio, and G. F. Varani, 1989, Mon. Not. R. Astron. Soc. **238**, 193.
Melin, H., 2006, Ph.D. thesis (University of London).
Melin, H., S. V. Badman, T. S. Stallard, S. W. H. Cowley, U. Dyudina, J. D. Nichols, G. Provan, J. O'Donoghue, W. R. Pryor, and K. H. Baines, 2016, Icarus **263**, 56.
Melin, H., L. N. Fletcher, T. S. Stallard, R. E. Johnson, J. O'Donoghue, L. Moore, and P. T. Donnelly, 2018, Mon. Not. R. Astron. Soc. **474**, 3714.
Melin, H., S. Miller, T. Stallard, and D. Grodent, 2005, Icarus **178**, 97.
Melin, H., S. Miller, T. Stallard, C. Smith, and D. Grodent, 2006, Icarus **181**, 256.
Melin, H., S. Miller, T. Stallard, L. M. Trafton, and T. R. Geballe, 2007, Icarus **186**, 234.
Melin, H., T. Stallard, S. Miller, J. Gustin, M. Galand, S. V. Badman, W. R. Pryor, J. O'Donoghue, R. H. Brown, and K. H. Baines, 2011, Geophys. Res. Lett. **38**, L15203.
Melin, H., T. Stallard, S. Miller, M. B. Lystrup, L. M. Trafton, T. C. Booth, and C. Rivers, 2011, Mon. Not. R. Astron. Soc. **410**, 641.
Melin, H., T. Stallard, S. Miller, L. M. Trafton, T. Encrenaz, and T. R. Geballe, 2011, Astrophys. J. **729**, 134.
Melin, H., and T. S. Stallard, 2016, Icarus **278**, 238.
Melin, H., T. S. Stallard, S. Miller, T. R. Geballe, L. M. Trafton, and J. O'Donoghue, 2013, Icarus **223**, 741.
Melin, H., *et al.*, 2019, Phil. Trans. R. Soc. A **377**, 20180408.
Meyer, W., P. Botschwina, and P. Burton, 1986, J. Chem. Phys. **84**, 891.
Migliorini, A., *et al.*, 2019, Icarus **329**, 132.
Milan, S. E., E. J. Bunce, S. W. H. Cowley, and C. M. Jackman, 2005, J. Geophys. Res. Space Phys. **110**, A03209.
Millar, T. J., A. Bennett, and E. Herbst, 1989, Astrophys. J. **340**, 906.
Miller, S., 2012, *The Chemical Cosmos: A Guided Tour* (Springer, New York).
Miller, S., 2018, *The Elusive Triangle: The Discovery of the* H^+_3 *Molecular Ion in the Atmosphere of Jupiter* (Royal Society of London, London), pp. 28–35.
Miller, S., N. Achilleos, G. E. Ballester, T. R. Geballe, R. D. Joseph, R. Prangé, D. Rego, T. Stallard, J. Tennyson, and L. M. Trafton, 2000, Phil. Trans. R. Soc. A **358**, 2485.
Miller, S., N. Achilleos, G. E. Ballester, H. A. Lam, J. Tennyson, T. R. Geballe, and L. M. Trafton, 1997, Icarus **130**, 57.
Miller, S., N. Achilleos, B. M. Dinelli, H. A. Lam, J. Tennyson, M. F. Jagod, T. R. Geballe, L. M. Trafton, R. D. Joseph, and G. E. Ballester, 1995, Geophys. Res. Lett. **22**, 1629.
Miller, S., R. D. Joseph, and J. Tennyson, 1990, Astrophys. J. **360**, L55.
Miller, S., H. A. Lam, and J. Tennyson, 1994, Can. J. Phys. **72**, 760.
Miller, S., T. Stallard, C. Smith, and al., et, 2006, Phil. Trans. R. Soc. A **364**, 3121.
Miller, S., T. Stallard, J. Tennyson, and H. Melin, 2013, J. Phys. Chem. A **117**, 9770.
Miller, S., and J. Tennyson, 1988a, Astrophys. J. **335**, 486.
Miller, S., and J. Tennyson, 1988b, J. Mol. Spectrosc. **128**, 530.
Miller, S., J. Tennyson, S. Lepp, and A. Dalgarno, 1992, Nature (London) **355**, 420.
Miller, S., J. Tennyson, and B. T. Sutcliffe, 1990, J. Mol. Spectrosc. **141**, 104.
Millward, G., S. Miller, T. Stallard, N. Achilleos, and A. D. Aylward, 2005, Icarus **173**, 200.
Millward, G., S. Miller, T. Stallard, A. D. Aylward, and N. Achilleos, 2002, Icarus **160**, 95.
Mitchell, D. G., W. S. Kurth, G. B. Hospodarsky, N. Krupp, J. Saur, B. H. Mauk, J. F. Carbary, S. M. Krimigis, M. K. Dougherty, and D. C. Hamilton, 2009, J. Geophys. Res. Space Phys. **114**, A02212.
Mizus, I. I., A. Alijah, N. F. Zobov, A. A. Kyuberis, S. N. Yurchenko, J. Tennyson, and O. L. Polyansky, 2017, Mon. Not. R. Astron. Soc. **468**, 1717.
Mizus, I. I., O. L. Polyansky, L. K. McKemmish, J. Tennyson, A. Alijah, and N. F. Zobov, 2019, Mol. Phys. **117**, 1663.
Moore, K. M., *et al.*, 2018, Nature (London) **561**, 76.
Moore, L., H. Melin, J. O'Donoghue, T. S. Stallard, J. I. Moses, M. Galand, S. Miller, and C. A. Schmidt, 2019, Phil. Trans. R. Soc. A **377**, 20190067.
Moore, L., J. O'Donoghue, H. Melin, T. Stallard, C. Tao, B. Zieger, J. Clarke, M. F. Vogt, T. Bhakyapaibul, and M. Opher, 2017, Geophys. Res. Lett. **44**, 4513.
Moore, L., J. O'Donoghue, I. Müller-Wodarg, M. Galand, and M. Mendillo, 2015, Icarus **245**, 355.
Moore, L., *et al.*, 2018, Geophys. Res. Lett. **45**, 9398.
Morioka, A., S. Yaegashi, H. Nozawa, H. Misawa, Y. S. Miyoshi, F. Tsuchiya, and S. Okano, 2004, Geophys. Res. Lett. **31**, L16806.
Morong, C. P., J. L. Gottfried, and T. Oka, 2009, J. Mol. Spectrosc. **255**, 13.
Morris, M., and E. Serabyn, 1996, Annu. Rev. Astron. Astrophys. **34**, 645.
Moss, R. E., 1996, Mol. Phys. **89**, 195.
Mou, G., D. Sun, and F. Xie, 2018, Astrophys. J. **869**, L20.
Mountain, C. M., D. J. Robertson, T. J. Lee, and R. Wade, 1990, Proc. SPIE Int. Soc. Opt. Eng. **1235**, 25.
Müller-Wodarg, I. C. F., T. T. Koskinen, L. Moore, J. Serigano, R. V. Yelle, S. Hörst, J. H. Waite, and M. Mendillo, 2019, Geophys. Res. Lett. **46**, 2372.
Munro, J. J., J. Ramanlal, and J. Tennyson, 2005, New J. Phys. **7**, 196.
Muolo, A., E. Matyus, and M. Reiher, 2018, J. Chem. Phys. **149**, 184105.
Muolo, A., E. Mátyus, and M. Reiher, 2019, J. Chem. Phys. **151**, 154110.
Mura, A., A. Adriani, F. Altieri, J. E. P. Connerney, S. J. Bolton, M. L. Moriconi, J. C. Gérard, W. S. Kurth, B. M. Dinelli, and F. Fabiano, 2017, Geophys. Res. Lett. **44**, 5308.
Mura, A., *et al.*, 2018, Science **361**, 774.
Neale, L., S. Miller, and J. Tennyson, 1996, Astrophys. J. **464**, 516.
Neale, L., and J. Tennyson, 1995, Astrophys. J. **454**, L169.
Nichols, J., and S. Cowley, 2004, Ann. Geophys. **22**, 1799.
Nichols, J. D., J. T. Clarke, S. W. H. Cowley, J. Duval, A. J. Farmer, J. C. Gérard, D. Grodent, and S. Wannawichian, 2008, J. Geophys. Res. Space Phys. **113**, A11205.
Novotný, O., *et al.*, 2019, Science **365**, 676.
O'Donoghue, J., H. Melin, T. S. Stallard, G. Provan, L. Moore, S. V. Badman, S. W. H. Cowley, K. H. Baines, S. Miller, and J. S. D. Blake, 2016, Icarus **263**, 44.
O'Donoghue, J., L. Moore, J. Connerney, H. Melin, T. S. Stallard, S. Miller, and K. H. Baines, 2019, Icarus **322**, 251.
O'Donoghue, J., L. Moore, J. E. P. Connerney, H. Melin, T. S. Stallard, S. Miller, and K. H. Baines, 2017, Geophys. Res. Lett. **44**, 11 762.

O'Donoghue, J., L. Moore, T. S. Stallard, and H. Melin, 2016, Nature (London) **536**, 190.
O'Donoghue, J., T. S. Stallard, H. Melin, S. W. H. Cowley, S. V. Badman, L. Moore, S. Miller, C. Tao, K. H. Baines, and J. S. D. Blake, 2014, Icarus **229**, 214.
O'Donoghue, J., T. S. Stallard, H. Melin, G. H. Jones, S. W. H. Cowley, S. Miller, K. H. Baines, and J. S. D. Blake, 2013, Nature (London) **496**, 193.
Oka, T., 1980, Phys. Rev. Lett. **45**, 531.
Oka, T., 1981, Phil. Trans. R. Soc. A **303**, 543.
Oka, T., 1992, Rev. Mod. Phys. **64**, 1141.
Oka, T., 2002, Nature (London) **418**, 31.
Oka, T., 2004, J. Mol. Spectrosc. **228**, 635.
Oka, T., 2006, Proc. Natl. Acad. Sci. U.S.A. **103**, 12235.
Oka, T., 2013, Chem. Rev. **113**, 8738.
Oka, T., 2019, Phil. Trans. R. Soc. A **377**, 20180402.
Oka, T., and E. Epp, 2004, Astrophys. J. **613**, 349.
Oka, T., and T. R. Geballe, 1990, Astrophys. J. **351**, L53.
Oka, T., T. R. Geballe, M. Goto, T. Usuda, Benjamin, J. McCall, and N. Indriolo, 2019, Astrophys. J. **883**, 54.
Oka, T., T. R. Geballe, M. Goto, T. Usuda, and B. J. McCall, 2005, Astrophys. J. **632**, 882.
Orton, G., *et al.*, 1995, Science **267**, 1277.
Padoan, P., and J. Scalo, 2005, Astrophys. J. **624**, L97.
Pan, F. S., and T. Oka, 1986, Astrophys. J. **305**, 518.
Parise, B., A. Castets, E. Herbst, E. Caux, C. Ceccarelli, I. Mukhopadhyay, and A. G. G. M. Tielens, 2004, Astron. Astrophys. **416**, 159.
Pavanello, M., and L. Adamowicz, 2009, J. Chem. Phys. **130**, 034104.
Pavanello, M., *et al.*, 2012, Phys. Rev. Lett. **108**, 023002.
Perry, A. J., J. N. Hodges, C. R. Markus, G. S. Kocheril, and B. J. McCall, 2015, J. Mol. Spectrosc. **317**, 71.
Petrignani, A., M. Berg, A. Wolf, I. I. Mizus, O. L. Polyansky, J. Tennyson, N. F. Zobov, M. Pavanello, and L. Adamowicz, 2014, J. Chem. Phys. **141**, 241104.
Plašil, R., J. Glosík, V. Poterya, P. Kudrna, J. Rusz, M. Tichý, and A. Pysanenko, 2002, Int. J. Mass Spectrom. **218**, 105.
Polyansky, O. L., A. Alijah, N. F. Zobov, I. I. Mizus, R. Ovsyannikov, J. Tennyson, T. Szidarovszky, and A. G. Császár, 2012, Phil. Trans. R. Soc. A **370**, 5014.
Polyansky, O. L., and J. Tennyson, 1999, J. Chem. Phys. **110**, 5056.
Provan, G., D. J. Andrews, C. S. Arridge, A. J. Coates, S. W. H. Cowley, S. E. Milan, M. K. Dougherty, and D. M. Wright, 2009, J. Geophys. Res. Space Phys. **114**, A02225.
Provan, G., L. Lamy, S. W. H. Cowley, and M. K. Dougherty, 2014, J. Geophys. Res. Space Phys. **119**, 7380.
Pryor, W. R., L. W. Esposito, A. Jouchoux, R. A. West, D. Grodent, J. C. Gérard, A. Radioti, L. Lamy, and T. Koskinen, 2019, J. Geophys. Res. Planets **124**, 1979.
Pryor, W. R., *et al.*, 2011, Nature (London) **472**, 331.
Quack, M., 1977, Mol. Phys. **34**, 477.
Rachford, B. L., *et al.*, 2002, Astrophys. J. **577**, 221.
Rachford, B. L., *et al.*, 2009, Astrophys. J. Suppl. Ser. **180**, 125.
Radioti, A., M. Lystrup, B. Bonfond, D. Grodent, and J. C. Gérard, 2013, J. Geophys. Res. Space Phys. **118**, 2286.
Ramanlal, J., O. L. Polyansky, and J. Tennyson, 2003, Astron. Astrophys. **406**, 383.
Ray, L. C., C. T. S. Lorch, J. O'Donoghue, J. N. Yates, S. V. Badman, C. G. A. Smith, and T. S. Stallard, 2019, Phil. Trans. R. Soc. A **377**, 20180407.
Raynaud, E., E. Lellouch, J. P. Maillard, G. R. Gladstone, J. H. Waite, B. Bézard, P. Drossart, and T. Fouchet, 2004, Icarus **171**, 133.
Rayner, J. T., *et al.*, 1993, Proc. SPIE Int. Soc. Opt. Eng. **1946**, 490.
Rego, D., N. Achilleos, T. Stallard, S. Miller, R. Prangé, M. Dougherty, and R. D. Joseph, 1999, Nature (London) **399**, 121.
Rego, D., S. Miller, N. Achilleos, R. Prangé, and R. D. Joseph, 2000, Icarus **147**, 366.
Ribas, I., 2006, Highlights Astron. **2**, 295.
Ribas, I., E. F. Guinan, M. Güdel, and M. Audard, 2005, Astrophys. J. **622**, 680.
Ribas, I., G. F. Porto de Mello, L. D. Ferreira, E. Hébrard, F. Selsis, S. Catalán, A. Garcés, J. do Nascimento, J. D., and J. R. de Medeiros, 2010, Astrophys. J. **714**, 384.
Roberts, H., E. Herbst, and T. J. Millar, 2003, Astrophys. J. **591**, L41.
Röhse, R., W. Kutzelnigg, R. Jaquet, and W. Klopper, 1994, J. Chem. Phys. **101**, 2231.
Roueff, E., E. Dartois, T. R. Geballe, and M. Gerin, 2006, Astron. Astrophys. **447**, 963.
Sanchez-Lavega, A., 2011, *An Introduction to Planetary Atmospheres* (Taylor & Francis, London).
Sandel, B. R., A. L. Broadfoot, and D. F. Strobel, 1980, Geophys. Res. Lett. **7**, 5.
Sandel, B. R., F. Herbert, A. J. Dessler, and T. W. Hill, 1990, Geophys. Res. Lett. **17**, 1693.
Sandel, B. R., *et al.*, 1979, Science **206**, 962.
Sarpal, B. K., J. Tennyson, and L. A. Morgan, 1994, J. Phys. B **27**, 5943.
Satoh, T., and J. E. P. Connerney, 1999a, Icarus **141**, 236.
Satoh, T., and J. E. P. Connerney, 1999b, Geophys. Res. Lett. **26**, 1789.
Saumon, D., and S. B. Jacobson, 1999, Astrophys. J. **511**, L107.
Savić, I., S. Schlemmer, and D. Gerlich, 2020, ChemPhysChem **21**, 1429.
Schneider, I. F., A. E. Orel, and A. Suzor-Weiner, 2000, Phys. Rev. Lett. **85**, 3785.
Scoville, N. Z., 1972, Astrophys. J. **175**, L127.
Seiff, A., D. B. Kirk, T. C. D. Knight, L. A. Young, F. S. Milos, E. Venkatapathy, J. D. Mihalov, R. C. Blanchard, R. E. Young, and G. Schubert, 1997, Science **276**, 102.
Seiff, A., D. B. Kirk, T. C. D. Knight, R. E. Young, J. D. Mihalov, L. A. Young, F. S. Milos, G. Schubert, R. C. Blanchard, and D. Atkinson, 1998, J. Geophys. Res. **103**, 22857.
Shaikhislamov, I. F., M. L. Khodachenko, Y. L. Sasunov, H. Lammer, K. G. Kislyakova, and N. V. Erkaev, 2014, Astrophys. J. **795**, 132.
Shkolnik, E., E. Gaidos, and N. Moskovitz, 2006, Astron. J. **132**, 1267.
Sidhu, K. S., S. Miller, and J. Tennyson, 1992, Astron. Astrophys. **255**, 453.
Skilling, J., and A. W. Strong, 1976, Astron. Astrophys. **53**, 253.
Skinner, T. E., S. T. Durrance, P. D. Feldman, and H. W. Moos, 1984, Astrophys. J. **278**, 441.
Smith, C. G. A., 2006, Ann. Geophys. **24**, 2709.
Smith, C. G. A., 2011, Mon. Not. R. Astron. Soc. **410**, 2315.
Smith, C. G. A., and N. Achilleos, 2012, Mon. Not. R. Astron. Soc. **422**, 1460.
Smith, C. G. A., and A. D. Aylward, 2008, Ann. Geophys. **26**, 1007.
Smith, C. G. A., and A. D. Aylward, 2009, Ann. Geophys. **27**, 199.
Smith, C. G. A., A. D. Aylward, S. Miller, and I. C. F. Müller-Wodarg, 2005, Ann. Geophys. **23**, 2465.
Smith, C. G. A., A. D. Aylward, G. H. Millward, S. Miller, and L. E. Moore, 2007, Nature (London) **445**, 399.
Smith, D., and N. G. Adams, 1987, J. Chem. Soc., Faraday Trans. 2 **83**, 149.
Smith, E. J., L. Davis, Jr., and D. E. Jones, 1976, *Jupiter's Magnetic Field and Magnetosphere*, Space Science Series Vol. 81 (University of Arizona Press, Tucson), pp. 788–829.

Smith, G. R., D. E. Shemansky, J. B. Holberg, A. L. Broadfoot, B. R. Sandel, and J. C. McConnell, 1983, J. Geophys. Res. **88**, 8667.

Snow, T. P., and B. J. McCall, 2006, Annu. Rev. Astron. Astrophys. **44**, 367.

Sochi, T., and J. Tennyson, 2010, Mon. Not. R. Astron. Soc. **405**, 2345.

Sofia, U. J., J. T. Lauroesch, D. M. Meyer, and S. I. B. Cartledge, 2004, Astrophys. J. **605**, 272.

Sommeria, J., L. B. Jaffel, and R. Prangé, 1995, Icarus **118**, 2.

Spencer, J. R., and J. Mitton, 1995, Eds., *The Great Comet Crash* (Cambridge University Press, Cambridge, England).

Spyromilio, J., B. Leibundgut, C. Fransson, J. Larsson, K. Migotto, and J. Girard, 2017, The Messenger **167**, 26.

Stallard, T., H. Melin, S. W. H. Cowley, S. Miller, and M. B. Lystrup, 2010, Astrophys. J. **722**, L85.

Stallard, T., S. Miller, G. E. Ballester, D. Rego, R. D. Joseph, and L. M. Trafton, 1999, Astrophys. J. **521**, L149.

Stallard, T., S. Miller, M. Lystrup, N. Achilleos, E. J. Bunce, C. S. Arridge, M. K. Dougherty, S. W. H. Cowley, S. V. Badman, and D. L. Talboys, 2008, Nature (London) **456**, 214.

Stallard, T., S. Miller, H. Melin, M. Lystrup, S. W. H. Cowley, E. J. Bunce, N. Achilleos, and M. Dougherty, 2008, Nature (London) **453**, 1083.

Stallard, T., S. Miller, H. Melin, M. Lystrup, M. Dougherty, and N. Achilleos, 2007, Icarus **189**, 1.

Stallard, T., S. Miller, G. Millward, and R. D. Joseph, 2001, Icarus **154**, 475.

Stallard, T., S. Miller, G. Millward, and R. D. Joseph, 2002, Icarus **156**, 498.

Stallard, T., C. Smith, S. Miller, H. Melin, M. Lystrup, A. Aylward, N. Achilleos, and M. Dougherty, 2007b, Icarus **191**, 678.

Stallard, T. S., A. G. Burrell, H. Melin, L. N. Fletcher, S. Miller, L. Moore, J. O'Donoghue, J. E. P. Connerney, T. Satoh, and R. E. Johnson, 2018, Nat. Astron. **2**, 773.

Stallard, T. S., J. T. Clarke, H. Melin, S. Miller, J. D. Nichols, J. O'Donoghue, R. E. Johnson, J. E. P. Connerney, T. Satoh, and M. Perry, 2016, Icarus **268**, 145.

Stallard, T. S., A. Masters, S. Miller, H. Melin, E. J. Bunce, C. S. Arridge, N. Achilleos, M. K. Dougherty, and S. W. H. Cowley, 2012, J. Geophys. Res. Space Phys. **117**, A12302.

Stallard, T. S., H. Melin, S. Miller, S. V. Badman, K. H. Baines, R. H. Brown, J. S. D. Blake, J. O'Donoghue, R. E. Johnson, and B. Bools, 2015, J. Geophys. Res. Space Phys. **120**, 6948.

Stallard, T. S., H. Melin, S. Miller, S. V. Badman, R. H. Brown, and K. H. Baines, 2012, Geophys. Res. Lett. **39**, L15103.

Stallard, T. S., H. Melin, S. Miller, L. Moore, J. O'Donoghue, J. E. P. Connerney, T. Satoh, R. A. West, J. P. Thayer, and V. W. Hsu, 2017, Geophys. Res. Lett. **44**, 3000.

Stallard, T. S., H. Melin, S. Miller, J. O'Donoghue, S. W. H. Cowley, S. V. Badman, A. Adriani, R. H. Brown, and K. H. Baines, 2012, Phil. Trans. R. Soc. A **370**, 5213.

Stallard, T. S., S. Miller, S. W. H. Cowley, and E. J. Bunce, 2003, Geophys. Res. Lett. **30**, 1221.

Stallard, T. S., S. Miller, L. M. Trafton, T. R. Geballe, and R. D. Joseph, 2004, Icarus **167**, 204.

Stallard, T. S., *et al.*, 2019, Phil. Trans. R. Soc. A **377**, 20180405.

Stark, R., F. F. S. van der Tak, and E. F. van Dishoeck, 1999, Astrophys. J. **521**, L67.

Strobel, D. F., and G. R. Smith, 1973, J. Atmos. Sci. **30**, 718.

Su, M., T. R. Slatyer, and D. P. Finkbeiner, 2010, Astrophys. J. **724**, 1044.

Suleimanov, Y. V., A. Aguado, S. Gomez-Carrasco, and O. Roncero, 2018, J. Phys. Chem. Lett. **9**, 2133.

Sundstrom, G., *et al.*, 1994, Science **263**, 785.

Szidarovszky, T., and A. G. Csaszar, 2013, Mol. Phys. **111**, 2131.

Tao, C., S. V. Badman, and M. Fujimoto, 2011, Icarus **213**, 581.

Tao, C., S. V. Badman, T. Uno, and M. Fujimoto, 2012, Icarus **221**, 236.

Tao, C., Y. Miyoshi, N. Achilleos, and H. Kita, 2014, J. Geophys. Res. Space Phys. **119**, 3664.

Tennyson, J., 1996, Comments At. Mol. Phys. **32**, 209.

Tennyson, J., 2019, *Astronomical Spectroscopy: An Introduction to the Atomic and Molecular Physics of Astronomical Spectroscopy*, 3rd ed. (World Scientific, Singapore).

Tennyson, J., K. Hulme, O. K. Naim, and S. N. Yurchenko, 2016, J. Phys. B **49**, 044002.

Tennyson, J., O. L. Polyansky, N. F. Zobov, A. Alijah, and A. G. Császár, 2017, J. Phys. B **50**, 232001.

Thomson, J. J., 1913, Proc. R. Soc. A **89**, 1.

Thorne, R. M., 1982, J. Geophys. Res. **87**, 8105.

Tinetti, G., *et al.*, 2018, Exp. Astron. **46**, 135.

Toomey, D. W., M. Shure, E. M. Irwin, and M. E. Ressler, 1990, Proc. SPIE Int. Soc. Opt. Eng. **1235**, 69.

Trafton, L., J. Carr, D. Lester, and P. Harvey, 1988, Icarus **74**, 351.

Trafton, L., D. Lester, J. Carr, and P. M. Harvey, 1986, in, Bull. Am. Astron. Soc. **18**, 773.

Trafton, L., D. F. Lester, and K. L. Thompson, 1989, Astrophys. J. **343**, L73.

Trafton, L. M., T. R. Geballe, S. Miller, J. Tennyson, and G. E. Ballester, 1993, Astrophys. J. **405**, 761.

Trafton, L. M., S. Miller, T. R. Geballe, J. Tennyson, and G. E. Ballester, 1999, Astrophys. J. **524**, 1059.

Uno, T., Y. Kasaba, C. Tao, T. Sakanoi, M. Kagitani, S. Fujisawa, H. Kita, and S. V. Badman, 2014, J. Geophys. Res. Space Phys. **119**, 10 219.

Urbain, X., A. Dochain, R. Marion, T. Launoy, and J. Loreau, 2019, Phil. Trans. R. Soc. A **377**, 20180399.

Uy, D., M. Cordonnier, and T. Oka, 1997, Phys. Rev. Lett. **78**, 3844.

van der Tak, F. F. S., P. Schilke, H. S. P. Müller, D. C. Lis, T. G. Phillips, M. Gerin, and E. Roueff, 2002, Astron. Astrophys. **388**, L53.

van Dishoeck, E. F., and J. H. Black, 1986, Astrophys. J. Suppl. Ser. **62**, 109.

Vastel, C., T. G. Phillips, and H. Yoshida, 2004, Astrophys. J. **606**, L127.

Velilla, L., B. Lepetit, A. Aguado, J. A. Beswick, and M. Paniagua, 2008, J. Chem. Phys. **129**, 084307.

Vidal-Madjar, A., A. Lecavelier des Etangs, J. M. Désert, G. E. Ballester, R. Ferlet, G. Hébrard, and M. Mayor, 2003, Nature (London) **422**, 143.

Vriesema, J., T. Koskinen, R. Yelle, and I. Müller-Wodarg, 2019, in *Proceedings of the EPSC-DPS Joint Meeting 2019* (Europlanet/Copernicus, Goettingen, Germany), pp. EPSC–DPS2019–1019.

Vriesema, J. W., T. T. Koskinen, and R. V. Yelle, 2020, Icarus **344**, 113390.

Waite, J. H., T. E. Cravens, J. Kozyra, A. F. Nagy, S. K. Atreya, and R. H. Chen, 1983, J. Geophys. Res. **88**, 6143.

Waite, J. H., G. R. Gladstone, W. S. Lewis, P. Drossart, T. E. Cravens, A. N. Maurellis, B. H. Mauk, and S. Miller, 1997, Science **276**, 104.

Waite, J. H., *et al.*, 2001, Nature (London) **410**, 787.

Waite, J. H., *et al.*, 2018, Science **362**, eaat2382.

Walmsley, C. M., D. R. Flower, and G. Pineau des Forêts, 2004, Astron. Astrophys. **418**, 1035.

Watanabe, H., H. Kita, C. Tao, M. Kagitani, T. Sakanoi, and Y. Kasaba, 2018, Geophys. Res. Lett. **45**, 11 547.

Watson, J. K., 1984, J. Mol. Spectrosc. **103**, 125 .
Watson, W. D., 1973a, Astrophys. J. **182**, L73.
Watson, W. D., 1973b, Astrophys. J. **183**, L17.
Weinberg, D. H., 2017, Astrophys. J. **851**, 25.
Winkel, B., H. Wiesemeyer, K. M. Menten, M. Sato, A. Brunthaler, F. Wyrowski, D. Neufeld, M. Gerin, and N. Indriolo, 2017, Astron. Astrophys. **600**, A2.
Woodgate, B. E., *et al.*, 1998, Publ. Astron. Soc. Pac. **110**, 1183.
Wu, W., *et al.*, 2019, Rev. Sci. Instrum. **90**, 101501.
Xu, L.-W., M. Rösslein, C. M. Gabrys, and T. Oka, 1992, J. Mol. Spectrosc. **153**, 726.
Yan, M., and A. Dalgarno, 1998, Astrophys. J. **500**, 1049.
Yang, H. Y., M. Ruszkowski, and E. Zweibel, 2018, Galaxies **6**, 29.
Yates, J. N., N. Achilleos, and P. Guio, 2014, Planet. Space Sci. **91**, 27.
Yates, J. N., L. C. Ray, and N. Achilleos, 2018, J. Geophys. Res. Space Phys. **123**, 9357.
Yates, J. N., L. C. Ray, N. Achilleos, O. Witasse, and N. Altobelli, 2020, J. Geophys. Res. Space Phys. **125**, e2019JA026792.
Yelle, R. V., 2004, Icarus **170**, 167.
Yelle, R. V., and S. Miller, 2004, in *Jupiter: The Planet, Satellites and Magnetosphere*, Vol. 1, edited by F. Bagenal, T. E. Dowling, and W. B. McKinnon (Cambridge University Press, Cambridge, England), pp. 185–218.
Yousif, F. B., C. Cisneros, J. de Urquijo, and I. Alvarez, 2001, J. Phys. B **34**, 725.
Yousif, F. B., and J. B. A. Mitchell, 1989, Phys. Rev. A **40**, 4318.
Yusef-Zadeh, F., M. Muno, M. Wardle, and D. C. Lis, 2007, Astrophys. J. **656**, 847.
Yusef-Zadeh, F., *et al.*, 2013, Astrophys. J. **762**, 33.
Zobov, N. F., S. V. Shirin, L. Lodi, B. C. Silva, J. Tennyson, A. G. Császár, and O. L. Polyansky, 2011, Chem. Phys. Lett. **507**, 48.